Diss. ETH No. 25152

Electrostatically induced nanostructures in bilayer graphene

A thesis submitted to attain the degree of

DOCTOR OF SCIENCES of ETH ZURICH
(Dr. sc. ETH Zurich)

presented by

Hiske Catharina Overweg

MSc Physics, Universiteit Leiden

born on 18.11.1989
citizen of the Netherlands

accepted on the recommendation of:

Prof. Dr. Klaus Ensslin, examiner
Prof. Dr. Thomas Ihn, co-examiner
Dr. Srijit Goswami, co-examiner
Prof. Dr. Christian Degen, co-examiner

2018

Abstract

Soon after the discovery of graphene [1], the idea was put forward that this material could be an attractive host for spin qubits [2]. Because of the low atomic weight of carbon, spin-orbit interactions in graphene are small. On top of that, the material mostly consists of nuclear spin-free C_{12}, which leads to a small hyperfine interaction. Both of these facts should lead to a long coherence time of electron spins, which is an important criterion for a quantum computation platform [3].

A first step towards the creation of a spin qubit in graphene is the implementation of confinement of charge carriers on the nanoscale. Single layer graphene has a gapless band structure, which makes it hard to realize controlled confinement [4]. The tunable band structure of bilayer graphene provides a solution. By applying a vertical electric field to this material a band gap is opened [5]. When the Fermi level is locally tuned into the band gap, confinement can be realized.

In this thesis we investigate the confinement of charge carriers in bilayer graphene by electrostatic gating. We start with a literature overview of the bilayer graphene band gap, which shows that in most bilayer graphene devices the low-temperature resistivity in presence of an electric field saturates at values lower than those predicted by theory. This has hampered the electrostatic definition of nanostructures in bilayer graphene so far.

We then report on the fabrication of samples consisting of exfoliated bilayer graphene encapsulated in hexagonal boron nitride and compare the transport properties to those of a device made with bilayer graphene grown by chemical vapor deposition. The former show signatures of ballistic transport in terms of Fabry-Pérot oscillations, as previously reported in Ref. [6] and exhibit a Lifshitz transition in the quantum Hall regime, as observed before in Ref. [7].

We continue to study dual-gated encapsulated bilayer graphene devices. Chapter 5 and Ref. [8] report on magnetoresistance oscillations in the p-n regime in intermediate magnetic fields.

Despite the observation of various interesting physical phenomena in dual-gated devices, the maximal resistance in these devices usually stayed in the range of tens of kiloohms, which is insufficient for electrostatic definition of nanostructures [9]. In Chapter 6 and Ref. [10] we demonstrate that the incorporation of a graphite back gate into the device structure reproducibly leads to induced resistances in the megaohm or even gigaohm regime, paving the path for electrostatically defined nanostructures.

In Chapter 7 and Ref. [10] we report on quantized conductance measured in a device with a split gate geometry and an additional gate to tune the density in the constriction. We investigate the magnetic field dependence of the conductance through the constriction, which shows a fascinating pattern of level crossings.

By creating a *p*-*n* junction in the same device in the quantum Hall regime, as discussed in Chapter 8 and Ref. [11], we can form a quantum dot, thus realizing electrostatic confinement of charge carriers in bilayer graphene. Finally we suggest future directions for the exploration of gated bilayer graphene nanostructures.

Zusammenfassung

Kurz nach der Entdeckung von Graphen [1] wurde dieses Material als attraktiver Kandidat für Spin Qubits vorgeschlagen [2]. Das geringe atomare Gewicht von Kohlenstoff führt zu einer kleinen Spin-Bahn Wechselwirkung. Des Weiteren besteht das Material hauptsächlich aus C_{12}, welches keinen Kernspin besitzt, sodass auch die hyperfein Wechselwirkung gering ist. Diese beiden Faktoren führen zu langen Kohärenzzeiten des Elektronenspins, was ein wichtiges Kriterium für die Entwicklung von Quanten Computern ist [3].

Ein erster Schritt für die Herstellung von Spin Qubits in Graphen ist die räumliche Einschränkung der Ladungsträger auf der Nanoskala. Die Bandstruktur einzelner Atomlagen von Graphen zeigt keine Bandlücke, weshalb die Realisierung von elektrisch kontrollierbaren Quantenstrukturen in diesem Material schwierig ist [4]. In zwei Atomlagen Kohlenstoff (bilayer graphene) ist die Bandstruktur einstellbar, sodass durch das Anlegen eines elektrischen Feldes eine Bandlücke [5] und somit eine lokale Einschränkung der Ladungsträger, durch das Einstellen des Fermi Niveaus in die Bandlücke, erzeugt werden kann.

In dieser Arbeit wird die Herstellung von Nanostrukturen in zweilagigem Graphen durch lokale elektrostatische Kontrolle untersucht. Eine Literaturübersicht der Bandlücke in zweilagigem Graphen zeigt, dass der Widerstand in den meisten Strukturen bei tiefen Temperaturen im elektrischen Feld nicht den theoretisch vorhergesagten Wert erreicht. Dies hat die Herstellung von Nanostrukturen in zwei Atomlagen Kohlenstoff bisher erschwert.

Des Weiteren berichten wir über die Herstellung von Proben mit exfoliiertem zweilagigem Graphen eingebettet in hexagonalem Bornitrid und vergleichen die Transporteigenschaften mit Strukturen in denen das zweilagiges Graphen mit chemischer Gasphasenabscheidung (chemical vapour deposition) hergestellt wurde. Erstere zeigen Anzeichen von ballistischem Transport in Form von Fabry-Pérot Oszillationen, wie zuvor in Ref. [12] berichtet und weisen Liftshitz Übergänge im Quanten-Hall-Regime auf, ähnlich wie in Ref. [13].

Außerdem untersuchen wir Strukturen aus zweilagigem Graphen, die in Bornitrid eingebettet sind und mit zwei Gate-Kontakten (dual-gated) kontrolliert werden. Kapitel 5 und Ref. [8] berichten über Oszillationen des Magnetowiderstands im p-n Bereich in mittleren Magnetfeldern.

Neben der Beobachtung von verschiedenen physikalischen Phänomenen in Proben die lokal mit zwei Gate-Kontakten gesteuert werden, konnte der Widerstand in

diesen Strukturen nicht auf mehr als 10 Kiloohm erhöht werden, was nicht für die elektrische Definition von Nanostrukturen ausreicht [9]. In Kapitel 6 und Ref. [10] zeigen wird, dass die Ergänzung der Strukturen mit einem Graphit Rückkontakt reproduzierbar zu einer Erhöhung des Widerstandes in den Megaohm oder Gigaohm Bereich führen, wodurch der Weg für die Herstellung elektrostatisch definierter Nanostrukturen bereitet wurde.

In Kapitel 7 und Ref. [10] wird die quantisierte Leitfähigkeit in Proben gemessen, in denen ein Kanal mit Gates definiert wird und die Ladungsträgerdichte in diesem Kanal über ein weiteres Gate gesteuert werden kann. Wir untersuchen die Magnetfeldabhängigkeit der Leitfähigkeit durch diese Struktur, welche ein faszinierendes Muster von Niveaukreuzungen zeigt.

Durch die Erzeugung eines p-n- Übergangs in derselben Struktur im Quantenhallregime, wird ein Quantenpunkt geformt, wodurch die elektrostatische Einschränkung von Ladungsträgeren in zwei lagigem Graphen gezeigt wird, siehe Kapitel 8 und Ref. [11]. Zum Schluss geben wir eine Aussicht für zukünftige Untersuchungen an elektrostatisch definierten Nanostrukturen in zweilagigem Graphen.

Contents

Lists of symbols

physical constants	explanation
$e < 0$	electron charge
ϵ_o	vacuum dielectric constant
$h = 2\pi\hbar$	Planck's constant
k_B	Boltzmann constant
$\phi_0 = h/e$	magnetic flux quantum
$R_K = h/e^2$	von Klitzing constant

graphene constants	explanation
a_0	graphene lattice constant
c_0	distance between graphene layers
γ_0	intralayer coupling
γ_1	interlayer coupling
γ_3	skew interlayer coupling
v	effective speed of light

Abbreviation	Explanation
2D	two-dimensional
2DEG	two-dimensional electron gas
AC	alternating current
AFM	atomic force microscopy
BG	back gate
BLG	bilayer graphene
CVD	chemical vapor deposition
CH	channel gate
D	drain
DC	direct current
DG	dual-gated
DOS	density of states
FQHE	fractional quantum Hall effect
GC	green contrast
hBN	hexagonal boron nitride
MAA	methacrylic acid
MISO	magneto-intersubband oscillations
MMA	methyl methacrylate
PC	Polycarbonate
PDMS	polydimethylsiloxane
PG	plunger gate
PMMA	polymethyl methacrylate
QHE	quantum Hall effect
QPC	quantum point contact
RGB	red, green, blue
S	source
SG	split gate or-single gated
SdH	Shubnikov - de Haas
TG	top gate
UV	ultraviolet

Symbol	Explanation
A	area
α	top gate capacitance
α_{CH}	lever arm of the channel gate
B	magnetic field
β	back gate capacitance
C	capacitance per area
d	distance
E	energy
E_{gap}	energy gap
$\mathcal{E}$	electric field
ϵ	dielectric permittivity
ϵ_i	on-site energy
E_F	Fermi energy
G	conductance
g	degeneracy
g^*	electron g-factor
h	height
I	current
I_g	green component of RGB color space
k_F	Fermi wave vector
$\mathbf{k}, k_\mathrm{x}, k_\mathrm{y}$	wave vector
ℓ	charge carrier mean free path
L, W	system size (length, width)
L_c	cavity length
m^*	effective charge carrier mass
μ	charge carrier mobility
n	charge carrier density
ν	filling factor
ω	angular frequency
ω_0	frequency of the electrostatic potential
ω_c	cyclotron frequency
R	resistance
R_c	cyclotron radius
R_S	series resistance
ρ	resistivity
s_f	scaling factor of the tight-binding model
σ	conductivity
t	thickness
T	temperature or transmission
U	interlayer asymmetry
V	voltage

Chapter 1

Introduction

In this chapter we introduce graphene (Section 1.1), discuss its potential for quantum computation (Section 1.2) and describe the nanostructures we study, namely quantum point contacts (Section 1.3) and quantum dots (Section 1.4). We focus on the basic physical phenomena occuring in these nanostructures. A more detailed discussion can be found in Ref. [14].

1.1 Graphene

Research on graphene has skyrocketed since its experimental discovery in 2004. To quantify this statement, we can take a look at the red data points Fig. 1.1, which represent the number of search results on Google Scholar which include the word graphene per year[1,2]. This number has surpassed 100.000 in recent years. The graphene hype has lead to various interesting product labels such as graphene skis (see Fig. 1.2), graphene hair dye [15] and even graphene blockchain [16].

Why is this material attracting so much attention? Graphene has many properties which make it stand out. As a single sheet of carbon atoms, it is the thinnest material conceivable, it is extremely strong [17] and exhibits exceptional electronic [18] and thermal conductivity [19]. The Dirac-like Hamiltonian of single layer graphene leads to the occurrence of various exotic physical phenomena, such as Klein tunneling [20] and a half-integer Hall quantization [21]. Its bilayer equivalent has a tunable band structure [5], which can make the material semiconducting. On top of that, it has recently been shown that by introducing a twist angle between the layers, it can become a Wigner crystal and a superconductor [22, 23]. Finally, there are indications that twisted bilayer graphene exhibits topological states [24, 25] -

---

[1] This number is not necessarily equal to the number of scientific publications per year. Although citations and patents have been excluded from the query, some cross references to publications from other years are still counted and some publications are simply dated incorrectly. This number should therefore be interpreted as a rough estimate of the number of publications.

[2] We thank Volker Strobel for the 'academic-keyword-occurrence' tool (`https://github.com/Pold87/academic-keyword-occurrence`).

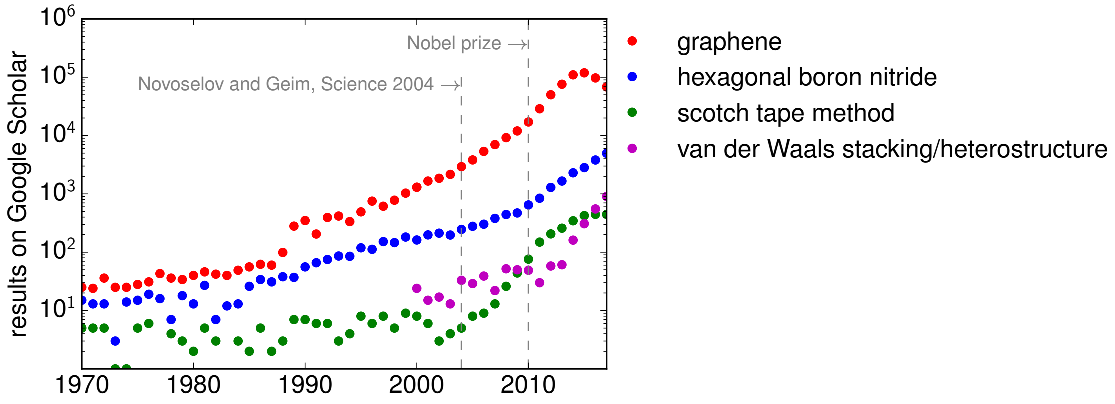

Figure 1.1: Number of search results on Google Scholar as a function of year for the search terms graphene, scotch tape method, hexagonal boron nitride and van der Waals stacking/heterostructure

the rich phenomenology of graphene keeps surprising us.

One other attractive aspect of graphene is the ease with which the material is obtained. Repeated peeling of a small piece of graphite using scotch tape results in micron-sized flakes, some of which consist of only one or two layers. These can be deposited onto a Si substrate by sticking the tape onto the Si substrate and removing it again. This explains the popularity of the term 'scotch tape method' in scientific literature in recent years (see Fig. 1.1, green data points).

Figure 1.2: Graphene ski

The aforementioned Si substrates have significant surface roughness and contain many charged impurities, which limit electronic performance of graphene devices. In 2010 Dean et al. [26] showed the situation can be improved by the use of hexagonal boron nitride (hBN) as a substrate for graphene. As an atomically flat insulating material with almost the same lattice constant as graphene, it is a great substrate for graphene samples. This explains the rising interest of the community in hexagonal boron nitride, as witnessed by the blue data points in Fig. 1.1.

The mobility measured in graphene devices was increased even more when it was realized that graphene could be encapsulated between two layers of hBN [27]. This results in a so-called 'van der Waals stack', because the assembly method relies on the large van der Waals forces between graphene and hBN. The occurrence of this term is plotted in Fig. 1.1 as well (purple data points). The devices studied in this project all consist of graphene encapsulated in hBN.

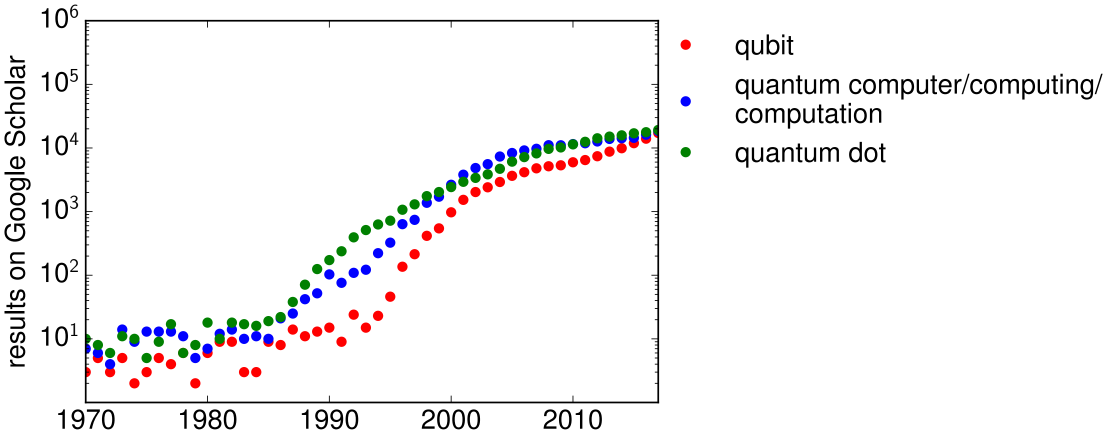

Figure 1.3: Number of search results on Google Scholar as a function of year for the search terms qubit, quantum dot, quantum computation/computer/computing

1.2 Quantum computation

Another flourishing research field is the field of quantum computation (see Fig. 1.3). Quantum computers use qubits instead of ordinary bits to store information. Since qubits can be in a superposition state and can be entangled, quantum computers can perform certain relevant information processing tasks significantly faster than conventional computers [28, 29].

In 2007 Trauzettel et al. [2] proposed the use of an electron spin in graphene as a qubit. They point out that long spin-coherence times, as desired for qubits [3], are expected in graphene. This is due to the low atomic weight of carbon, which leads to small spin-orbit interaction, and the fact that graphene consists mainly of the nuclear spin-free C_{12} isotope, which leads to small hyperfine interaction.

In order to manipulate a single electron spin, it has to be confined to a small region of space. This can be done in a quantum dot, which explains the parallel evolution of the research interest in quantum computation, qubits and quantum dots as seen in Fig. 1.3.

The aim of this project is the confinement of charge carriers in bilayer graphene. Once this landmark is reached, spin states of graphene qubits can be investigated. To study confinement we fabricate quantum point contacts and quantum dots. These systems are introduced in the following sections.

1.3 Quantum point contacts

A quantum point contact is a constriction formed in a two-dimensional electron or hole system (see inset of Fig. 1.4). When the width of the constriction is comparable to the Fermi wavelength, discrete modes arise in the energy spectrum. The modes have a parabolic dispersion relation, because charge carriers are free to move in the

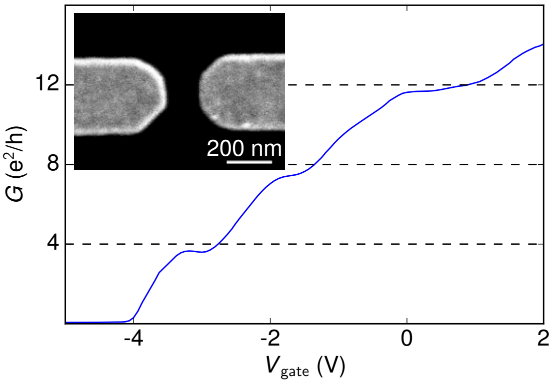

Figure 1.4: Conductance of a quantum point contact as a function of gate voltage, showing conductance plateaus corresponding to quantized modes. Inset: Scanning electron micrograph of a QPC. Bright areas correspond to metallic top gates, dark color corresponds to the hBN surface with graphene underneath.

direction along the channel. It can be shown that each of them contributes e^2/h to the conductance through the constriction [14]. When shifting the Fermi level through the energy spectrum by means of a changing gate voltage, a sequence of plateaus with conductance

$$G = Nge^2/h \tag{1.1}$$

is observed, as shown in Fig. 1.4, where N is the number of occupied modes and g is the degeneracy of these modes.

1.4 Quantum dots

In quantum dots, charge carriers are confined in all spatial directions, which leads to discrete energy levels. Transport through a quantum dot depends on the alignment of the Fermi level in the source and drain reservoirs with respect to the levels in the dot. This is illustrated in Fig. 1.5a,b: whenever an energy level of the quantum dot is within the bias window (Fig. 1.5a), induced by a voltage applied between source and drain contacts, current can flow through the dot. If there is no level within the bias window (Fig. 1.5b), current flow is prohibited, a phenomenon known as Coulomb blockade. With a plunger gate (PG) the dot levels can be shifted up and down in energy, leading to spikes in the current whenever an energy level of the dot is within the bias window. A measurement of the conductance of a quantum dot as a function of plunger gate voltage is shown in Fig. 1.5c. The resonances correspond to indiviual charge carriers hopping onto the dot. A scanning electron micrograph of a dot, with a schematic drawing of electron flow, is shown in the inset of Fig. 1.5c. By optimizing the geometry and adjusting the gate voltages, a quantum dot populated with a single electron can be realized. Such a system can be extended to a double-dot configuration to study spin qubits [30, 31] and measure the coherence time of electron spins.

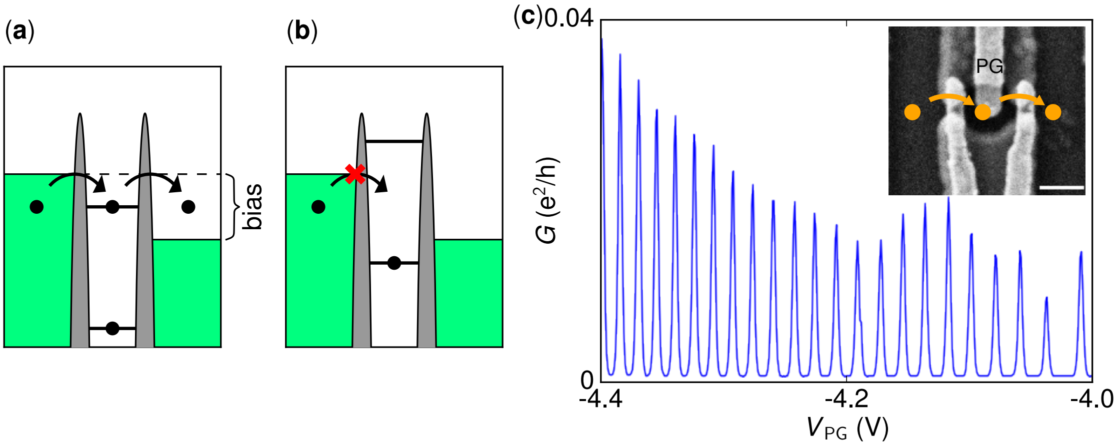

Figure 1.5: (a) Schematic of current flow through a quantum dot. Whenever an energy level of the dot is within the bias window, current can flow. (b) When no level is present within the bias window, current flow through the system is prohibited. (c) Conductance as a function of plunger gate voltage, showing Coulomb blockade.

Chapter 2

Literature overview: The bilayer graphene band gap

The aim of this thesis is to confine charge carriers in bilayer graphene by electrostatic gating. This requires a band structure with a band gap, for which the Fermi level can be tuned into the band gap. The band structure of bilayer graphene and the possibility to induce a band gap is studied from a theoretical perspective in section 2.1. Section 2.2 introduces the electrostatic model of a dual-gated bilayer graphene device. After these theoretical sections, an overview of optical and transport measurements of the bilayer graphene band gap is provided in sections 2.3 and 2.4. Transport measurements often show a resistance which is lower than the theoretically expected resistance. Section 2.5 provides an overview of possible causes of low resistance despite the presence of a band gap. Finally, the implications for the formation of nanostructures are discussed in section 2.6.

2.1 Tight binding model of graphene

In monolayer graphene, three out of the four valence electrons hybridize in sp^2 configuration and form covalent bonds with the neighboring lattice sites, leading to the hexagonal lattice structure. These electrons do not contribute to transport. The remaining electron, relevant for transport, forms a p orbital perpendicular to the plane, which is only slightly perturbed by neighboring atoms. The wave function of this electron can therefore be approximated as a Linear Combination of Atomic Orbitals. Writing the Hamiltonian in this basis results in a tight-binding Hamiltonian for graphene, which describes a system with on-site energy ϵ and hopping parameter γ_0 between neighboring lattice sites:

$$\mathcal{H} = \sum_i \epsilon_i \left|\psi_i\right\rangle \left\langle\psi_i\right| - \sum_{\langle i,j\rangle} \gamma_0 (\left|\psi_i\right\rangle \left\langle\psi_j\right| + \left|\psi_j\right\rangle \left\langle\psi_i\right|) \tag{2.1}$$

where $\left|\psi_i\right\rangle$ is the atomic orbital on the ith site [32, 33].

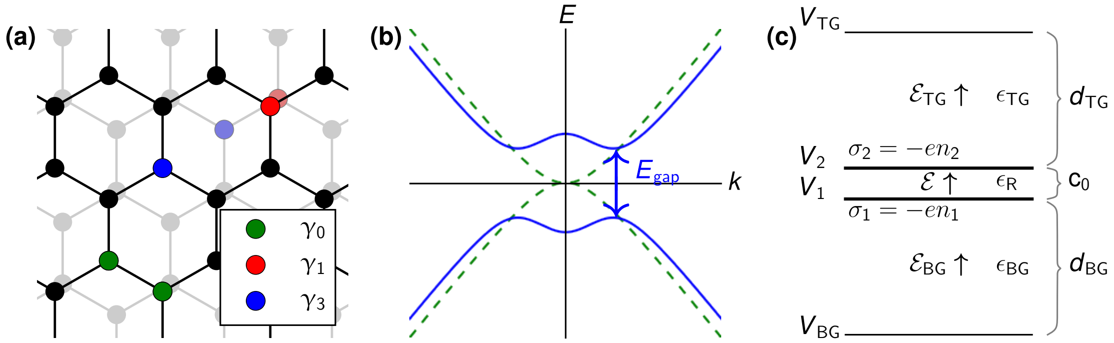

Figure 2.1: (a) Lattice of Bernal-stacked bilayer graphene with the coupling parameters γ (b) Bandstructure of bilayer graphene. In absence of interlayer asymmetry the band structure is gapless (dashed green line). Interlayer asymmetry leads to a band structure with band gap (solid blue line). (c) Schematic of a dual gate bilayer graphene flake.

In bilayer graphene several different hopping parameters have to be taken into account. Bernal-stacked bilayer graphene consists of two layers of hexagonally ordered atoms, where half of the atoms sit directly on top of each other, as shown in Fig. 2.1a. Following the convention of the Slonczewski-Weiss-McClure model for graphite [34, 35], neighboring lattice sites on the same layer (e.g. sites marked in green) have a coupling γ_0 in the tight binding model. Sites directly on top of each other (marked in red) are coupled by γ_1 and the remaining sites which are not vertically aligned (marked in blue) have a coupling γ_3. Infrared spectroscopy measurements [36] have yielded $\gamma_0 = 3.16$ eV, $\gamma_1 = 0.381$ eV and $\gamma_3 = 0.38$ eV. γ_3 only plays a role at low density [5, 37] and will be neglected below. For the lowest energy bands of pristine bilayer graphene the model leads to a gapless bandstructure, as indicated by the green dashed line in Fig. 2.1b. An interlayer asymmetry U between on-site energies on the different layers, which can in practise be realized by an electric field, leads to the opening of a band gap [5, 38, 39]. The resulting band structure is shown in Fig. 2.1b (blue line) and can be described by [5]:

$$E(k) = \pm\sqrt{\frac{\gamma_1^2}{2} + \frac{U^2}{4} + (\hbar v k)^2 - \sqrt{\frac{\gamma_1^4}{4} + (\gamma_1^2 + U^2)(\hbar v k)^2}} \tag{2.2}$$

where $v = \sqrt{3}\gamma_0 a_0/(2\hbar)$ with a_0 the spacing between neighboring sites within one layer. From equation 2.2 the band gap can be determined [5]:

$$E_{gap} = \frac{|U|\gamma_1}{\sqrt{U^2 + \gamma_1^2}}$$

2.2 Electrostatics of dual-gated bilayer graphene

Dual-gated bilayer graphene can be modeled as two parallel conducting plates separated by the interlayer spacing $c_0 = 0.335$ nm with surface charges σ_1 and σ_2 (see Fig. 2.1c). The back gate (top gate) is separated from the graphene by a medium with dielectric constant ϵ_{BG} (ϵ_{TG}) and thickness $\mathrm{d_{BG}}$ ($\mathrm{d_{TG}}$). The electric fields can be related to potential differences:

$$\mathcal{E}_{\mathrm{BG}} \approx V_{\mathrm{BG}}/d_{\mathrm{BG}} \qquad \mathcal{E}_{\mathrm{TG}} \approx -V_{\mathrm{TG}}/d_{\mathrm{TG}} \qquad \mathcal{E} = (V_1 - V_2)/c_0 = U/(ec_0) \tag{2.3}$$

where U is the interlayer asymmetry. Application of Gauss's law gives the following relations for the charge carrier density n and U [33]:

$$n = n_1 + n_2 = \frac{\epsilon_0 \epsilon_{\mathrm{BG}}}{e d_{\mathrm{BG}}} V_{\mathrm{BG}} + \frac{\epsilon_0 \epsilon_{\mathrm{TG}}}{e d_{\mathrm{TG}}} V_{\mathrm{TG}} + n_{\mathrm{BG},0} + n_{\mathrm{TG},0} \tag{2.4}$$

$$U = \frac{c_0 e}{2}\left(\frac{\epsilon_{\mathrm{BG}}}{\epsilon_{\mathrm{R}} d_{\mathrm{BG}}} V_{\mathrm{BG}} - \frac{\epsilon_{\mathrm{TG}}}{\epsilon_{\mathrm{R}} d_{\mathrm{TG}}} V_{\mathrm{TG}}\right) + \frac{c_0 e}{2} \frac{e}{\epsilon_{\mathrm{R}} \epsilon_0} (n_{\mathrm{BG},0} - n_{\mathrm{TG},0}) + \frac{c_0 e}{2} \frac{e}{\epsilon_{\mathrm{R}} \epsilon_0} (n_2 - n_1) \tag{2.5}$$

where $n_{\mathrm{BG},0}$ and $n_{\mathrm{TG},0}$ account for chemical doping of the graphene in absence of any applied voltages. The last term in equation 2.5 shows that the interlayer asymmetry depends on the difference between the charge carrier densities of the individual layers. These densities depend on the interlayer asymmetry, because of its appearance in the band structure (equation 2.1) . The problem therefore requires a self-consistent calculation, but it can be simplified in the limit where screening is neglected. In that case, the last term of equation 2.5 vanishes. The terms involving $n_{\mathrm{BG},0}$ and $n_{\mathrm{TG},0}$ can be rewritten in terms of offset voltages $V_{\mathrm{BG},0}$ and $V_{\mathrm{TG},0}$. This simplifies equations 2.4 and 2.5:

$$n = \beta(V_{\mathrm{BG}} - V_{\mathrm{BG},0}) + \alpha(V_{\mathrm{TG}} - V_{\mathrm{TG},0}) \tag{2.6}$$

$$\mathcal{E} = \frac{\beta e}{2\epsilon_0}(V_{\mathrm{BG}} - V_{\mathrm{BG},0}) - \frac{\alpha e}{2\epsilon_0}(V_{\mathrm{TG}} - V_{\mathrm{TG},0}) \tag{2.7}$$

where $\alpha = \epsilon_0 \epsilon_{\mathrm{TG}}/(e d_{\mathrm{TG}})$ and $\beta = \epsilon_0 \epsilon_{\mathrm{BG}}/(e d_{\mathrm{BG}})$ and we used that $\epsilon_{\mathrm{R}} = 1$ in between the graphene layers. As an example, the charge carrier density and electric field as a function of V_{BG} and V_{TG} for a $\beta = \alpha = 5 \times 10^{11}$ $\mathrm{V^{-1}cm^{-2}}$ is shown in Figs. 2.2a,b respectively.

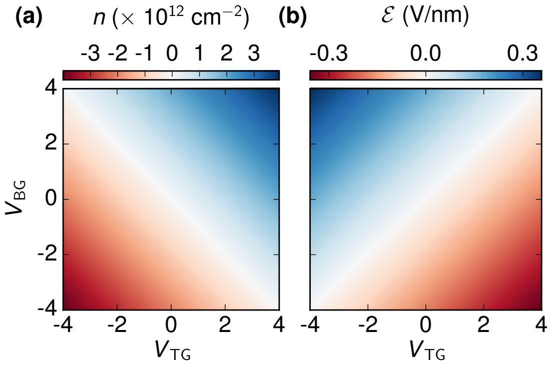

Figure 2.2: (a) Charge carrier density as a function of V_{TG} and V_{BG} as given by equation 2.6 for $\beta = \alpha = 5 \times 10^{11}$ V^{-1}cm^{-2}. (b) Electric field as a function of V_{TG} and V_{BG} as given by equation 2.7.

2.3 Optical measurements of the band gap

The first experimental evidence for the bilayer graphene band gap was obtained by Ohta et al. [40]. They perform angle-resolved photo-emission spectroscopy of bilayer graphene grown on SiC to map out the band structure. The doping and the electric field are changed by the deposition of potassium atoms onto the surface. This has the same effect as a changing top gate voltage and the resulting process is therefore equivalent to moving along a horizontal line in Fig. 2.2. The initially n-doped sample (equivalent to a positive top gate voltage) shows a transition from a gapped to a gapless and back to a gapped band structure when adding potassium (equivalent to lowering the top gate voltage). With this method it is impossible to quantify the applied electric field however. Zhang et al. [41] performed infrared absorption spectroscopy on dual-gated bilayer graphene. They use a bilayer graphene flake exfoliated on a Si/SiO$_2$ substrate which served as a back gate. Prior to the deposition of the top gate, a layer of Al$_2$O$_3$ is deposited as a gate dielectric. With the combination of the top and back gate the absorption spectra as a function of the electric field in the range of 0 to 3 V/nm is measured whilst keeping the density at zero. The experimentally obtained values for the gap as a function of electric field (on the order of 100 meV for $\mathcal{E} = 1$ V/nm) show good agreement with tight-binding calculations in which screening effects have been taken into account [42].

2.4 Transport measurements of the band gap

In transport measurements the gap size can be determined by measuring the temperature dependence of the resistivity. For an ideal band gap the resistivity follows the Arrhenius law: $\rho \sim \exp(E_{gap}/(2k_BT))$. The first transport measurements [43], performed on bilayer graphene in between SiO$_2$ layers, show an increase of the resistivity at charge neutrality with the electric field $\mathcal{E}$. The green data points in Fig. 2.3a, taken from Ref. [43], show the temperature dependence of the resistivity at charge neutrality ($n = 0$) for $\mathcal{E} = 0.4$ V/nm (Fig. 2.3b shows similar results for $\mathcal{E} = 0.8 - 1.0$ V/nm). The resistivity does not follow the Arrhenius law: rather than

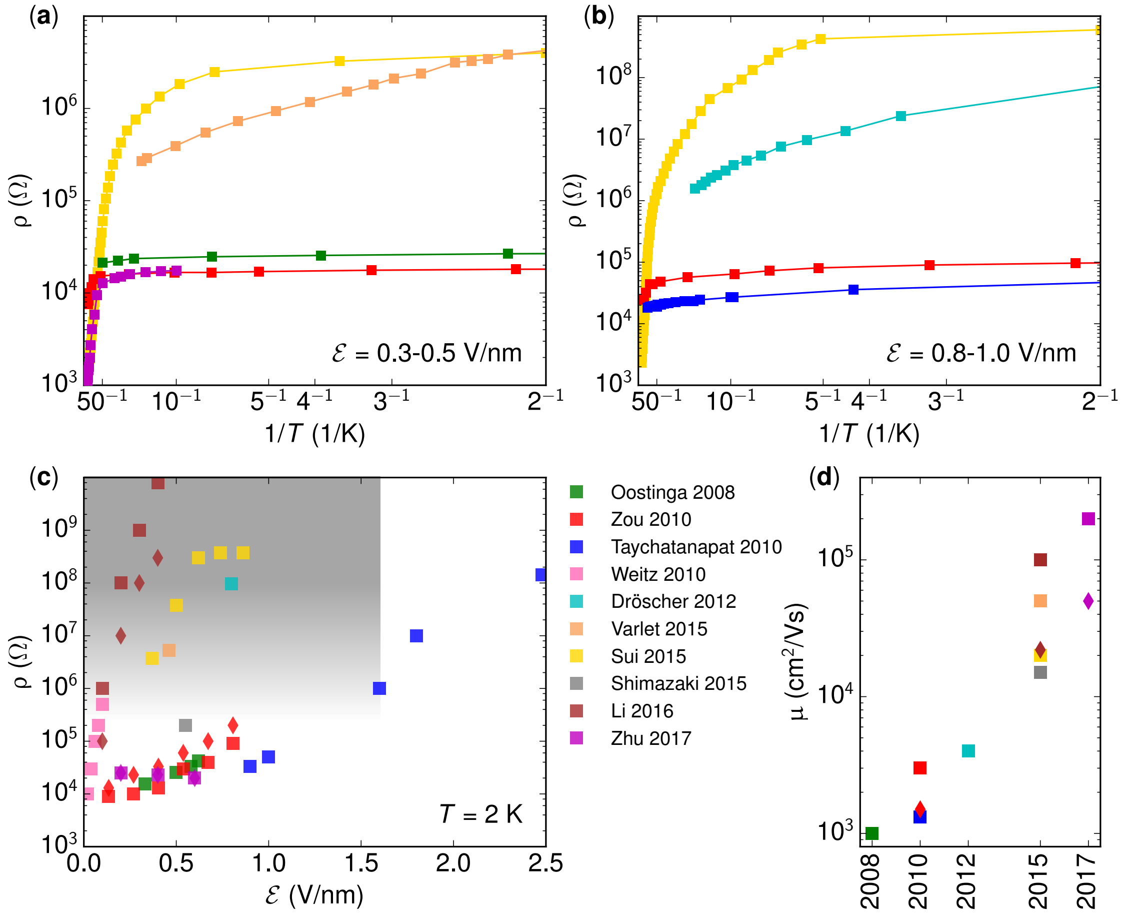

Figure 2.3: (a) Resistivity as a function of temperature in an electric field of $E = 0.3 - 0.5$ V/nm. Different colors denote different references: Oostinga 2008 [43], Zou 2010 [44], Taychatanapat 2010 [45], Weitz 2010 [46], Dröscher 2012 [47], Varlet 2015 [7], Sui 2015 [48], Shimazaki 2015 [49], Li 2016 [50] and Zhu 2017 [51]. (b) Resistivity as a function of temperature in an electric field of $E = 0.8 - 1.0$ V/nm. (c) Resistivity as a function of electric field at $T = 2$ K. Different symbols denote different samples. (d) Mobility as a function of year of publication

showing a steep increase, it saturates at low temperature. The temperature dependence is more accurately described by a power law $\rho \sim (T_0/T)^{1/3}$, which is expected for variable range hopping via mid-gap localized impurity sites. This suggests that improvements of graphene or dielectric quality could lead to a temperature dependence closer to the Arrhenius law. Figure 2.3c shows ρ as a function of $\mathcal{E}$ at $T = 2$ K for this sample and other samples measured in literature.

Zou et al. [44] reported on the temperature dependence over a larger temperature range. Their sample consists of a graphene flake on a Si/SiO$_2$ substrate covered by a dielectric layer of HfO$_2$ and a top gate. Between $T = 220$ K and $T = 140$ K the resistivity can be described by the Arrhenius law (see red line in Fig. 2.3a,b). In high electric fields, the gap size is in agreement with the theoretically predicted gap size. At lower electric fields the measured energy scale is larger than the theoretical prediction. The authors argue that in this regime the energy barrier which needs to be overcome is dominated by the energy scale of the disorder potential. Below $T = 50$ K the resistivity saturates at values similar to the ones found by Oostinga et al. (see Fig. 2.3a), which the authors attribute to hopping via mid-gap states.

The regime of electric fields higher than $\mathcal{E} = 1$ V/nm was studied by Taychatanapat et al. [45]. Their device consists of a graphene flake on a Si/SiO$_2$ substrate covered by an Al$_2$O$_3$ dielectric and a top gate. The high temperature resistivity follows the Arrhenius law with a gap size which is two orders of magnitude smaller than the theoretically expected gap. The authors explain this by impurity bands in the gap arising from negatively charged donors. The low temperature resistivity again shows a saturation, albeit at relatively high values. The authors mention that the typical mobility of the devices before oxide growth ($\mu = 1500 - 2000\text{cm}^2/\text{Vs}$) was 30% higher than the mobility afterwards. This indicates that the dielectric deposition introduces additional impurities, which could lead to a spatially varying band gap.

The reduced sample quality by the deposition of dielectrics was circumvented in the work of Weitz et al. [46] in which the graphene was suspended. The gap size extracted from the temperature dependence between $T = 10$ K and $T = 0.5$ K is an order of magnitude lower than the theoretically expected band gap (higher temperature data is not shown). The authors refer to the possible existence of conducting edge states to explain the discrepancy (see Section 2.5). The resistivity obtained at $T = 2$ K is relatively high given the small electric fields achievable in suspended samples (see Fig. 2.3c).

Dröscher et al. [47] studied the temperature dependent resistivity of a device consisting of a graphene flake on a Si/SiO$_2$ substrate covered by hexagonal boron nitride (hBN). Although the resistivity reached at $T = 2\ K$ is relatively high, the band gap extracted from the temperature dependence measured up to $T = 16.5$ K is an order of magnitude smaller than the theoretical value, which is explained by the presence of mid-gap states.

The problem of disorder induced by the dielectric could be solved by the encapsulation of graphene in hBN, initiated by Dean et al. [26]. Encapsulation resulted in higher mobility samples than the previously mentioned samples on Si/SiO$_2$ (see Fig. 2.3d). Surprisingly, this improved device quality did not change the saturation of the resistivity at low temperatures. The measured resistivity at low temperatures in most encapsulated devices is still below the MOhm range in the works of Shimazaki et al. [49], Zhu et al. [51] and some of the device studied by Varlet et al. [13]. Two notable exceptions are discussed in the works of Varlet et al. [7] and Sui et al. [48]. The temperature dependence of the resistivity of both devices nonetheless saturates at low temperature. Sui et al. extract a gap size in agreement with theory in the temperature range above $T = 70$ K.

Two samples showing particularly high resistivity where presented by Li et al. [50]. They consist of a graphene flake encapsulated in hBN on top of a graphite back gate. These samples show a saturation of the temperature dependence at low temperature as well.

In conclusion, all samples mentioned in this section showed a resistivity which saturates below the theoretically expected value at low temperature. Hopping transport via mid-gap states is a widely suggested explanation. Two other explanations are discussed in the next section.

2.5 Explanations of conduction in the gap

2.5.1 Conduction along the edge

In 2008 Castro et al. [52] calculated that the band structure of a perfect zigzag bilayer graphene nanoribbon has zero-energy states propagating along the edges irrespective of the interlayer asymmetry, which leads to a minimal conductance of $G = 4\ e^2/h$. In practice most samples have irregular edges, but the tight-binding simulations by Li et al. [53] suggested that these conductive edge states also exist in samples with disordered edges, yet with lower conductance. Surprisingly, they find that the edge conductance cannot be suppressed but it saturates at a finite value for sufficiently disordered structures.

Experimental evidence for edge conduction was found in Refs. [51, 54]. In these works superconducting contacts are used to induce superconductivity in bilayer graphene by the proximity effect. By taking the Fourier transform of the critical current as a function of magnetic field, the spatial current distribution can be found. At low charge carrier densities enhanced current flow along the device edges is found in both works. While Allen et al. [54] observe enhanced edge conduction in pristine monolayer and bilayer graphene and argue that this is due to band bending induced by the potential at the edges of the device, Zhu et al. [51] find the edge conduction only in devices with an induced band gap. Because of this they exclude the potential profile and chemical doping along the edges as possible causes. They attribute the edge conduction to either the aforementioned conduction along zigzag edge segments or valley currents induced by the valley Hall effect which get squeezed towards the edge.

Zhu et al. also investigated gapped monolayer graphene. This material can be gapped when the rotation angle with the underlying hBN substrate is small and a superlattice arises [55]. They observe edge currents in gapped monolayer graphene too. Scanning gate microscopy measurements on similar devices by Dou et al. [56] show evidence for edge states in a low but not in a high mobility device. They therefore conclude that the observed edge currents stem from chemical doping of the edges.

2.5.2 Conduction along domain walls

After Martin et al. [57] put forward the existence of chiral states at the boundaries between bilayer graphene regions with opposite electric field polarity, the existence of similar one-dimensional states along domain walls between AB and BA stacked bilayer graphene was predicted [58, 59]. These AB-BA domain walls occur naturally in bilayer graphene, but cannot be observed in atomic force microscopy images. Ju et al. [60] could locate them using near-field infrared nanoscopy. In absence of inter-valley scattering processes the channels along the domain walls should exhibit an ideal conductance of $G = 4\ e^2/h$. The authors study several bilayer graphene devices on a Si/SiO$_2$ substrate covered by an Al$_2$O$_3$ dielectric and a top gate, with and without domain walls. In the devices without domain walls, the resistivity at charge neutrality at $T = 4.2$ K increases from $R = 4$ kΩ without electric field to $R = 80$ kΩ for the maximal applied electric field. For devices in which a domain wall is present, the resistivity in an electric field saturates around $R = 14$ kΩ. For all devices with domain walls the minimal conductance is between $G = 2\ e^2/h$ and $G = 4\ e^2/h$, where shorter devices ($L = 200$ nm) show a conductance closer to the theoretically predicted value of $G = 4\ e^2/h$. The authors conclude that the deviation is due to inter-valley scattering and suggest that encapsulation of bilayer graphene in hBN could result in devices with a conductance closer to the ideal value. Scanning tunneling microscopy measurements which probe the local density of states have confirmed the existence of states within the gap at AB-BA domain walls [61].

2.6 Implications for nanostructures

The ability to form highly resistive gapped regions is crucial for the electrostatic definition of nanostructures. Domain walls and edge currents should be avoided when making tunnel barriers. Although domain walls cannot be detected with the equipment we have at hand, in practice they do not form a problem since they occur only rarely[1]. Avoiding edge currents is potentially a bigger issue, since up to date there is no agreement on the cause of the edge currents.

hBN encapsulation has resulted in high quality graphene, as witnessed by the high mobility of the devices reported on in 2015 and later. In practice, hBN encapsulation sets an upper limit on the applied electric fields. The onset of leakage currents for a pristine hBN flake of thickness t usually occurs around a voltage $V = 0.5\ \mathrm{V/nm} \times t$ [2]. This limits the electric fields which can be applied to a maximum of $\mathcal{E} = 1.6$ V/nm. For hBN which has been exposed to reactive ion etching, the onset of leakage possibly occurs at lower electric fields.

The resistance of tunnel barriers in high quality quantum devices should largely exceed the resistance quantum $R_\mathrm{K} = 25.8$ kΩ [9]. In practice this translates to a resistivity within the gray region in Fig. 2.3c. The vertical boundary of this region is

---

[1] We thank Professor Lin He for this information

[2] We thank Aroosa Ijaz and Peter Rickhaus for this information.

set by the aforementioned onset of leakage currents in hBN. Despite the saturating resistivity at low temperatures observed in all samples, a few samples discussed in this chapter fall within this region. A question which will be answered in this thesis is how to make samples which systematically end up in the regime of high resistivity.

Chapter 3

Fabrication of gated bilayer graphene devices

3.1 Introduction

The first graphene devices consisted of a graphene flake on a Si/SiO_2 substrate [1]. Surface roughness and charged impurities induced significant disorder in these devices, leading to low mobility and a short mean free path. During the fabrication process the graphene flakes also got in contact with resist layers and other chemicals, which leave residues behind. These residues induce a nonuniform doping in graphene, reducing the device quality even more. Two ways of improving the quality of graphene devices were found: suspension [62] and encapsulation by hexagonal boron nitride [26, 27]. Since our experiments require both top gates and back gates, we work with encapsulated graphene. Fabricating top gates and applying large displacement fields to suspended devices is technologically much more challenging.

After encapsulation the graphene flake is contacted by etching trenches, defined by an e-beam lithography mask, in the hBN and deposition of metal in these trenches. Another e-beam lithography step is performed to add a top gate structure to the device. In case a second layer of top gates is required, a layer of dielectric (Al_2O_3) is deposited before the last e-beam step to define the additional top gate layer. In this chapter all steps of this process are discussed in detail.

3.2 Substrate chip preparation

To exfoliate graphene we use chips made from commercial Si/SiO_2 wafers. For a good contrast of graphene flakes in the optical microscope, the thickness of the top SiO_2 layer has to be 90 nm or 285 nm. At the start of this thesis project, we worked with chips with a marker pattern defined by optical lithography. This provides a convenient coordinate system to locate flakes. During the optical lithography process the wafer surface gets in contact with chemicals and solvents though. We tried to clean the surface with acetone and isopropanol, by UV-ozone cleaning and by plasma ashing. Neither of these methods resulted in a cleanliness of the chip comparable to the cleanliness of the wafer prior to our processing. We therefore concluded that for the exfoliation, where cleanliness is critical, it is better to work with unprocessed substrate chips without markers. Once the graphene is encapsulated in hBN cleanliness is less important and the stack can be deposited on a chip with markers. The markers make it easier to align the e-beam lithography masks used in later fabrication steps. Details of the fabrication of the marker chips can be found in Refs. [13, 63]. After sawing the wafer the marker chips are still covered by a protective layer of photoresist. This layer can be dissolved by putting the chips in an acetone bath at 50 °C for two hours.

3.3 Exfoliation of 2D crystals

To deposite flakes of 2D materials onto chips, a piece of blue tape[1] is used. For graphene exfoliation a shiny flake of graphite is selected and is pressed onto the tape and removed from the tape again, leaving some pieces of graphite behind. For hBN exfoliation some small pieces of hBN crystal are selected and put on the tape. Afterwards the tape is folded together between 10 and 20 times to achieve a homogeneous density of graphite/hBN on the tape. We then press about 8 Si/SiO_2 chips onto the tape. Each chip is pressed for about 10 s, whilst avoiding any shearing motion of the chip. At this stage one can choose to wait for about 5 minutes, which presumably leads to the adhesion of larger flakes to the chips. The chips are then peeled off from the tape in a smooth and slow movement.

3.4 Selection of graphene flakes

The chips with flakes are examined under the optical microscope to find suitable flakes for devices. Figure 3.1a shows a picture of a chip taken with the 10 x objective. This picture is used to find a flake back at a later stage. The dark and bright dots are graphite flakes. A zoom into the white square is shown in Fig. 3.1b. The flake marked with the red arrow is a bilayer graphene flake. This can be seen from the color. By extracting the intensity of the green component of the RGB color space I_g from the image, we can determine the green contrast[2]:

$$GC = \frac{I_{g,flake} - I_{g,substrate}}{I_{g,substrate}} = 0.3 \pm 0.05 \text{ for bilayer graphene}$$

Another method to determine the number of layers is to perform Raman spectroscopy and to determine the full width at half maximum of the $2D$-peak, which is

---

[1] Nitto Denko Corporation ELP BT-150E-CM

[2] The precise numbers may vary depending on the microscope settings

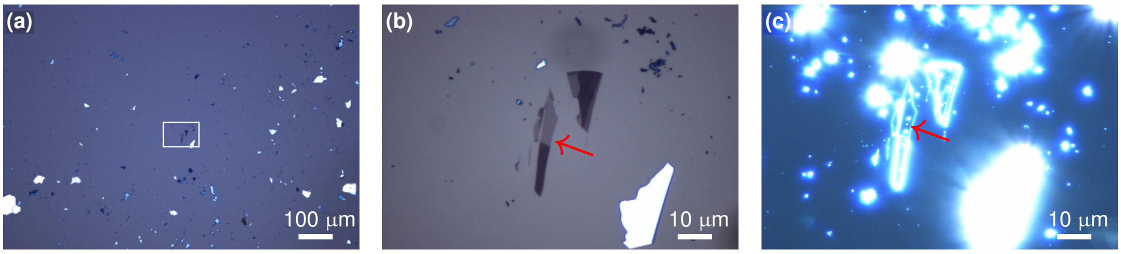

Figure 3.1: (a) Optical microscope image of a Si substrate with graphite flakes (dark and bright spots) (b) Zoom in the rectangle indicated in (a). The red arrow indicates a bilayer graphene flake (c) Dark field image of (b) with a 10 s exposure time. Contaminations of the flake show up as bright dots (red arrow).

between 45 cm^{-1} and 56 cm^{-1} for bilayer graphene [64]. Using the green contrast is the preferred method however, since it is faster and sufficiently reliable.

To determine the cleanliness of the flake we take dark field pictures with 10 s exposure time, as shown in Fig. 3.1c. The flake in the picture is not entirely clean, as can be seen from the white spots on the surface (see red arrow). It should be noted that flakes with contaminants like this one can still result in clean devices: during the stacking and annealing process the contaminants tend to assemble in bubbles and bubble free areas can be selected for the device.

3.5 Selection of hBN flakes

Chips with hBN flakes are examined under the optical microscope as well. Suitable flakes are between 15 and 50 nm high and have an area of at least 20×10 $\mu\mathrm{m}^2$ without any cracks or steps. The height can be roughly determined from the color (see Fig. 3.2) and more precisely with atomic force microscopy (AFM).

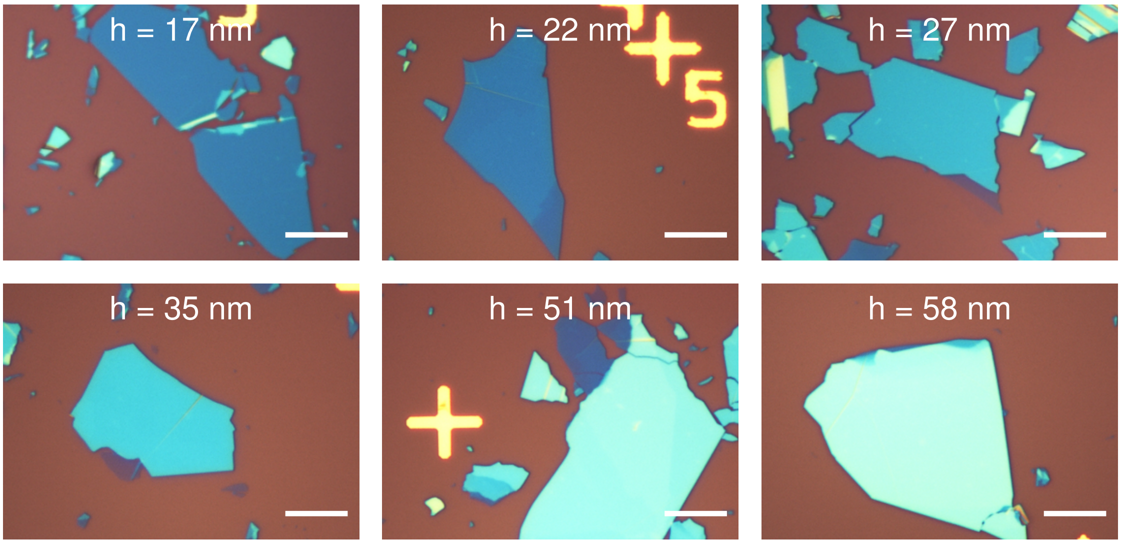

Figure 3.2: Optical microscope images of hBN flakes on chips with markers. The color of the flake is determined by its thickness. The scale bar is 10 μm.

3.6 Stacking of flakes

To create a stack of graphene and hBN layers we use a micromanipulator. We prepare a glass slide with a polymer stamp to which the flakes adhere. The process is adapted from Refs. [27, 65]. It is illustrated in Fig. 3.3. The glass slide with polymer stamp and exfoliated hBN is aligned and brought slowly in contact with a chip with a graphene flake (3.3a). The chip is mounted on the stage of the micromanipulator, which is set to a temperature of 110 °C. Because of the strong van der Waals interaction between graphene and hBN the two materials stick together when retracting the glass slide (3.3b). In the next step, the glass slide is brought in contact with another hBN flake (3.3c). For samples where Si is used as the back gate the stack is now finished. By increasing the temperature the polymer can be melted and the glass slide can be retracted, leaving the stack on the chip. When making a sample with a graphite back gate, the stack is lifted up once more (3.3d). It is then brought in contact with a graphite flake (3.3e) and finally the polymer is melted and the glass slide can be removed (3.3f). We used two different types of polymer stamps for this process, which are discussed in the next paragraphs.

MAA/MMA glass slides

The first type consisted of a thin layer of commercially available PDMS, cut into pieces of around 1×1 cm^2, on which a layer of MAA/MMA is spun (see Ref. [13] for process details). Afterwards hBN is exfoliated onto this stamp and suitable flakes are located. For melting the MAA/MMA the temperature of the stage is increased to 125 °C. After the stacking process the chip is put in an acetone bath at 50 °C

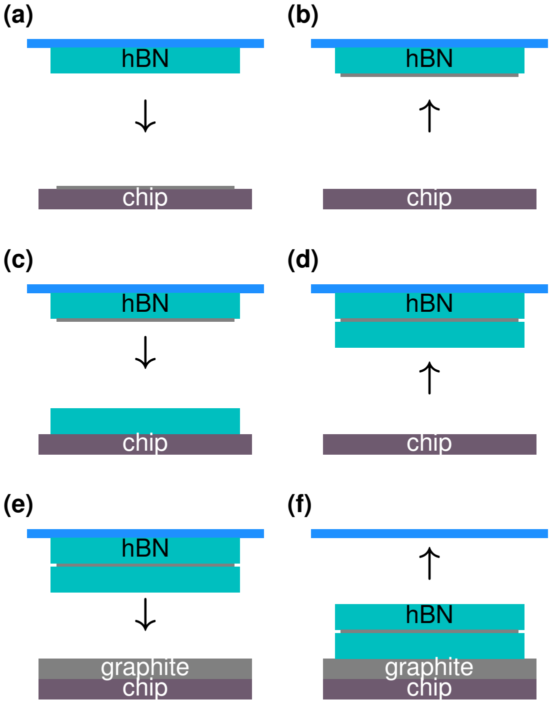

Figure 3.3: Schematics of the stacking process. (a) A hBN flake on a glass slide(blue) with a polymer stamp is brought in contact with a graphene flake (gray) on a chip. (b) Because of the strong van der Waals interaction between graphene and hBN the two materials stick together when retracting the glass slide. (c),(d) Same process as (a),(b) where now a hBN flake is picked up. (e) The stack is placed on a graphite flake. (f) By melting the polymer the glass slide can be retracted.

to dissolve residues of the polymer stamp. There are several disadvantages of this stacking technique:

- When exfoliating hBN onto the stamps it sometimes happens that most of the MAA/MMA film is ripped off and no hBN is left behind. We tried different types of resist for the film, different baking processes and different ways of removing the tape from the stamp, but the problem kept occurring.
- Since the MAA/MMA is not very sticky, it sometimes happens that a flake is accidentally deposited when aiming to pick up another flake. (E.g. after the step in 3.3a one would end up with hBN and graphene on a chip).
- It can be tough to get the right region of the stamp in contact with the chip. When approaching the substrate, the glass slide sometimes gets stuck before the desired flakes are in contact, because of a wrong tilt angle. Correcting for this in the micromanipulator set-up is a laborious process.

PC glass slides

The second type of stamp consisted of a much thicker, home grown PDMS layer to which a film of PC is attached (process details can be found in Ref. [66]). The PC is stickier than the MAA/MAA, so the initial hBN flake can be picked up from a substrate chip and unintended depositions of flakes do not occur. The stamp is considerably thicker, which on the one hand makes it challenging to locate graphene flakes below the stamp in the micromanipulator, but on the other hand makes adjustments of the position of the stamp much smoother. A wrong tilt angle can simply be corrected by rolling over to the desired spot. The visibility of the flakes below the stamps can be improved by using a Normarski prism. For melting of the PC stamps a temperature of 160 °C is required. Residues of the polymer stamp on the stack can be removed by putting the sample in chloroform for 10 minutes.

The second type of glass slides resulted in a considerably higher yield of the stacking process. For an overview of more techniques employed in the community, see Ref. [67].

Bubble formation

As mentioned in section 3.4 contaminants are present on the surface of flakes. As soon as the flakes are exposed to air they adsorb water, atmospheric gasses and hydrocarbons. During the stacking process the contaminants tend to form bubbles between the layers, leaving behind clean areas of the flakes. This process is also referred to as ‘self-cleaning’. Figure 3.4a shows an example of an AFM image of a stack with bubbles. The position of the graphene is indicated by white dashed lines. Graphene in bubbly regions is usually more disordered, which results in a low device mobility. To make (quasi-)ballistic devices, bubble free regions should be selected. The bubbles occur in various densities and in various sizes. Up to a certain extent cleaner flakes lead to cleaner stacks, but the efficiency of the ’self-cleaning’ process also plays an important role. It is generally assumed that when the layers are brought in contact more slowly, the efficiency of the cleaning process is bigger [67]. We observed that for contacting speeds smaller than roughly 5 μm/s no significant improvement occurs by reducing the speed.

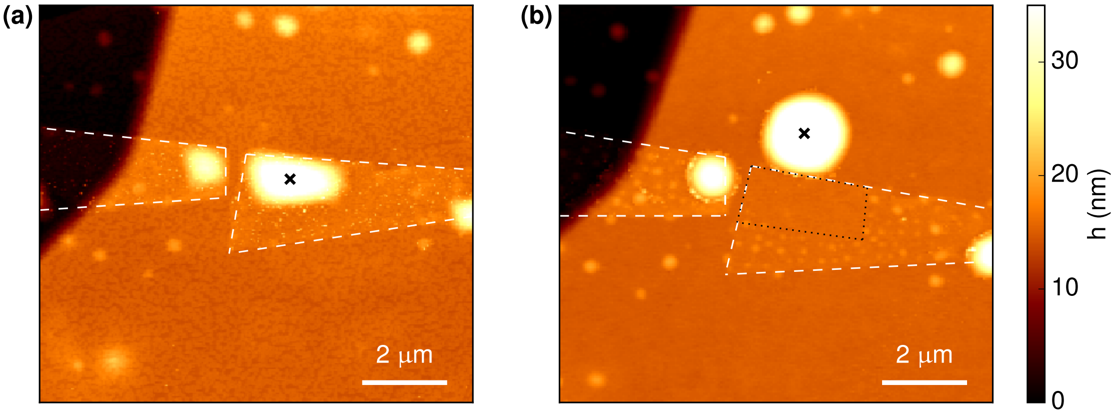

Figure 3.4: (a) AFM image of a graphene flake (delimited by the dashed white lines) encapsulated between hBN layers (brown and orange). Bubbles are present in the stack. (b) AFM image of the same region after thermal annealing. The bubble marked with the black cross has moved and left behind a clean graphene area, delimited by the dotted black line.

3.7 Thermal annealing

The bubbles in graphene stacks can gather even more contaminants during thermal annealing. The thermal annealing step also makes sure that the bubbles will not move around anymore during further steps of the fabrication process. It is performed in a tube oven with an Ar flow of 2 L/min and a H_2 flow of 0.2 L/min. Over the course of two hours the temperature is ramped up to 320 °C. The sample remains at this temperature for 3 hours before cool down. The result of the annealing process can be seen in Fig. 3.4b. The big bubble marked with the black cross has moved away from the graphene and a flat and clean graphene area (indicated by the black dotted line) is left behind.

3.8 Contacting the graphene

Figure 3.5a shows an optical microscope image of a finished stack with a schematic cross section of the device below. The stack consists of a graphite back gate (outlined in pink), a bottom hBN flake (outlined in white), a graphene flake (outlined in red) and a top hBN flake (outlined in green). The next step is to create contacts to the graphene.

The contacts to the graphene are defined by e-beam lithography. The contacting process is based on Ref. [27] and process details can be found in Ref. [63]. Before the application of e-beam resist, the sample is exposed to a mild oxygen plasma for 20 s at a power of 200 W. This increases the adhesion of the resist to the chip surface

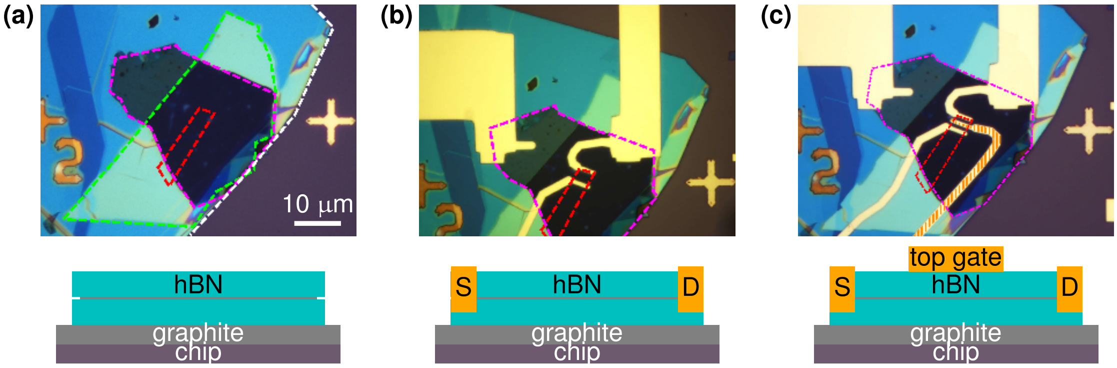

Figure 3.5: (a) Top: Optical microscope image of a finished stack. The graphite back gate is outlined in pink, the bottom hBN is outlined in white, the graphene is outlined in red and the top hBN is outlined in green. Bottom: schematic of a cross section of the device (b) Top: optical microscope of the same device after two contacts have been added to the graphene and one contact has been added to the graphite gate. Bottom: cross section of the device with the added source and drain contacts (S,D) (c) Top: Optical microscope image after deposition of a top gate (highlighted in orange) Bottom: corresponding cross section.

in general and to the extremely flat hBN surface in particular. The e-beam mask consists of fine markers which allow for precise alignment of following e-beam steps and trenches for the contacts. These are etched into the structure by reactive ion etching. For samples with a graphite back gate it is essential to control the etching depth of the process: etching too deeply will result in contacts which connect the graphite back gate and the graphene layer (see schematic in Fig. 3.5b). The etching depth can be controlled by setting a desired etching time, since the etching rate for the employed CHF_3/O_2 recipe is constant at 48 nm/min. After etching 10 nm of Cr and 50 nm of Au is deposited in the trenches to form the contacts. The result can be seen in Fig. 3.5b. Using a probe station the contacts can be checked for Ohmic behavior by applying a DC bias within the range of ±5 mV. The probe station can also be used to verify that the graphene layer and the graphite back gate are not connected.

3.9 Definition of top gates

The top gate design is written with e-beam lithography as well. After the development of the e-beam lithography pattern the sample is exposed to a short reactive ion etching recipe with Ar and O_2. This roughens the hBN surface which increases the adhesion of the metal of the top gates. Figure 3.5c shows an optical microscope image of a sample with a top gate. An AFM picture of a different sample with four split gates can be seen in Fig. 3.6a. The source and drain contacts are denoted by

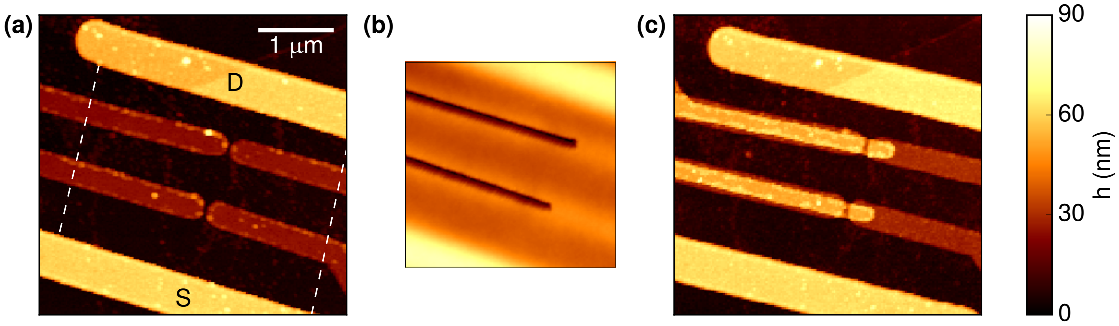

Figure 3.6: (a) AFM image of a stack with two contacts, labeled S and D, and four split gates. White dashed lines indicate the edges of the encapsulated graphene flake. (b) AFM image to check the alignment of the e-beam lithography mask for the definition of the upper gate layer. The whole structure is covered with 140 nm of resist, except for the trenches where the upper gates will be deposited. The trenches are well aligned with the underlying split gates. (c) Final device geometry after deposition of metal in the trenches defined in (b)

S and D and the edges of the encapsulated graphene flake are indicated by white dashed lines.

For fine gate patterns (features smaller than 100 nm) a thinner resist layer is used to increase the resolution of the e-beam pattern. The resolution is furthermore improved by developing the e-beam resist in a solution of isopropanol and water (3:1) at 0 °C [68]. To make sure that the lift-off process works well for these fine patterns only 20 nm of metal is deposited in this case.

3.10 Deposition of a dielectric layer

To isolate a next layer of top gates from the first layer of top gates, two dielectrics were considered: hBN and Al_2O_3. The deposition of an additional layer of hBN onto the processed stacks is difficult. To avoid damaging the stack, we use the less invasive 'PMMA carrying layer transfer method' to deposit the hBN [13, 26, 67]. With this method it is challenging to bring the hBN to the desired location and make it stick there. During the removal of the PMMA the additional hBN layer would sometimes detach as well. The yield of the fabrication process could be improved by depositing a dielectric layer of Al_2O_3 at 150 °C by atomic layer deposition. When using fine top gate structures that are 20 nm high, an Al_2O_3 layer of 30 nm results in good isolation between the top gate layers. Thicker Al_2O_3 layers should be avoided as it makes the wire bonding process harder.

3.11 Definition of upper gate layer

The deposition of a final layer of upper gates can be done in the same way as the deposition of the first layer of top gates. To check the alignment of the gate layers AFM can be used prior to the metal deposition. An example is shown in Fig. 3.6b, where the entire device is covered with 140 nm of resist except the dark trenches which define the upper gate layer. The final device geometry is shown in Fig. 3.6c.

Chapter 4

Comparison of exfoliated graphene and CVD grown graphene

In this chapter we compare the quality of exfoliated bilayer graphene and bilayer graphene grown by chemical vapor deposition (CVD). We discuss characterization measurements of both materials. Exfoliated graphene flakes have a typical extent of a few to tens of micrometers. CVD grown graphene on the other hand has a typical size of hundreds of micrometers [69], but can reach lengths of 100 m [70]. Another interesting possibility when using CVD growth is the use of a pure Carbon-12 source. Natural graphite has a small fraction of Carbon-13 atoms, which do have a nuclear spin. Carbon-12 is nuclear spin free and therefore electron spins in this material do not suffer from decoherence caused by hyperfine interactions.

Up until recently however, the mobility and mean free path in CVD graphene were lower than that measured in exfoliated crystals. Signatures of ballistic transport in monolayer CVD graphene were reported by Calado et al. [71]. The method to transfer the graphene from the Cu foil on which it is grown to a hBN substrate involved contact between graphene and polymer layers, resulting in the formation of bubbles containing contaminants in between the hBN and graphene layers. After annealing at $T = 600°$ C atomic force microscopy was performed to identify micron-sized bubble-free regions. Ballistic transport was observed only in these regions. In 2015 Banszerus et al. [69] discovered that monolayer CVD graphene can be picked up from a Cu foil using a hBN flake on a polymer stamp (similar to the method described in section 3.6) after sufficient oxidation of the foil. This reduced the problem of bubble formation significantly. They demonstrated a mean free path exceeding 28 μm in devices made with this technique [72].

In this chapter we compare transport measurements at $T = 1.7$ K of encapsulated bilayer graphene samples made with exfoliated [1] and CVD grown bilayer graphene. The bilayer graphene was grown by Ming Huang in the group of professor Rodney Ruoff. A CuNi foil was used as a substrate for the growth process. With the Ni content the ratio of bilayer graphene and monolayer graphene can be tuned. We

---

[1] The sample with exfoliated graphene is the same as sample C in Chapter 5.

used the transfer process described in section 3.6 to remove the graphene from the CuNi foil. In the next sections, we will discuss the geometry of the device, transport measurements at $B = 0$ T, Fabry-Pérot oscillations and magnetotransport.

4.1 Device geometry

A schematic of the samples studied in this chapter is shown in Fig. 4.1a. The samples consist of a bilayer graphene flake encapsulated in hBN with two contacts (labelled S and D) to probe the transport. The charge carrier density in the graphene can be changed by applying a voltage to the Si back gate. With the top gate (TG) the charge carrier density in the middle region of the device can be changed. The dimensions of the samples can be found in Table 4.1.

graphene type	**CVD**	**exfoliated**
sample width W (μm)	1.8	1.1
sample length L (μm)	1.3	1.0
top gate length L_{TG} (μm)	0.5	0.5
top hBN (nm)	19	28
bottom hBN (nm)	33	39

Table 4.1: Dimensions of the CVD grown sample and the exfoliated sample

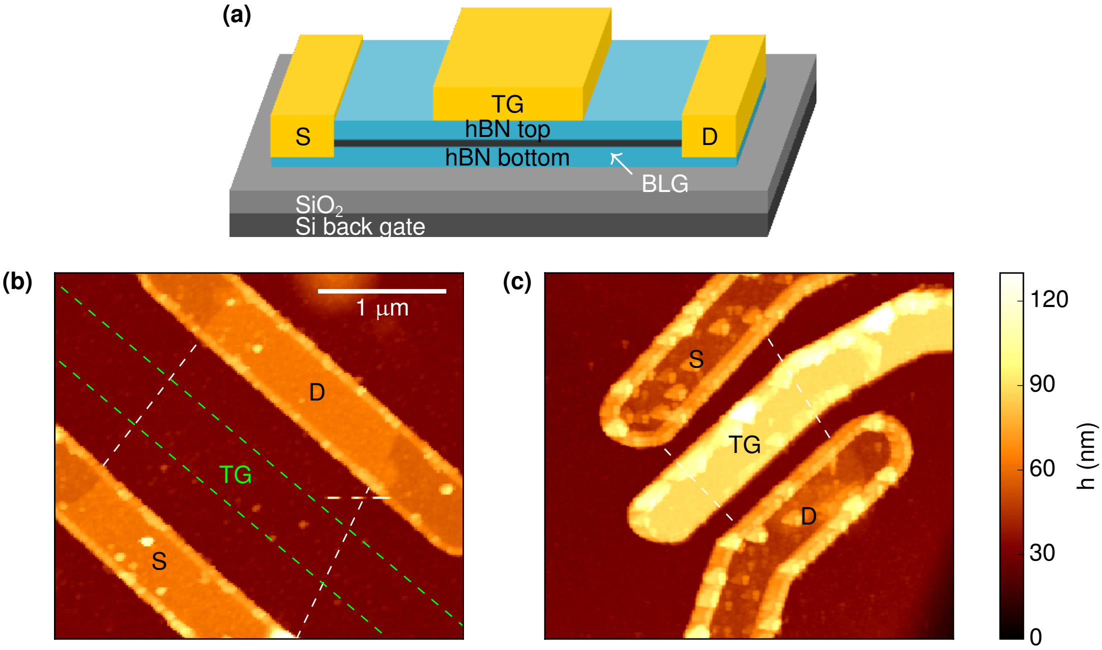

Figure 4.1: Sample geometry (a) Schematic drawing of the BLG samples encapsulated in hBN with source and drain contacts (S,D), a top gate (TG) on top and a Si back gate below. (b) AFM image of the sample with CVD grown graphene (edges denoted by the white dashed lines) prior to the deposition of the top gate (marked by the green lines). (c) AFM image of the sample with exfoliated graphene. The brighter lines around the contacts are artificial and are caused by a blunt AFM tip.

4.2 Conductance at $B = 0$ T

The conductance as a function of top gate voltage and back gate voltage of the CVD graphene and the exfoliated graphene can be seen in Fig. 4.2a,b respectively. Both measurements show a horizontal line of low conductance. This is the charge neutrality point in the outer region of the device, which is not affected by the top gate voltage. Above this line the outer region is n-doped and below it is p-doped. The corresponding shift of the Fermi level in the band structure is schematically drawn in Fig. 4.2c. When comparing the two samples, we note that the conductance dip of the CVD grown sample is relatively broad compared to the conductance dip of the exfoliated sample. This is an indication that the latter is of higher quality [62].

The diagonal line of low conductance is the charge neutrality point of the middle region of the device. The charge carrier density in this region is affected by both the top gate voltage and the back gate voltage, as described by equation 2.6. Along the diagonal line the electric field in the region under the top gate increases in the direction of the arrow. This is why the band structure of the inner region at the

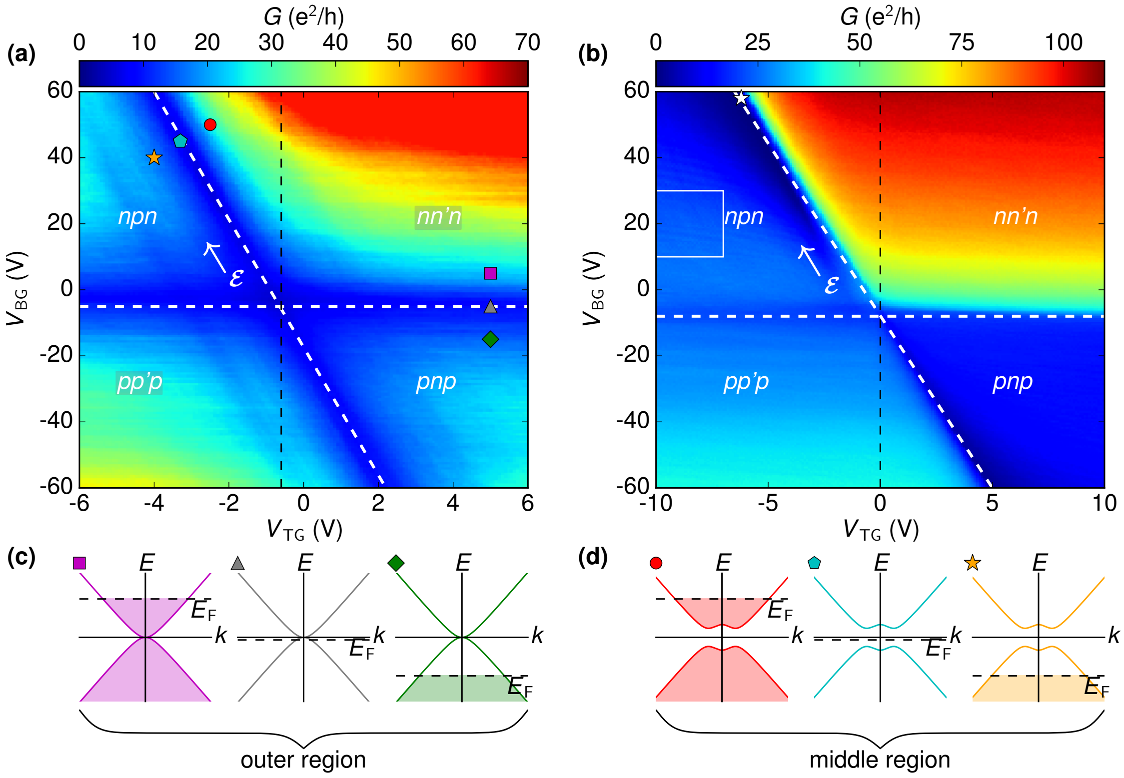

Figure 4.2: (a) Conductance of the CVD graphene sample as a function of top gate and back gate voltage. (b) Conductance of the exfoliated graphene sample as a function of top gate voltage and back gate voltage. (c) Band structure and Fermi level in the outer region of the device at the positions of the markers in (a). (d) Band structure and Fermi level in the middle region of the device at the positions of the markers in (a).

position of the red circle, the blue pentagon and the orange star has a band gap (see Fig. 4.2d). For the CVD graphene sample the conductance along the diagonal line stays more or less constant when the band gap opens. This is an indication that the energy scale related to the disorder potential is larger than the band gap. For the device made with exfoliated graphene a decrease of the conductance with increasing electric field is observed. Because of the opening band gap, the resistance of this sample goes up to $R = 200\ \mathrm{k\Omega}$ at the position marked by the white star in Fig. 4.2b.

For both samples the conductance in the $pp'p$ regime is considerably lower than the conductance in the $nn'n$ regime. This can be explained by the presence of n-doped regions close to the leads, which are caused by the contact with Cr atoms in the leads [27, 73]. In the case of $pp'p$ doping the conductance is lower because of the formation of p-n junctions close to the contacts.

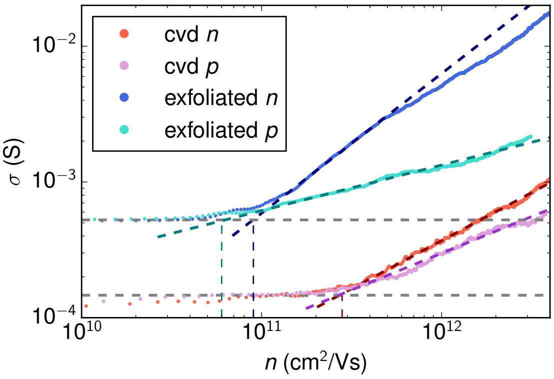

Figure 4.3: Conductivity as a function of charge carrier density. For both samples we can distinguish a regime at high density where the conductance increases with increasing charge carrier density and a regime at low density where the conductivity is constant.

graphene type	**CVD**	**exfoliated**
disorder density $\boldsymbol{n}$ ($\times 10^{11}$ cm^{-2})	3	0.9
disorder density $\boldsymbol{p}$ ($\times 10^{11}$ cm^{-2})	3	0.6
mobility n ($\times 10^4$ cm^2/(Vs))	0.4	4
mobility p ($\times 10^4$ cm^2/(Vs))	0.4	6

Table 4.2: Disorder density and mobility of the CVD grown sample and the exfoliated sample

4.3 Mobility

To determine the mobility of the samples we focus on the conductivity along the black dashed line in Fig. 4.2a,b. Along this line the carrier density in the device is uniform. Using a capacitance model as shown in equation 2.6, the back gate voltage axis can be converted into a density axis. Fig. 4.3 shows the conductivity of both samples for n and p doping as a function of charge carrier density with a log-log scale. At low charge carrier density charged impurities in the sample define an electrostatic potential consisting of electron and hole puddles [74]. Changing the gate voltage in the low density regime merely leads to a redistribution of charge carriers within these puddles. At higher density, above the disorder density (marked by the vertical dashed lines in Fig. 4.3), the conductivity increases with increasing charge carrier density.

The disorder density and corresponding mobilities extracted from the data in Fig. 4.3 can be found in Table 4.2. The lower disorder density and higher mobility of the exfoliated sample are indications that the exfoliated graphene is of higher quality than the CVD grown graphene.

4.4 Fabry-Pérot interferences

When zooming in on the conductance of the exfoliated sample in the npn regime, an oscillatory pattern can be discerned. To enhance the contrast, we plot the deriva-

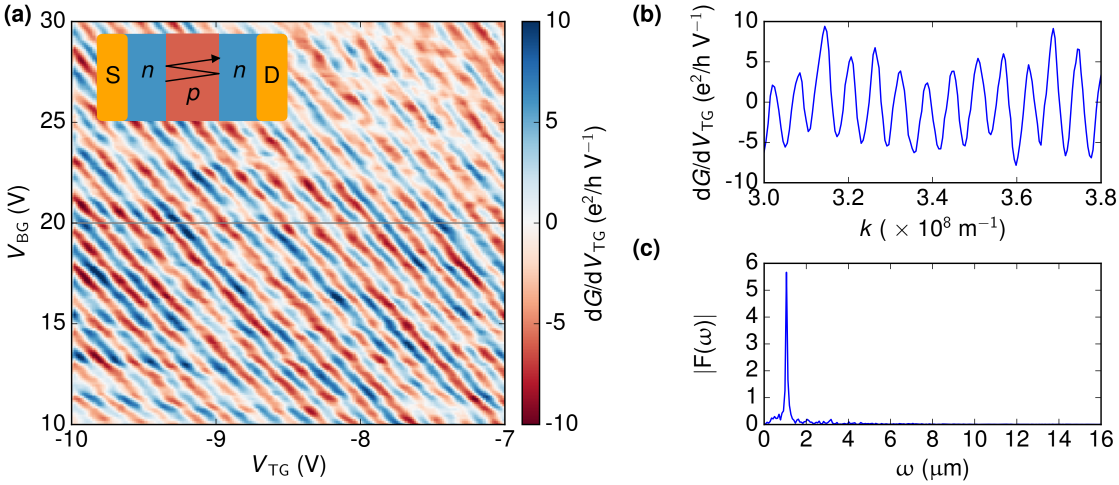

Figure 4.4: (a) Zoom of the transconductance as a function of top gate voltage and back gate voltage in the region marked by the white rectangle in Fig. 4.2b. The oscillatory pattern arises because the p-n interfaces form a Fabry-Pérot cavity (see inset). (b) Cut along the gray line in (a), where the gate voltage axis has been transformed into a wave vector axis. (c) Fourier transform of (b), exhibiting a sharp peak at $\omega = 1.1$ μm, which is twice the cavity length.

tive of the conductance with respect to top gate voltage (the transconductance) in Fig. 4.4. The gate voltage ranges are marked by the white rectangle in Fig. 4.2. The oscillatory pattern of the conductance in the bipolar regime has been observed before in both single layer graphene [75, 76] and bilayer graphene [6]. The two semi-transparent p-n interfaces create a cavity in which charge carriers bounce back and forth (see inset of Fig. 4.4a). The waves leaving the cavity after one or more passes through the cavity interfere with each other. For each additional round through the cavity, a phase of $\Delta\Phi = 2kL_{\mathrm{c}}$ is acquired, where L_{c} is the cavity length. Depending on the wave vector (which is changed by the gate voltage), this interference can be either constructive or destructive. This explains the oscillating conductance observed in the measurement. We plot the observed oscillations as a function of the wave vector $k = \sqrt{\pi n}$ (Fig. 4.4b) and take a Fourier transform (Fig. 4.4c) to extract the cavity length of $L_{\mathrm{c}} = \omega/2 = 0.55$ μm, which is in good agreement with the lithographic length of the top gate of $L_{\mathrm{TG}} = 0.5$ μm.

In the CVD graphene sample, no oscillations are observed. This can be explained by comparing the mean free path to the cavity length. For the exfoliated sample the mean free path is on the order of $\ell \approx 400$ nm, which is on the same order of magnitude as the cavity length. The transport through the cavity is therefore quasiballistic. The CVD graphene sample has a mean free path on the order of $\ell \approx 20$ nm, which is an order of magnitude smaller than the cavity length. The cavity is therefore in the diffusive regime and does not show any Fabry-Pérot oscillations.

4.5 Magnetotransport measurements

At sufficiently high perpendicular magnetic fields and sufficiently low temperature the quantum Hall effect occurs in two dimensional systems, which leads to a discrete energy spectrum [14]. In bilayer layer graphene the energy of the Landau levels is given by [77]:

$$E_N = \mathrm{sgn}(N)\hbar\omega_c\sqrt{N(N-1)} \qquad \text{for } N \in \mathbb{Z} \tag{4.1}$$

where $\omega_c = eB/m^*$. The energy separation of the levels therefore increases with magnetic field. For a more disordered sample a higher magnetic field is needed to observe the quantum Hall effect, because the Landau levels are broadened by disorder. Each Landau level can be occupied by at most eB/h charge carriers and therefore the filling factor, the total number of occupied Landau levels is given by $\nu = hn/eB$. In pristine bilayer graphene the spin and valley degrees of freedom [77, 78] lead to fourfold degenarate Landau levels in the regime where Zeeman splitting and spin-orbit interactions can be neglected [79]. An exception is the lowest Landau level, which is eightfold degenerate because $E_0 = E_1$. This results in quantization of the Hall conductivity σ_{xy} whenever the filling factor is close to an integer multiple of four:

$$\sigma_{xy} = \frac{e^2}{h}|\nu| \qquad \text{for } \nu \approx 4i,\ i \in \mathbb{Z}_{\neq 0} \tag{4.2}$$

and at the same time the longitudinal conductivity σ_{xx} drops to zero. For a square sample the quantized conductance, which occurs when the Fermi level lies in a gap between Landau levels, is therefore given by:

$$G = \sqrt{\sigma_{xx}^2 + \sigma_{xy}^2} = \sigma_{xy} = \frac{e^2}{h}|\nu| \qquad \text{for } \nu \approx 4i,\ i \in \mathbb{Z}_{\neq 0} \tag{4.3}$$

For a sample with a different length-to-width ratio, undershoots and overshoots around the plateau values occur [80].

Figure 4.5a shows the conductance of the CVD graphene sample as a function of back gate voltage and magnetic field for $V_{\mathrm{TG}} = -0.65$ V. This top gate voltage corresponds to a uniform density throughout the device. Around $B = 6$ T the conductance curve shows two plateau-like features on the electron side. The first plateau occurs close to the expected value of $G = 4\ e^2/h$. The second plateau does not appear at $G = 8\ e^2/h$ but at $G = 10\ e^2/h$ instead. With only two plateaus it is impossible to determine the contact resistance, which needs to be subtracted from the measured resistance, therefore we did not subtract any contact resistance from the curves in Fig. 4.5a and this might explain the deviations of the plateau from the expected value. Another explanation is the significant disorder in the sample, which leads to the onset of the quantum Hall effect only occurring around $B = 5 - 6$ T.

The conductance of the exfoliated graphene device as a function of back gate voltage and magnetic field at $V_{\mathrm{TG}} = 0$ V is shown in Fig. 4.5b. On the electron-side clear plateaus can be observed at $G = 4, 8, 12, 16\ e^2/h$. Figures 4.5c,d show the derivative of the conductance with respect to the x-axis as a function of back gate

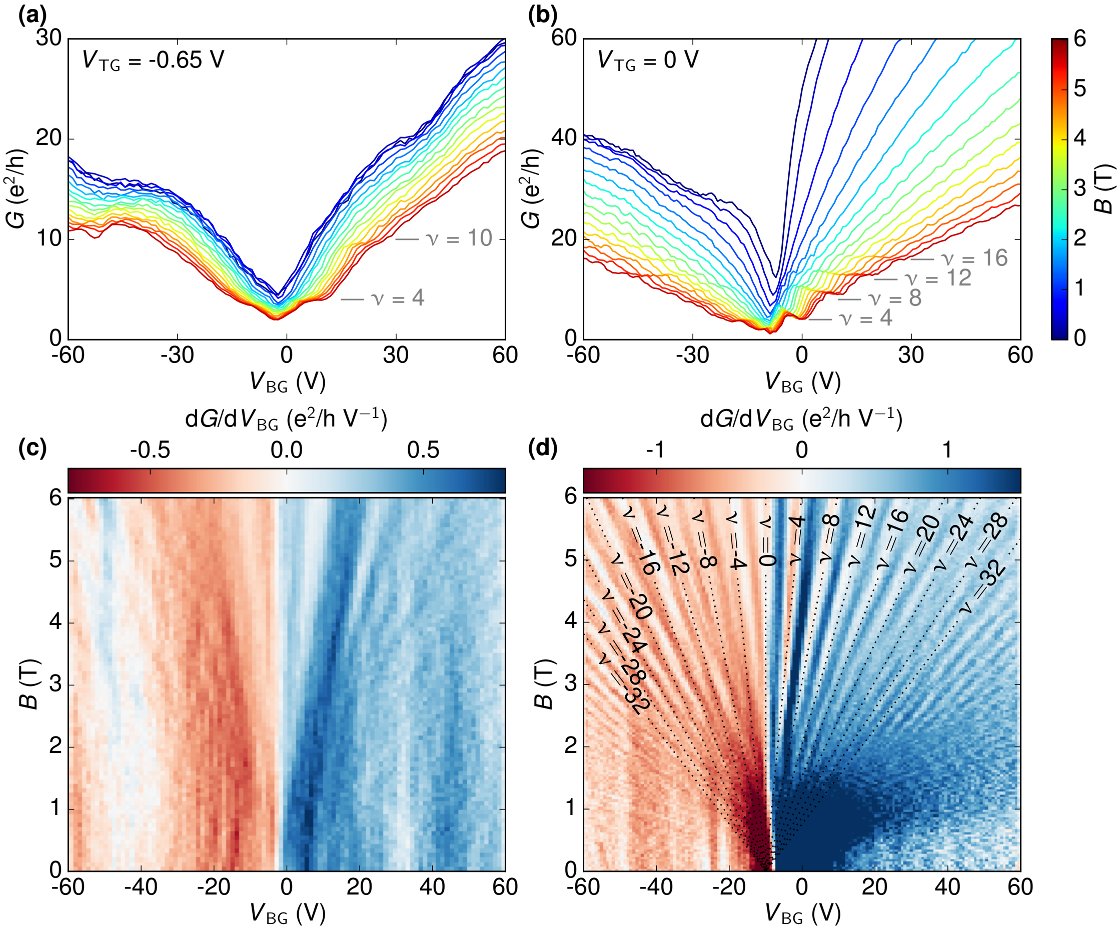

Figure 4.5: (a) Conductance of the CVD sample as a function of back gate and magnetic field for $V_{\mathrm{TG}} = -0.65$ V. (b) Conductance of the exfoliated graphene sample as a function of back gate and magnetic field for $V_{\mathrm{TG}} = 0$ V. (c) Derivative with respect to back gate voltage of the data in (a) (d) Derivative of the data in (b). The Landau levels are marked by their respective filling factors.

voltage and magnetic field. For the exfoliated sample the quantum Hall plateaus are clearly visible and they are marked by their respective filling factors. It shows a plateau at $\nu = 0$, contrary to what is expected for pristine bilayer graphene (see equation 4.3). This can be explained by the small but finite electric field in the sample [81]. The higher disorder in the CVD grown sample explains why the fan-like structure is weaker for this sample.

4.6 Magnetotransport in presence of electric fields

The degeneracy of bilayer graphene Landau levels gets lifted when the disorder broadening is smaller than the Zeeman splitting. Additionally, the valley degeneracy

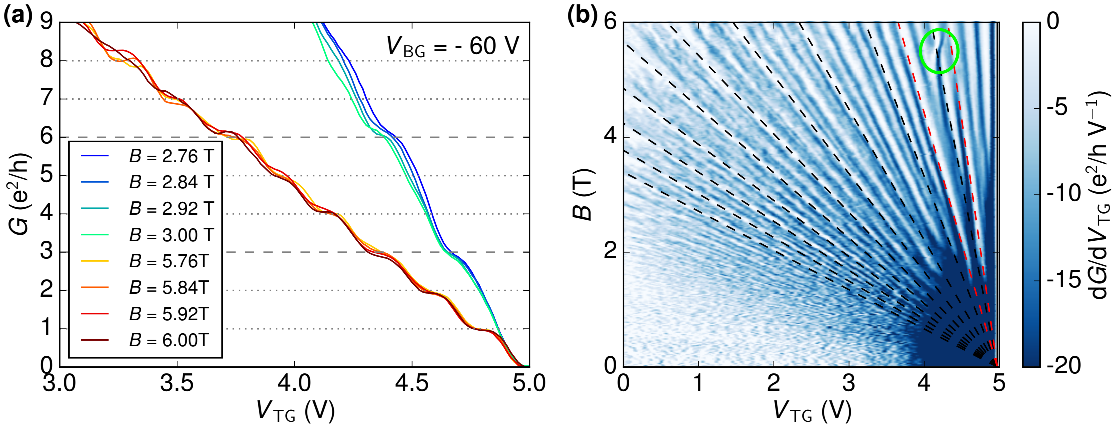

Figure 4.6: (a) Conductance of the exfoliated graphene sample as a function of top gate voltage for several magnetic field strengths at $V_{\mathrm{BG}} = -60$ V. Around $B = 3$ T a threefold degeneracy of the Landau levels is observed. Around $B = 6$ T all degeneracies are lifted. (b) Transconductance as a function of top gate voltage and magnetic field at $V_{\mathrm{BG}} = -60$ V. Landau levels for which the filling factor is a multiple of four are marked by black dashed lines. The plateaus related to $\nu = 3, 6$ are marked by red lines and show up prominently already at $B = 2$ T. Other integer filing factors are clearly visible as well. The green circle marks a level crossing.

can be lifted by the application of an electric field [82]. Quantum Hall plateaus at integer filling factors which are not a multiple of four have been observed in Refs. [7, 83–85]. Figure 4.6a shows the conductance of the exfoliated sample as a function of top gate voltage for several magnetic field strengths. The back gate was set to $V_{\mathrm{BG}} = 60$ V. For the top gate range of $V_{\mathrm{TG}} = 3 - 5$ V used in this measurement, the sample is in the $nn'n$ regime (see Fig. 4.2b). Since the charge carrier density in the outer regions is higher than the charge carrier density in the inner region, the filling factor of the inner region determines the conductance. Around $B = 6$ T plateaus can be observed for $G = 1, 2, 3, ...8$ e^2/h, as expected in presence of an electric field. Around $B = 3$ T the conductance shows a more unconventional sequence of conductance plateaus at $G = 3, 6$ e^2/h. This is a consequence of the Lifshitz transition which occurs in the $B = 0$ T band structure. When taking skew interlayer hopping into account, the Fermi contour at low density is not circular, but consists of three equivalent pockets. The anomolous quantum Hall sequence arising from the Lifshitz transition has been studied in detail in Refs. [7, 37]. In Fig. 4.6b the transconductance as a function of top gate voltage and magnetic field is shown. Quantum Hall plateaus show up as white lines. The plateaus corresponding to $\nu = 4i$ with $i \in \mathbb{Z}$ are marked by a black dashed line. The broken degeneracy is apparent from the presence of other plateaus between the marked ones. The prominent $G = 3, 6$ e^2/h plateaus are marked by red dashed lines. A level crossing resulting from the Lifshitz transition is indicated by a green circle.

4.7 Conclusion

In this chapter we have compared the quality of samples made with CVD grown bilayer graphene and exfoliated bilayer graphene. The high disorder density and the low mobility, the absence of Fabry-Pérot interferences and the onset of the quantum Hall effect at high magnetic fields for the CVD sample indicate that this sample is significantly more disordered. The CVD grown graphene was inspected in a scanning electron microscope after growth, which may have resulted in the deposition of additional carbon atoms on the surface. We intended to make samples with a second batch of CVD graphene, which has not been inspected with electron beams after growth. For the second batch we did not succeed in removing the graphene from the CuNi foil. This could be related to a possibly higher surface coverage of the graphene, which makes the oxidation process of the foil less efficient. In the mean time Schmitz et al. [86] have reported on the fabrication and characterization of a CVD grown bilayer graphene sample with a mobility at $T = 2$ K of $\mu = 1.8 \times 10^5$ cm^2/(Vs) for electrons and $\mu = 0.8 \times 10^5$ cm^2/(Vs) for holes. The CVD graphene they measure can therefore compete with state of the art exfoliated graphene samples.

Chapter 5

Oscillatory magnetoresistance in p-n junctions

This chapter is based on the work:

Oscillating magnetoresistance in graphene p-n junctions at intermediate magnetic fields
Hiske Overweg, Hannah Eggimann, Ming-Hao Liu, Anastasia Varlet, Marius Eich, Pauline Simonet, Yongjin Lee, Kenji Watanabe, Takashi Taniguchi, Klaus Richter, Vladimir I. Fal'ko, Klaus Ensslin, Thomas Ihn
Nano Letters **17**, 2852–2857 (2017)

5.1 Introduction

In this chapter we report on the observation of magnetoresistance oscillations in graphene p-n junctions. The oscillations have been observed for six samples, consisting of single-layer and bilayer graphene, and persist up to temperatures of 30 K, where standard Shubnikov-de Haas oscillations are no longer discernible. The oscillatory magnetoresistance can be reproduced by tight-binding simulations. We attribute this phenomenon to the modulated densities of states in the n- and p-regions.

p-n junctions are among the basic building blocks of any electronic circuit. The ambipolar nature of graphene provides a flexible way to induce p-n junctions by electrostatic gating. This offers the opportunity to tune the charge carrier densities in the n- and p-doped regions independently. The potential gradient across a p-n interface depends on the thickness of the involved insulators and can also be modified by appropriate gate voltages. Due to the high electronic quality of present day graphene devices a number of transport phenomena in *pnp* or *npn* junctions have been reported, such as ballistic Fabry-Pérot oscillations [6, 75, 76] and so-called snake states [87, 88], both of which depend on characteristic length scales of the sample.

Here we report on the discovery of yet another kind of oscillation, which does not depend on any such length scale. The oscillations occur in the bipolar regime, in the magnetic field range where Shubnikov-de Haas oscillations are observed in the unipolar regime. These novel oscillations in the bipolar regime are governed by the unique condition that the distance between two resistance minima (or maxima) in gate voltage space is given by a constant filling factor difference of $\Delta\nu = 8$. The features are remarkably robust: they occur in samples with one and two *p*-*n* interfaces; in single and bilayer graphene; up to temperatures of 30 K (where Shubnikov-de Haas oscillations have long disappeared); over a large density range; for interface lengths ranging from 1 μm to 3 μm and in both *pnp* and *npn* regimes. The oscillations have been observed in a magnetic field range of $B = 0.4$ T up to $B = 1.4$ T. Their periodicity does not match the periodicity of the aforementioned snake states. Here we address this phenomenon and suggest a model which can qualitatively explain the oscillations.

5.2 Samples

Measurements were performed on six samples in total, which all consist of a graphene flake encapsulated between two hexagonal boron nitride (h-BN) flakes on a Si/SiO$_2$ substrate. They all show similar behavior. This paper focuses on measurements performed on one sample (sample A), with the device geometry sketched in Fig. 5.1a. Specifications of the other five samples are summarized in table 5.1. The bilayer graphene (BLG) flake was encapsulated with the dry transfer technique described in Ref. [26]. A top gate was evaporated on the middle part of the sample, which divides the device into two outer regions, only gated by the back gate (single-gated regions), and the dual-gated middle region. The other five samples were made with the more recent van der Waals pick-up technique [27]. Unless stated otherwise, the measurements were performed at 1.7 K. An AC voltage bias of 50 μV was applied symmetrically between the Ohmic contacts ('source' and 'drain' in Fig. 5.1a, inner contacts in Fig. 5.1b) and the current between the same contacts was measured. The

sample name	**A**	**B**	**C**	**D**	**E**	**F**
sample width W (μm)	1.3	1.4	1.1	0.9	3	1.2
sample length L (μm)	3.0	1.4	1.0	2.3	3	2.8
top gate length L_{TG} (μm)	1.1	0.7	0.55	1.2	1.0	1.0
distance to top gate (nm)	23	44	28	57	35	25
number of graphene layers	2	1	2	2	2	2
junction type	*npn*	*pn*	*npn*	*pn*	*npn*	*npn*

Table 5.1: Characteristics of samples A-F

transconductance dG/dV_{TG} was measured by applying an AC modulation voltage of 20 mV to the top gate.

5.3 Measurements

Figure 5.1c shows the conductance as a function of top gate voltage V_{TG} and back gate voltage V_{BG}. Charge neutrality of the single-gated regions shows up as a horizontal line of low conductance and is marked by a white line. The diagonal line of low conductance corresponds to charge neutrality of the dual-gated region. The slope of this line is given by the capacitance ratio of the top and back gate. Together these lines divide the map into four regions with different combinations of carrier types: two with the same polarities in the single- and dual-gated regions (*pp'p* and *nn'n*) and two with different polarities (*npn* and *pnp*). The conductance in the latter regions shows a modulation which is more clearly visible in the transconductance (see Fig. 5.2a). The oscillatory conductance is caused by Fabry-Pérot interference of charge carriers travelling back and forth in the region of the sample underneath the top gate. Their periodicity yields a cavity length $L_{\mathrm{TG}} = 1.1$ μm, which is in agreement with the lithographic length of the top gate. The Fabry-Pérot oscillations were studied in more detail in Ref. [6], which revealed the ballistic nature of transport in the dual-gated region.

The Fabry-Pérot oscillations disappear in a magnetic field of $B \gtrsim 100$ mT (see Fig. 5.2b-d). Yet at magnetic fields of $B = 0.4$ T a new oscillatory pattern appears in the *npn* and *pnp* regime. This can be seen in the conductance and transconductance maps recorded at $B = 0.5$ T, shown in Figs. 5.3a-d. The oscillations follow neither the horizontal slope of features taking place in the single-gated region, nor the diagonal slope of the dual-gated region. They are therefore expected to occur at the interface between the *p*- and *n*-doped regions. This was confirmed by measurements on sample D, which had two contacts in the single-gated region and two contacts in the dual-gated region. For this sample, only the conductance along paths involving the interface shows oscillations (see Appendix D).

On top of this novel oscillatory pattern the transconductance of sample A in Fig. 5.3b(d) shows faint diagonal lines in the *nn'n*(*pp'p*) regime, which are Shubnikov-de Haas oscillations in the dual-gated region. The occurrence of Shubnikov-de Haas oscillations shows that in this moderate magnetic field regime the Landau levels are broadened by disorder on the scale of their spacing, resulting in a modulation of the density of states.

Using a plate capacitor model described in section 2.2, the gate voltage axes can be converted into density and filling factor axes, ν_X with $X = \mathrm{SG}, \mathrm{DG}$ for the single- and dual-gated regions, respectively. The result of this transformation is shown in Fig. 5.3e. The oscillatory pattern has a slope of one, i.e. it follows lines of constant filling factor difference $\Delta\nu = \nu_{\mathrm{DG}} - \nu_{\mathrm{SG}}$. It appears that the oscillations can be

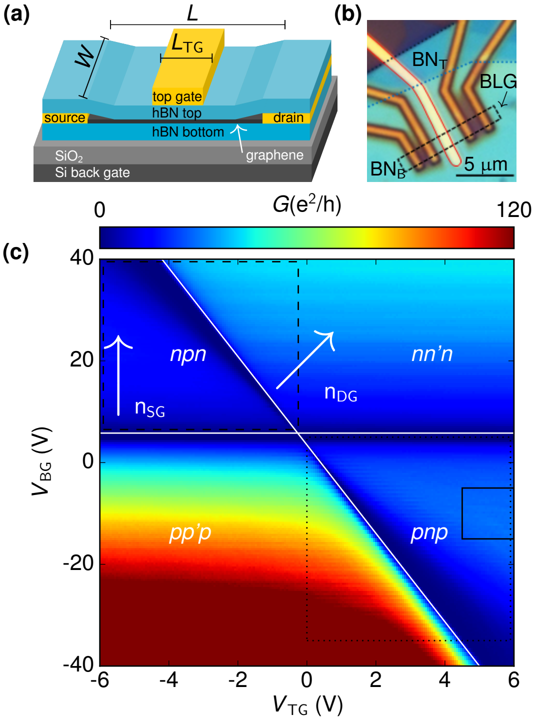

Figure 5.1: Characterization of the device. (a) Schematic of the device: a bilayer graphene flake is encapsulated between h-BN layers. It is contacted by Au contacts and a Au top gate is patterned on top, which defines the dual-gated region. (b) Optical microscope image of the sample. The four contacts, of which only the inner ones were used, appear orange. The top gate is outlined by a red curve. (c) Conductance of the sample at $B = 0$ T, $T = 1.7$ K. Four regions of different polarities are indicated. A zoom of the transconductance in the boxed region with a solid line is shown in Fig. 5.2. The dashed (dotted) box indicates the gate voltage range in which Figs. 5.3a,b (c,d) were measured.

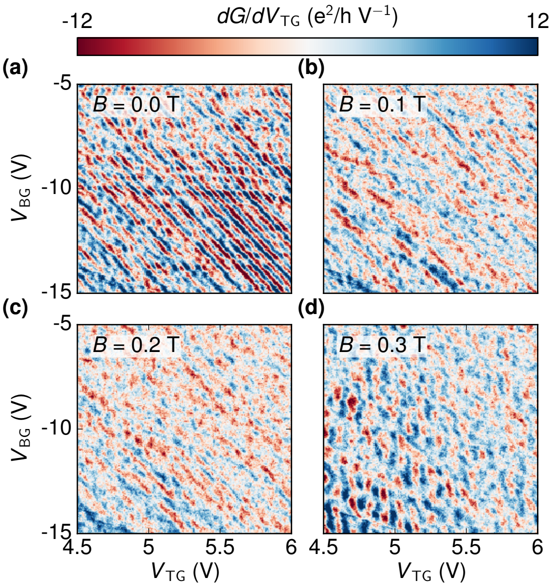

Figure 5.2: Disappearance of Fabry-Pérot oscillations with increasing magnetic field. The measurement was taken in the boxed region with solid lines in Fig. 5.1c. At $B = 0$ T (a) the transconductance shows clear Fabry-Pérot oscillations. They disappear in a magnetic field of $B \gtrsim 0.1$ T (b–d).

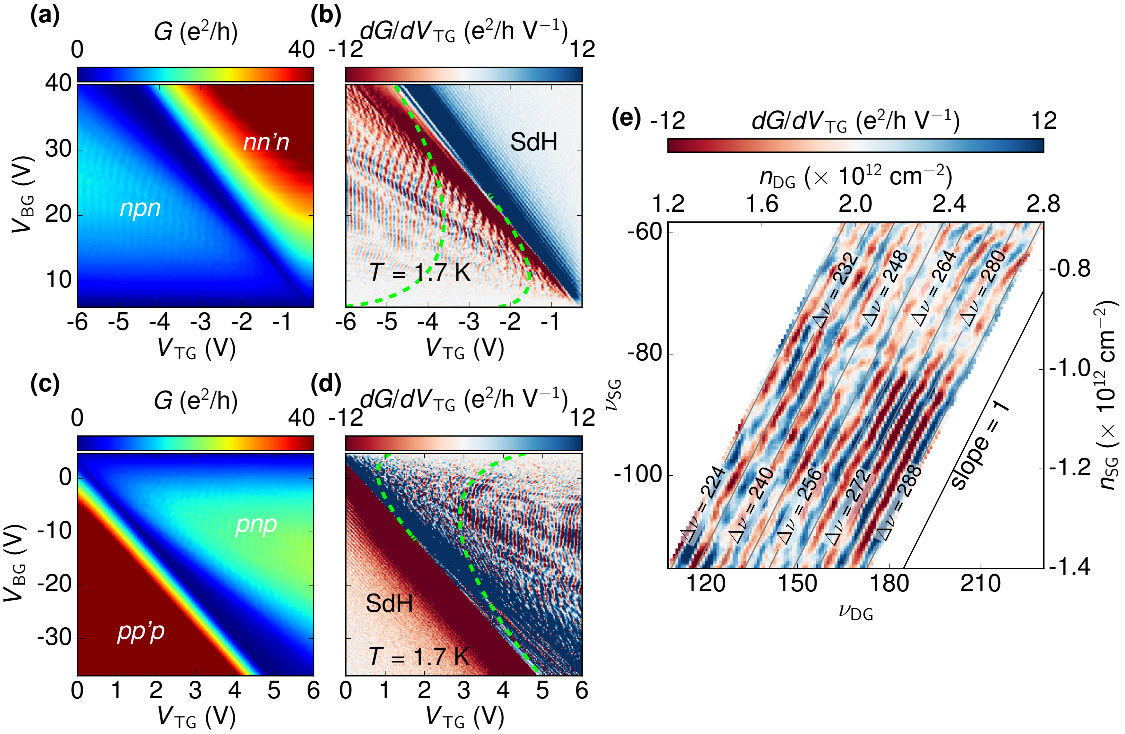

Figure 5.3: Magnetotransport at $B = 0.5$ T. (a) Conductance of the sample at 0.5 T, showing an oscillatory pattern in the *npn* regime. The measurement was taken in the dashed boxed region of Fig. 5.1c. (b) The oscillatory pattern in the *npn* regime is more clearly visible in the transconductance. Green dashed lines indicate the pattern expected for snake states. In the *nn'n* regime some faint lines can be distinguished, following the slope of the charge neutrality line of the dual gated region. These are Shubnikov-de Haas oscillations. (c),(d) Same as (a),(b), but with opposite charge carrier polarities. The oscillations are essentially particle-hole symmetric. (e) Transconductance at $B = 0.5$ T in the *pnp* regime as a function of charge carrier density (and filling factor) in the single- and dual-gated region. The oscillatory pattern follows the indicated line of slope one and can therefore be described by lines of constant filling factor difference $\Delta\nu = \nu_{\mathrm{DG}} - \nu_{\mathrm{SG}}$.

phenomenologically described by:

$$G = \langle G \rangle + A \ \cos\left(2\pi \frac{\Delta\nu}{8}\right) \tag{5.1}$$

where A is the amplitude of the oscillations, which is on the order of 4 % of the background conductance $\langle G \rangle$ at $T = 1.7$ K. The distance between one conductance maximum and the next can therefore be bridged by either changing the filling factor in one region by 8, or by changing the filling factor in both regions oppositely by 4. It should be noted that Eq. (5.1) can be used to describe the oscillations in all

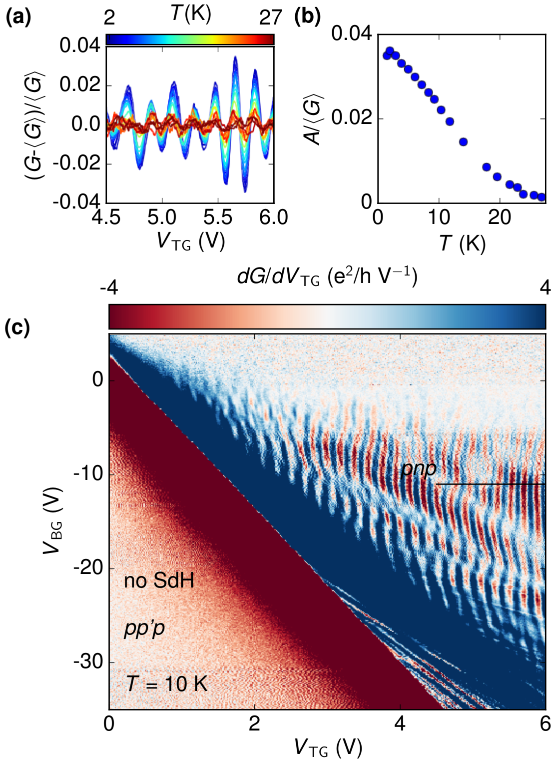

Figure 5.4: Temperature dependence. (a) Oscillatory part of the conductance as a function of top gate voltage and temperature measured along the line cut indicated by the black line in Fig. 5.4c. (b) Amplitude A of the oscillatory conductance as a function of temperature. The oscillations disappear around $T = 30$ K. (c) Transconductance at $T = 10$ K, $B = 0.5$ T in the *pnp* regime. Whereas Shubnikov-de Haas oscillations in the *pp'p* regime have faded out, the oscillatory pattern in the *pnp* regime persists.

six samples, regardless of the number of graphene layers and the sample width (see table 5.1 and Appendix D).

The oscillations persist in magnetic fields up to $B = 1$ T for sample A and the periodicity scales with $\Delta\nu$ for the entire magnetic field range. In higher magnetic fields the conductance is dominated by quantum Hall edge channels and takes on values below e^2/h in the *npn* and *pnp* regimes, in agreement with observations by Amet et al. [89]. Other works report on the (partial) equilibration of edge channels [89–94] and shot noise [95, 96] in p-n junctions in the quantum Hall regime.

The oscillatory conductance is quite robust against temperature changes. Figure 5.4a,b show the decay of the amplitude as a function of temperature T. The oscillatory conductance in the *pnp* and *npn* regime disappear at a temperature around $T = 30$ K. As can be seen in Fig. 5.4c, at $T = 10$ K the oscillations are still clearly present, while the Shubnikov-de Haas oscillations in the *pp'p* regime have already faded out. The persistence up to $T = 30$ K indicates that the studied phenomenon does not require phase coherence on the scale of the device size. The phase coherence length at $T = 1.7$ K is estimated to be on the order of the device size, but it falls off with $1/T$ [97].

5.4 Tight binding model

The above discussed oscillations can be reproduced by transport calculations carried out by Ming-Hao Liu for an ideal SLG p-n junction at an intermediate magnetic field B, based on the scalable tight-binding model [98]. The ideal junction is modeled by connecting two semi-infinite graphene ribbons (oriented along armchair) with their carrier densities given by n_L in the far left and n_R in the far right. A simple hyperbolic tangent function with smoothness 50 nm bridging n_L and n_R is considered; see the inset of Fig. 5.5a for an example. To cover the density range up to $\pm 3 \times 10^{12}$ cm^{-2} corresponding to a maximal Fermi energy of $E_{\max} \approx 0.2$ eV, the scaling factor $s_f = 10$ is chosen because it fulfills the scaling criterion [98] $s_f \ll 3\gamma_0\pi/E_{\max} \approx 141$ very well; here $\gamma_0 \approx 3$ eV is the hopping energy of the unscaled graphene lattice. Note that the following simulations consider $W = 1$ μm for the width of the graphene ribbon, but simulations based on a different width show an identical oscillation behavior (see Appendix B for details), confirming its width-independent nature as already concluded from our measurements.

The transmission function $T(n_R, n_L)$ across the ideal p-n junction at $B = 0.5$ T is shown in Fig. 5.5a, where fine oscillations along symmetric bipolar axis (marked by the blue arrows) from np to pn through the global charge neutrality point can be seen. Two regions marked by the white dashed boxes in Fig. 5.5a are zoomed-in and shown in Figs. 5.5b and d for a closer look and comparison with the measurements of sample B and E (Figs. 5.5c and e, respectively). Despite certain phase shifts (observed in Figs. 5.5b, d, and e) that are beyond the scope of the present study, good agreement between our transport simulation and experiment showing the oscillation period well fulfilling Eq. (5.1) can be seen.

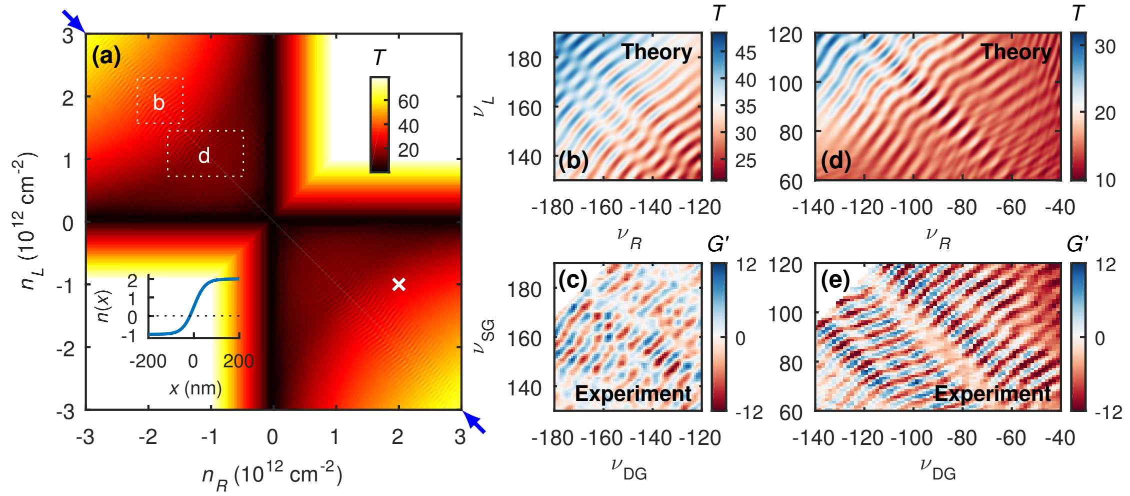

Figure 5.5: (a) Transmission T as a function of the carrier densities on the left, n_L, and right, n_R, for an ideal SLG p-n junction at a perpendicular magnetic field $B = 0.5$ T based on a tight-binding transport calculation (color range restricted for clarity). Oscillations occur in the vicinity of the symmetric bipolar axis marked by blue arrows. Inset: an example of the considered carrier density profile corresponding to the white cross. White dashed boxes correspond to the density regions shown in panels (b) and (d), where the carrier density values are transformed in filling factors. (c)/(e) Transconductance G' measured for sample B/E shown with the same filling factor range as (b)/(d).

5.5 Physical model

Other works [87, 88] report on the formation of so called snake states along p-n interfaces in graphene. Snake states result in a minimum in the conductance whenever the sample width W and the cyclotron radius R_c satisfy $W/R_c = 4m - 1$ with m a positive integer. In the density range of Fig. 5.3b,d this would lead to two resonances at most (indicated by green dashed lines in Fig. 5.3b,d), which is far less than the observed number of resonances. On top of that, snake states are inconsistent with the observed absence of a dependence on sample width. Furthermore, the tight-binding simulation also confirms that the observed effect is independent of the sample width and cannot be suppressed by introducing strong lattice defects in the vicinity of the p-n junction (see Appendix B). We therefore rule out snaking trajectories as a possible cause of the observed oscillations.

Another process which could give rise to oscillations in a graphene p-n junction in a magnetic field is the interference of charge carriers which are partly reflected and partly transmitted at the interface. When the charge carrier densities are equal on both sides of the interface, electrons and holes will have equal cyclotron radii and therefore the paths of transmitted and reflected charge carriers will form closed loops. For the case of equal density, this model predicts the right periodicity of the oscillations [99]. Experimentally, however, the measured oscillations are still visible when the densities on both sides of the p-n interface are quite different: at the point $(V_{\mathrm{BG}},V_{\mathrm{TG}}) = (12,\text{-}6)$ V for example (see Fig. 5.3b), the cyclotron radii on the p and n side are respectively 0.36 μm and 0.16 μm. The path lengths hence differ by $2\Delta R_{\mathrm{c}} = 0.40$ μm, which is more than seven times the Fermi wavelength (0.02 μm and 0.05 μm). It seems unlikely that interference between charge carriers on skipping orbits can still occur in this density regime. One could consider a refinement of this model by taking into account trajectories with a non-normal incidence on the p-n interface. It can be shown however that it is impossible to form such a trajectory when the densities are not equal. Consider the situation sketched in Fig. 5.6. Basic geometry tells us that:

$$L = 2R_{\mathrm{c},1}\cos(\vartheta_1) = 2R_{\mathrm{c},2}\cos(\vartheta_2) \tag{5.2}$$

and therefore

$$\sqrt{n_1}\cos(\vartheta_1) = \sqrt{n_2}\cos(\vartheta_2) \tag{5.3}$$

where n_1 and n_2 are the charge carrier densities on the two sides of the interface. Considering conservation of the transverse component of the momentum leads to Snell's law:

$$k_{\mathrm{F},1}\sin(\vartheta_1) = k_{\mathrm{F},2}\sin(\vartheta_2) \tag{5.4}$$

which implies

$$\sqrt{n_1}\sin(\vartheta_1) = \sqrt{n_2}\sin(\vartheta_2) \tag{5.5}$$

Combining Eqs. 5.3 and 5.5 leads to the conclusion that $\vartheta_1 = \vartheta_2$ and therefore $n_1 = n_2$. This picture could be altered when taking the density gradient along the p-n junction into account, though.

The tight-binding simulations show that the oscillatory pattern is still present when introducing large-area lattice defects in the vicinity of the p-n junction, which destroy the skipping trajectories (see Appendix B). The observed robustness against temperature changes is in contradiction with this model as well. Thus, the observed oscillations cannot be ascribed to interference of charge carriers on cyclotron orbits at the p-n interface.

Since the oscillations occur in both single-layer and bilayer graphene, we exclude an explanation that relies on specific details of the dispersion relation. In the magnetic field range where the oscillations are observed, the sample width is comparable to the classical cyclotron diameter. This excludes explanations based on classical electron flow following skipping orbit-like motion along edges.

A mechanism which may cause the oscillations involves the alignment of the density of states (DOS) around the Fermi energy. Diagrams of the DOS in the single- and dual-gated regions are sketched in Figs. 5.7a-c. Figure 5.7d shows a zoom in the map of the oscillatory transconductance of Fig. 5.3e. At point a in this zoom the filling factor in the dual-gated regime is $\nu_{\mathrm{DG}} = 180$ and $\nu_{\mathrm{SG}} = \text{-}92$ in the single-gated region. Because of the fourfold degeneracy of the Landau levels,

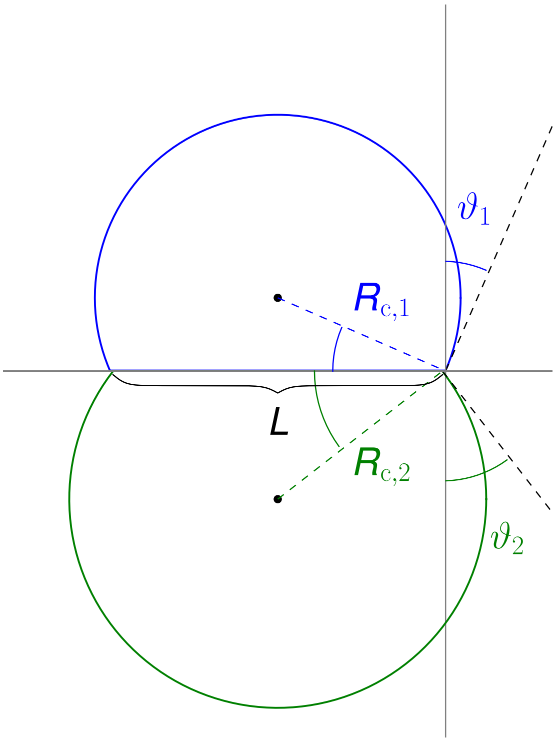

Figure 5.6: Interference of two trajectories along a *p*-*n* interface. Because of Snell's law, the sketched situation, with different charge carrier densities on both sides of the interface, cannot be realized.

Landau level numbers are N = 45 and N = -23 respectively, as shown in the DOS diagram of Fig. 5.7a. When following the oscillatory pattern from point a to point b, the two combs of DOS remain aligned with one another and only the Fermi level changes. This is in contrast to what happens when moving from point a to point c: the DOSs shift with respect to one another and the transconductance oscillates. It could therefore be the case that the alignment of the DOS affects the conductance of the *p*-*n* interface in a way similar to the magneto-intersubband oscillations (MISO) of a two-dimensional electron gas (2DEG) [100, 101]: the occupation of two energy subbands of a 2DEG can lead to enhanced scattering between the subbands when the DOSs of the subbands are aligned. Although the *p*- and *n*- regions are spatially separated in the case of graphene *p*-*n* junctions, a similar enhancement of the coupling at the interface may be observed. Numerical calculations of the overlap of the density of states can be found in Appendix C.

In the *pp'p* and *nn'n* regime the interfaces are much more transparent (see conductance in Fig. 5.4a,d and Ref. [102]), therefore the interface plays a negligible role in the total conductance. This explains why the oscillations are only visible in presence of a *p*-*n* interface.

As the two outer regions of the sample have the same density up to an insignificant difference in residual doping, the two *p*-*n* interfaces contribute in a similar way. The number of interfaces can at most influence the visibility of the oscillations. In practice we find that the visibility is however mostly influenced by sample quality.

Just as for the oscillations we report on, MISO persist up to relatively high

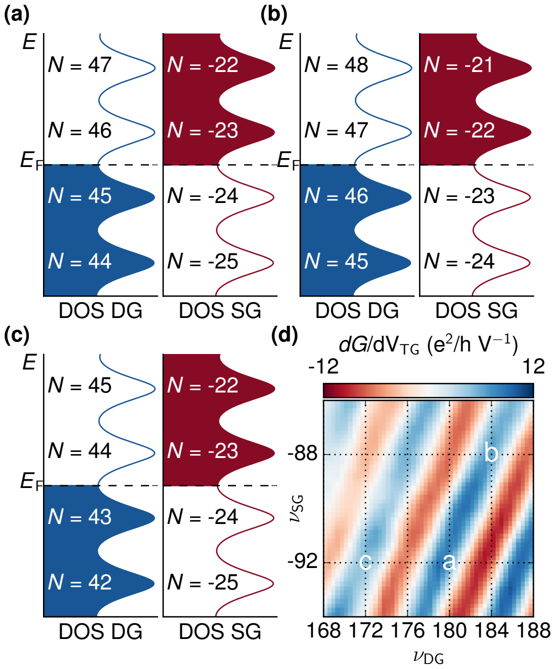

Figure 5.7: (a-c) Schematics of the densities of states as a function of energy for the single- and dual-gated regions of the sample at positions a-c of the measurement (d) Zoom in Fig. 5.3e. The alignment of the densities of states can lead to an oscillatory pattern with the right slope: along the line from point a to point b the two combs of densities of states stay aligned, whereas the combs shift with respect to one another when moving from point a to point c.

temperatures. The spacing predicted by this model lacks a factor of two compared to the experiment, however: it would predict the argument of the cosine of Eq. (5.1) to be $2\pi\Delta\nu/4$. Further investigation is needed to explain this discrepancy between the MISO model on the one hand and the experimental data and the tight-binding simulations on the other hand.

5.6 Conclusion

We have observed oscillations in the conductance of six graphene p-n junctions in the magnetic field range of $B = 0.4 - 1.5$ T. The oscillations are independent of sample width and can be described by the filling factor difference between the single- and dual-gated regions. The oscillations are quite robust against temperature changes: they fade out only in the range of $T = 20 - 40$ K, whereas Shubnikov-de Haas oscillations decay below $T = 10$ K. The oscillations can be well reproduced by tight-binding transport calculations considering an ideal p-n junction at a constant magnetic field. Up to a factor of two, the oscillatory pattern can be explained by considering the density of states alignment of the single- and dual-gated regions.

Chapter 6

Graphite back gates

Parts of this chapter are based on the work:

Electrostatically induced quantum point contacts in bilayer graphene
Hiske Overweg, Hannah Eggimann, Xi Chen, Sergey Slizovskiy, Marius Eich, Pauline Simonet, Riccardo Pisoni, Yongjin Lee, Kenji Watanabe, Takashi Taniguchi, Vladimir I. Fal'ko, Klaus Ensslin, Thomas Ihn
Nano Letters **18**, 553-559 (2018)

6.1 Introduction

In this chapter we investigate the band gap in bilayer graphene induced by an electric field. The samples have the same gate geometry as shown in the previous chapters (Figs. 4.1a, 5.1a). The first eight samples we studied, consisted of bilayer graphene encapsulated in hBN with a highly n-doped Si back gate and a Au top gate.

We found similar results to what was often found in literature (see Chapter 2): the resistivity at low temperatures with increasing electric field stayed below the $M\Omega$ regime, impeding the electrostatic definition of nanostructures. The resistivity as a function of electric field at $T = 2$ K for five of these samples is plotted with black symbols in Fig. 6.1a, along with the results from literature mentioned in chapter 2. The mobility of our samples, plotted in Fig. 6.1b, is on par with state of the art encapsulated bilayer graphene devices. The other three samples were not included in this figure as they were measured at $T = 4.2$ K only. Inspired by the works of Hunt et al. [55] and Chen et al. [103], who employed a graphite back gate for a monolayer graphene device, and Li et al. [50], who achieved high resistivity in a bilayer graphene sample with a graphite back gate (see Fig. 6.1a), we decided to

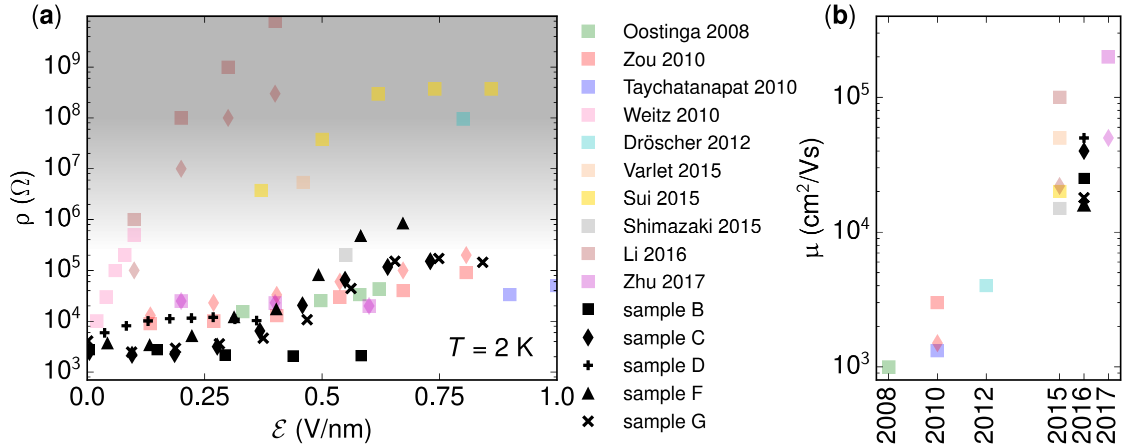

Figure 6.1: (a) Resistivity as a function of electric field at $T = 2$ K. Different symbols denote different samples. (b) Mobility as a function of year of publication or measurement.

study samples with a graphite back gate as well[1]. The sample geometry is discussed in section 6.2. Section 6.3 discusses transport measurements in the samples with a graphite back gate at low temperature. The bias dependence, resulting in a first estimate of the gap size, is shown in section 6.4. The temperature dependence of the resistivity, which gives a more precise estimate of the gap, is discussed in section 6.5. Finally our findings are summarized in section 6.6.

6.2 Sample geometry

The samples studied in this chapter have the same barrier geometry as studied in chapters 4 and 5, except that the Si back gate is replaced by a graphite flake below the device. This geometry is sketched in Fig. 6.2. The graphite back gate is atomically flat. Because of its close vicinity to the graphene layer it potentially results in a better screening of charged impurities in the Si substrate, in the boron nitride and in the graphene itself. It also leads to a stray field pattern which is different from samples with a Si back gate[2]. This can affect the doping profile across the sample, which is an important factor to take into account when studying current flow along device edges [51, 54, 56].

---

[1] We thank Yongjin Lee for this excellent suggestion.

[2] We thank Kostya Novoselov for this suggestion

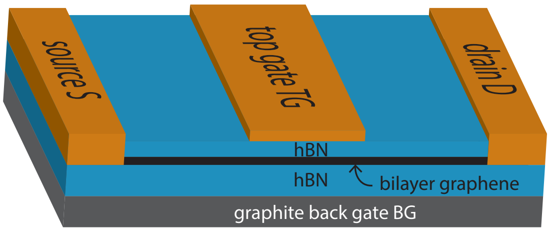

Figure 6.2: Schematic of an encapsulated bilayer graphene sample with a graphite back gate below the device. Source and drain contacts are used to probe transport through the graphene layer. The top gate covers the middle region of the device

6.3 Resistance map

The resistance as a function of top gate voltage and back gate voltage for samples E and H, both with a graphite back gate, is shown in Fig. 6.3. The resistance increases by orders of magnitude along the diagonal line along which the band gap opens. This is in sharp contrast with the samples without a graphite back gate, which only showed a moderate increase in resistance along this line (see Fig. 6.1a).

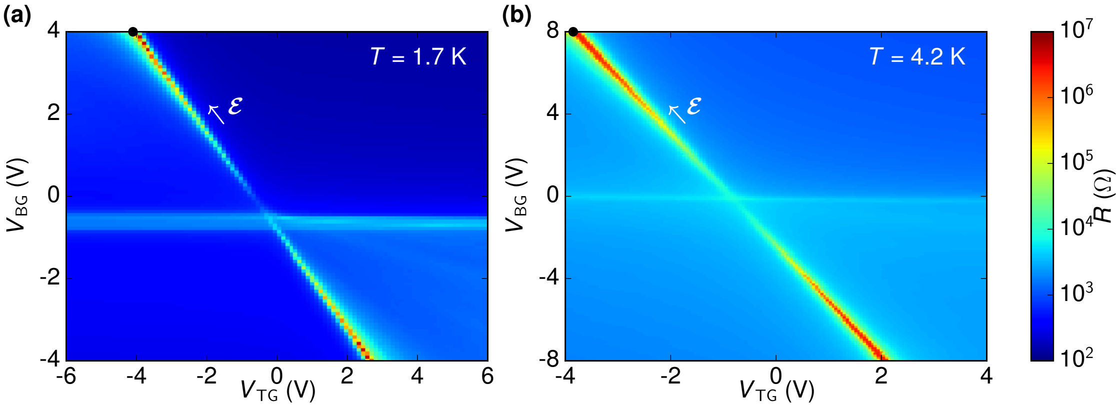

Figure 6.3: (a) Resistance of sample E as a function of top gate voltage and back gate voltage measured at $T = 1.7$ K. Along the diagonal line a band gap opens in the direction of the arrow which results in a significant increase of the sample resistance. (b) Resistance of sample H as a function of top gate voltage and back gate voltage measured at $T = 4.2$ K. Similar behavior is observed for this sample.

6.4 IV characteristics

The resistance of sample E reaches values which are too high to measure with a small AC bias voltage. We therefore measure the current as a function of the DC source drain voltage at the point of highest resistance, marked with the black dot in Fig. 6.3a. At this point the electric field is $\mathcal{E} = 0.37$ V/nm. The result is shown in Fig. 6.4. The strong reduction of the slope of the curve around $V_{\mathrm{SD}} = 0$ V is a clear indication of the induced band gap. The resistance in the gap can be read off from the slope close to $V_{\mathrm{SD}} = 0$ V (see inset) and is determined to be $R = 23$ GΩ. This resistance is on the order of the leakage resistance between wires in our set-up, which defines an upper limit of the resistance we can measure. The vertical offset at $V_{\mathrm{SD}} = 0$ V is artificial and is caused by the offset of the IV-converter.

From Fig. 6.4 the band gap of sample E can be estimated to be $E_{gap} \approx 40$ meV. This gap size is on the same order of magnitude as the gap size expected from tight binding calculations [41] in an electric field of $\mathcal{E} = 0.37$ V/nm, whereas in earlier works the extracted gap size was two orders of magnitude smaller than the theoretical gap size [45].

The maximal resistance measured in sample H was $R = 10$ MΩ, despite the fact that a higher electric field of $\mathcal{E} = 0.85$ V/nm was reached at the position of the black dot in Fig. 6.3b. A possible explanation for the lower resistance achieved in this sample is the fact that the region of the graphene under the top gate was not entirely free of bubbles (see section 3.6). The lower quality of the graphene in this region can lead to more mid-gap states. The maximal resistance in this sample nonetheless satisfies the criterion $R \gg R_{\mathrm{K}}$, so it is still within the range which is suitable for the definition of nanostructures [9].

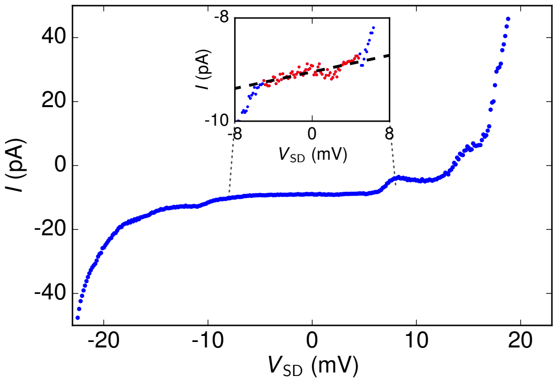

Figure 6.4: Current through sample E as a function of the source drain bias voltage measured in an electric field of $\mathcal{E} = 0.37$ V/nm. The linear slope fitted through the data points around $V_{\mathrm{SD}} = 0$ V (inset) yields a resistance of $R = 23$ GΩ

6.5 Temperature dependence

To get a more precise measurement of the band gap, we measure the resistivity at the point marked by the black dot in Fig. 6.3a as a function of temperature. The result is shown in Fig. 6.5. The white squares and the black line correspond to sample E and the colored data points correspond to other samples from literature. Down to $T = 40$ K the resistance follows the Arrhenius law $\rho \sim \exp(E_{gap}/(2k_BT))$. The extracted band gap is $E_{gap} = 55$ meV for an electric field of $\mathcal{E} = 0.37$ V/nm, which is in good agreement with the numerically determined gap size [25].

Just as reported before in literature, the resistivity deviates from the Arrhenius law at low temperatures, indicating that hopping via mid-gap states occurs in sample E as well.

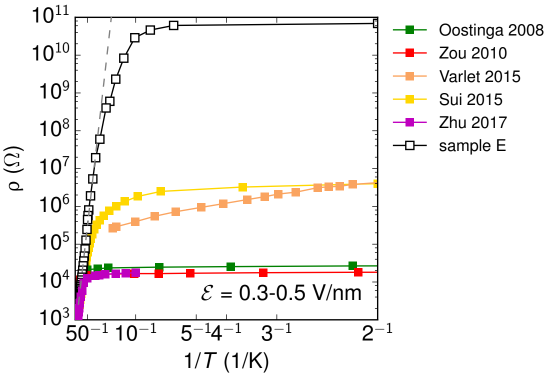

Figure 6.5: Resistivity as a function of temperature for sample E (white squares) and several samples from literature (colored squares) measured in an electric field of $\mathcal{E} = 0.3 - 0.5$ V/nm. The dashed line is a fit of the Arrhenius law, which gives a band gap of $E_{gap} = 55$ meV.

6.6 Conclusion

The effect of a graphite back gate on the resistivity of bilayer graphene samples at low temperatures as a function of electric field is summarized in Fig. 6.6a. Open symbols denote samples with a graphite back gate (the two samples discussed in this chapter, two samples by Li et al. [50] and a sample which was measured by Marius Eich [104]). The mobility of these samples is not necessarily larger than the mobility of the samples without graphite back gate (compare the mobility of the samples by Zhu et al. [51]). Samples with a graphite back gate systematically result in high resistivity in presence of an electric field however. This is a strong indication that either the aforementioned improvement in screening or the changed stray field compared to samples with a Si back gate reduces the number of mid-gap states, leading to a closer match with the theoretically predicted behavior.

Out of the samples with a graphite back gate, sample H shows the lowest resistivity, possibly due to the presence of bubbles in the stack under the top gate. It may therefore be important to avoid bubbly regions when aiming for high resistivity. Nevertheless even sample H fulfils the criterion for tunnel barriers of nanostructures $R \gg R_{\mathrm{K}}$ [9]. Graphite back gates therefore open new perspectives for electrostatical definition of nanostructures in bilayer graphene.

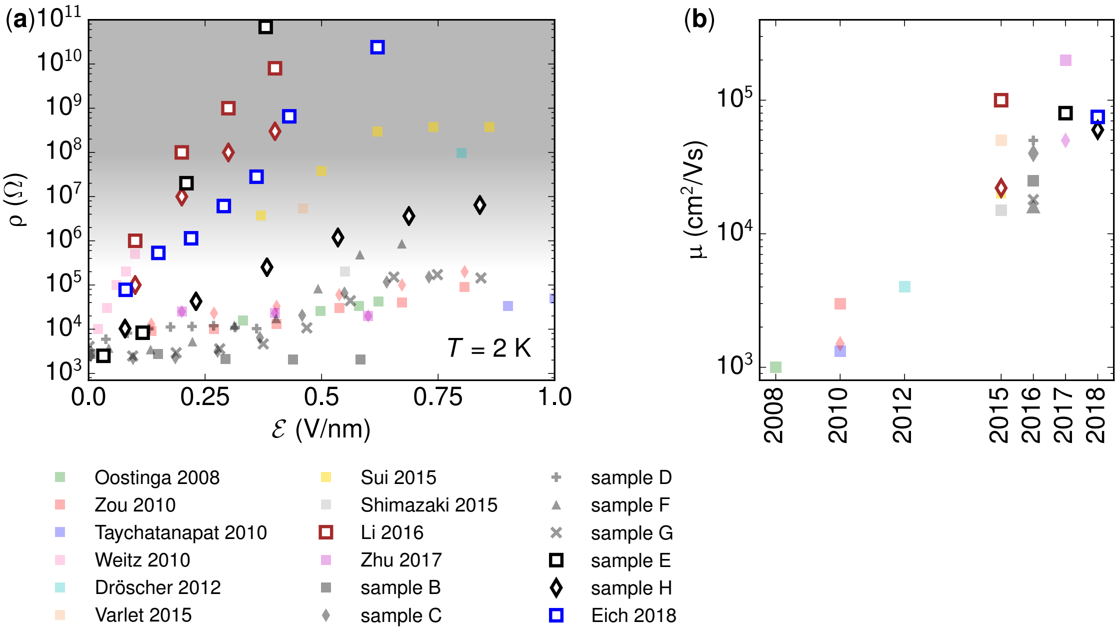

Figure 6.6: (a) Resistivity as a function of electric field at $T = 2$ K. Different symbols denote different samples. Open symbols denote samples with graphite back gate (b) Mobility as a function of year of publication or measurement.

Chapter 7

Electrostatically induced quantum point contacts in bilayer graphene

Parts of this chapter are based on the work:

Electrostatically induced quantum point contacts in bilayer graphene
Hiske Overweg, Hannah Eggimann, Xi Chen, Sergey Slizovskiy, Marius Eich, Pauline Simonet, Riccardo Pisoni, Yongjin Lee, Kenji Watanabe, Takashi Taniguchi, Vladimir I. Fal'ko, Klaus Ensslin, Thomas Ihn
Nano Letters **18**, 553-559 (2018)

7.1 Introduction

In the previous chapter we have shown that it is possible to induce a resistance on the order of gigaohms in encapsulated bilayer graphene samples with a graphite back gate and metallic top gates. In this chapter we exploit this property to define quantum point contacts (QPCs) in bilayer graphene. Several research groups have created electrostatically confined one-dimensional channels or quantum dots [105–107] in bilayer graphene, where the carriers are guided via a split gate structure with depleted graphene regions below the biased split gates. In these experiments however, the minimal conductance achievable in such geometries is limited by leakage currents below the split gates, presumably caused by hopping transport or a small energy gap. We will see that the graphite back gate helps to overcome this problem.

The sample geometry, discussed in section 7.2, differs from the conventional design of a quantum point contact: an extra gate is added on top of the channel defined by the split gates. Section 7.3 focuses on the conductance at $B = 0$ T, where we observe device-dependent conductance quantization of $\Delta G = 2\ e^2/h$ and $\Delta G = 4\ e^2/h$. The magnetic field dependence of the QPC modes, which shows an intricate pattern of level crossings, is discussed in section 7.5. Section 7.6 discusses finite bias measurements both with and without magnetic field. Section 7.7 concludes this chapter.

7.2 Sample geometry

In this chapter we will study three samples. Samples E and H were already introduced in chapter 6. Sample I will be introduced below. In an additional lithography step, a split gate geometry was added to samples E and H, which was then covered by another insulating layer and a gate on top of the channel. The geometry is sketched in Fig. 7.1a. In GaAs, similar QPC gate geometries have been studied [108]. The combination of split gates, back gate and channel gate is essential to separately tune the gap and the position of the Fermi level in the regions underneath the split gates as well as the carrier density in the channel.

Fig. 7.1b shows an AFM image of sample E. On top of the device two 300 nm wide split gates (SG), separated by 100 nm, were added next to the top gate (TG). Atomic layer deposition was performed to add a dielectric layer (Al_2O_3, 60 nm). Finally, another 200 nm wide gate, referred to as channel gate (CH), was evaporated onto the channel defined by the split gates (see Fig. 7.1c). Sample H was produced in the same way but has a thinner Al_2O_3 layer (20 nm), a smaller channel width (80 nm) and a narrower channel gate (60 nm). In sample H, two separate pairs of contacts are used to probe either the graphene region with top gate, or the graphene region with split gate geometry.

Sample I, also consisting of a bilayer graphene flake encapsulated in hBN on top of a graphite back gate, was stacked inside an Ar glovebox by Peter Rickhaus. Six pairs of split gates in series were deposited on top of the stack. An AFM image of the sample, made prior to the deposition of the channel gates, is shown in Fig. 7.1d. The four QPCs showing quantized conductance are labelled QPC M (80 nm wide channel) QPC L1,L2 (180 nm wide channel) and QPC S (50 nm wide channel) [1]. The channel gates were all 200 nm wide.

More details about the sample fabrication and geometry can be found in appendix E.

To illustrate the basic idea of electrostatic confinement in bilayer graphene, we take a look at Fig. 7.1e. It shows a schematic of the dispersion relation at three different points across the QPC, indicated in Fig. 7.1b. When the Fermi level under the split gates lies in the gap (I., III.) and the Fermi level in the channel lies in the conduction band (II.), charge carriers can only flow through the narrow channel. A finite element simulation of the electrostatic potential can be found in appendix F.

---

[1] For one of the other QPCs, a split gate is not working. The last QPC can be pinched off, but does not show any quantized conductance (see Appendix G.2).

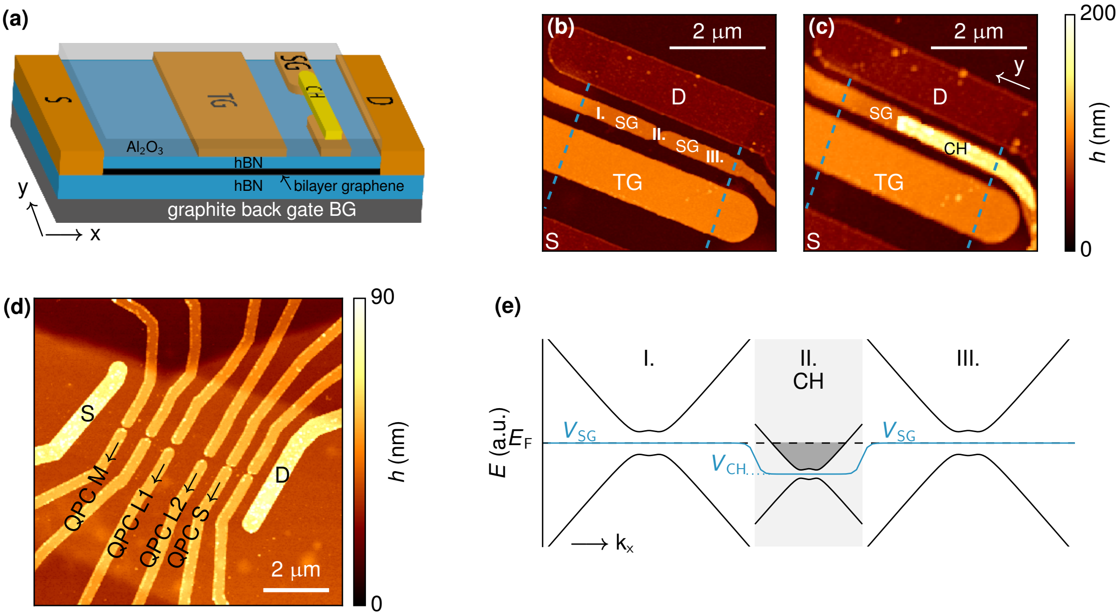

Figure 7.1: Sample layout. (a) Schematic of sample E. A bilayer graphene flake is encapsulated in hexagonal boron nitride. It is contacted by a source (S) and drain (D) contact and has a graphite back gate (BG) below, a top gate (TG), two split gates (SG) and a channel gate (CH) on top. The channel gate is separated from the split gates by a dielectric layer of Al_2O_3. (b) Atomic force microscopy image of sample E prior to deposition of the channel gate. The position of the graphene flake is indicated by blue dashed lines. (c) Atomic force microscopy image of sample E with the channel gate. (d) Atomic force microscopy image of sample I, with six pairs of split gates in series, prior to the deposition of the channel gates. (e) Model of the band structure along the y-direction with the electrostatic potential indicated by the blue line. The Fermi level under the split gates lies in the band gap. The channel gate induces a finite carrier density in the channel.

7.3 Resistance in the bulk at $B = 0$ T

Unless stated otherwise, the measurements in the following sections were performed at $T = 1.7$ K. An AC bias voltage of 50 μV was applied and the current I was measured using low-frequency lock-in techniques.

Figure 7.2a shows the resistance of sample E as a function of split gate voltage (V_{SG}) and back gate voltage (V_{BG}), with a grounded top gate and channel gate. Lines of enhanced resistance follow the same pattern as in Fig. 6.3a. In contrast to Fig. 6.3a, the resistance along the electric field axis does not increase beyond about $R = 5$ kΩ (note the different color scales of Figs. 7.2a and 6.3a). This is because charge carriers can flow through the channel between the split gates.

The channel can be depleted, however, by applying a channel gate voltage of $V_{CH} = -12$ V. The blue triangles in Fig. 7.2b show the resistance as a function

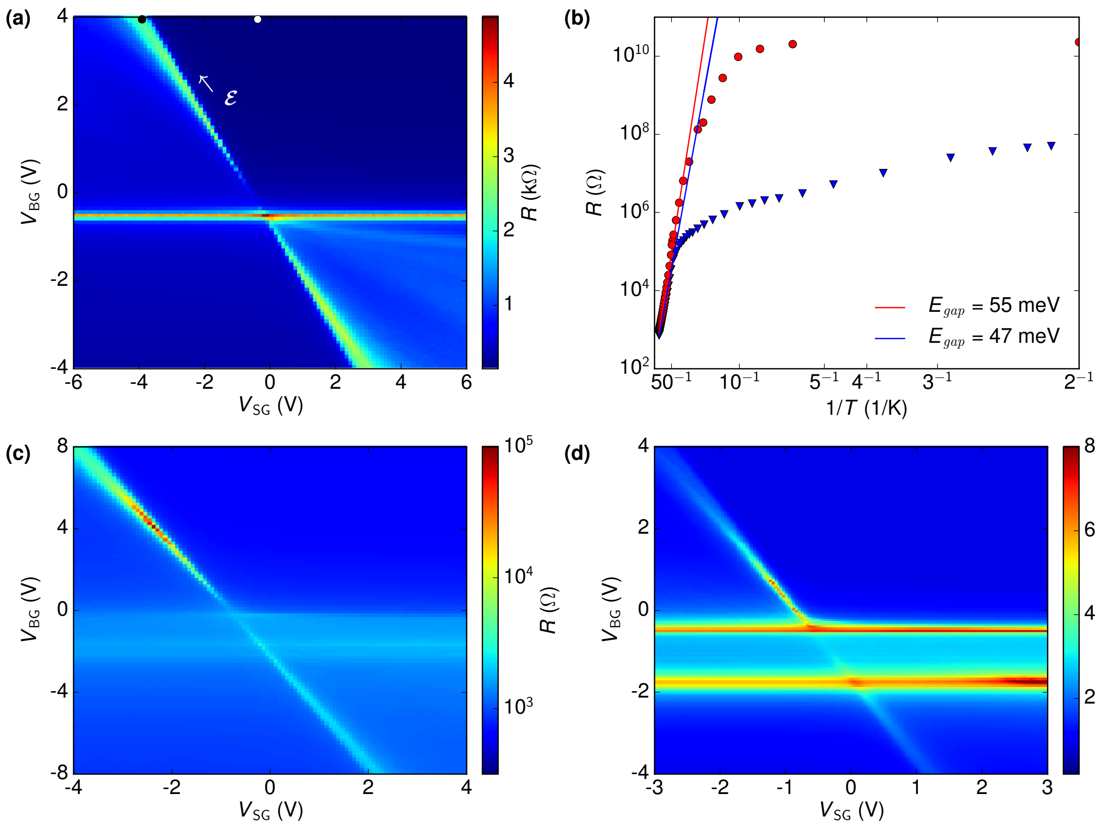

Figure 7.2: (a) Resistance of sample E as a function of split gate voltage and back gate voltage. (b) Temperature dependence of the resistance of sample E. The blue triangles show the resistance of the QPC for $V_{\mathrm{BG}} = 4$ V, $V_{\mathrm{SG}} = -3.9$ V (black dot in (a)) and $V_{\mathrm{CH}} = -12$ V. For comparison the red dots show resistance under the full top gate (TG in Fig. 7.1). (c),(d) Resistance of sample H and I respectively as a function of split gate voltage and back gate voltage.

of inverse temperature for ($\mathrm{V_{SG}}$,$\mathrm{V_{BG}}$) = $(-3.9, 4)$ V (black dot in Fig. 7.2a) and $V_{\mathrm{CH}} = -12$ V, which gives the highest resistance achievable at $T = 1.7$ K using the split gates and the channel gate. In the high temperature regime a gap energy of $E_{gap} = 47$ meV can be extracted. The resistance deviates from the activated behavior below $T \sim 50$ K and goes up to $R = 50$ MΩ at $T = 1.7$ K, which is three orders of magnitude higher than the resistance quantum h/e^2. In sample H the maximal resistance achieved with the split gates and the channel gate is $R = 20$ MΩ at $T = 1.7$ K. These results are in contrast with previous works on bilayer graphene QPCs, which never showed a conductance below $G = e^2/h$.[105, 106] These results show that it is not only possible to achieve high resistances with a rather wide uniform gate, but also with a combination of three narrower gates. The band gap underneath the split gates is sufficient to suppress conductance when the Fermi energy is in the gap.

Figures 7.2c,d show the resistance of samples H and I as a function of split gate and back gate voltage, with grounded channel gates. The resistance of sample H goes up significantly higher than the other samples. Apparently the narrow channel in this sample can already be depleted when $V_{\mathrm{CH}} = 0$ V. The resistance of sample I shows an additional line of high resistance at $V_{\mathrm{BG}} = -1.9$ V. The measurement was performed with a voltage applied to a single pair of split gates. The additional line of high resistance corresponds to the charge neutrality point under the five grounded pairs of split gates.

7.4 Conductance in the constriction at $B = 0$ T

We vary the channel gate voltage V_{CH} in the regime where conductance under the split gates is maximally suppressed. For sample E the back gate voltage could not be increased above $V_{\mathrm{BG}} = 4$ V because of the onset of gate leakage, most likely due to the thin hBN layer between the back gate and the contacts. Suppression of conductance under the gates was only reached at $(V_{\mathrm{SG}}, V_{\mathrm{BG}}) = (-3.9, 4)$ V (see black dot in Fig. 7.2a). The conductance G at this operating point as a function of channel gate voltage V_{CH} is shown in Fig. 7.3a. A series resistance of $R_{\mathrm{S}} = 150\ \Omega$ was subtracted, which was determined by measuring the resistance at $(\mathrm{V}_{\mathrm{SG}}, \mathrm{V}_{\mathrm{BG}}) = (-0.4, 4)$ V (see white dot in Fig. 7.2a). This point corresponds to uniform doping throughout the sample. The conductance shows plateaus at $G = 8, 10, 12, 14, 16, 18\ e^2/h$. No plateaus are discernible below $G = 8\ e^2/h$. To our knowledge this is the largest number of conductance plateaus observed in bilayer graphene to date. At $V_{\mathrm{CH}} = -12$ V the channel is depleted, reaching a resistance of $R = 50\ \mathrm{M}\Omega$.

Sample H has a larger back gate voltage range with gate leakage smaller than 0.1 nA. Figure 7.3b shows its conductance as a function of channel gate voltage for a set of back gate - split gate voltage pairs. Under the split gates, increasing voltage differences $V_{\mathrm{BG}} - V_{\mathrm{SG}}$ correspond to an increasing electric field $\mathcal{E}$ along the charge neutrality line (cf. Fig. 7.2a). For each curve, a series resistance equal to the resistance measured at uniform doping at the corresponding back gate voltage was subtracted. Throughout the whole range, plateaus can be observed slightly below $G = 4, 12\ e^2/h$ (see blue arrows). For $V_{\mathrm{BG}} < 6$ V a plateau occurs slightly below $8\ e^2/h$ as well (dashed blue arrow). In the range above $G = 12\ e^2/h$ small oscillations are observed which cannot be identified to be quantized conductance plateaus.

The conductance of the different channels in sample I is shown in Figs. 7.3c,d. We again subtracted a series resistance equal to the resistance measured at uniform doping at the corresponding back gate voltage for each curve. The narrowest QPC (QPC S, Fig. 7.3c, gray line) only shows a few plateaus within the channel gate voltage range. Likewise we see that the widest QPC (QPC L1, Fig. 7.3d) shows population of more modes than the middle QPC (Fig. 7.3c) within a small channel gate voltage range. This is in agreement with the expected larger energy spacing

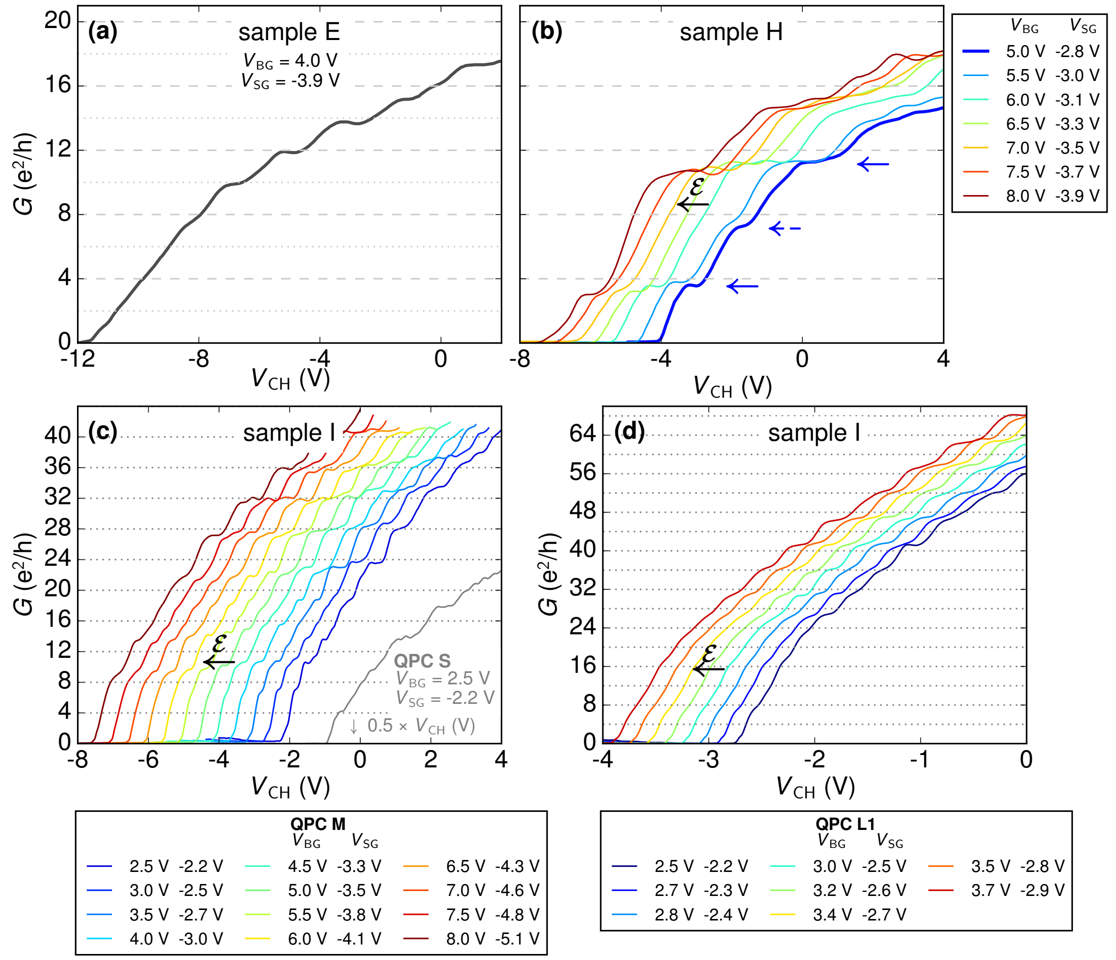

Figure 7.3: (a) Conductance G of the induced channel in sample E as a function of V_{CH} at $B = 0$ T for the gate voltage configuration at the black dot in Fig. 7.2a. The conductance shows a number of steps of $\Delta G = 2\ e^2/h$. (b) Conductance of the channel in sample H as a function of channel gate voltage V_{CH} at $B = 0$ T for several combinations of back gate and split gate voltage. The conductance shows plateaus slightly below $G = 4, 8, 12\ e^2/h$. (c) Conductance of QPC S (in gray) and QPC M (in color) in sample I as a function of channel gate voltage. Several steps of $\Delta G = 4\ e^2/h$ can be identified. (d) Conductance of QPC L1 in sample I as a function of channel gate voltage.

of the modes for a narrower channel. In the higher mode regime $G > 20\ e^2/h$ conductance plateaus with a step size of $\Delta G = 4\ e^2/h$ can be identified. The lower modes are less pronounced, especially in QPC L1.

Samples H and I could also be depleted completely at $V_{\mathrm{BG}} = -8$ V, when the entire sample is p-doped. The conductance as a function of channel gate voltage in this setting shows several smaller kinks, but no quantized conductance plateaus. In sample E it was not possible to deplete the channel in the p-doped regime, most likely because of the limited back gate voltage range.

Our results fit well into the landscape of experiments on single- and bilayer graphene QPCs published previously, where lifted degeneracies were observed in some but not all samples. Theoretically, for pristine bilayer graphene, steps of $\Delta G = 4\ e^2/h$ are expected because of spin- and valley-degeneracy, as observed in samples H and I. At the same time the observed step size of $\Delta G = 2\ e^2/h$ in sample E, witnessing a lifted degeneracy, is in agreement with other experimental works on bilayer graphene [105, 106]. In monolayer graphene, conductance quantization with steps of $\Delta G = 2\ e^2/h$ was observed in both limits of low [109, 110] and high [111] mode number. However, Kim et al. [112] reported conductance quantization with a step size $\Delta G = 4\ e^2/h$ in an electrostatically induced channel in monolayer graphene. Zimmermann et al. [113] studied a QPC in single layer graphene in the quantum Hall regime where a step size of $\Delta G = 1\ e^2/h$ is observed.

We speculate that the difference in the observed degeneracies in sample E on the one hand and samples H and I on the other hand is caused by the residual disorder in the devices. In the quantum Hall regime all degeneracies in the lowest Landau level are lifted in our samples (see below), which demonstrates good sample quality. Yet at zero magnetic field, the lack of perfect flatness of plateaus, the deviations from the expected plateau values, the occasionally missing plateaus, and the absence of plateaus in a p-doped channel indicate that a further increase in device quality, currently out of reach, would lead to improvements. Beyond that, strain effects could modify the potential landscape. In GaAs heterostructures, it is well known that a difference in thermal expansion coefficient between the metal gates evaporated on top of the semiconductor wafer and the semiconductor material itself can lead to a strain-induced change of the potential of 5-10% [114]. In our case, the hBN layer separating the metal gate from the graphene layer is comparatively thinner, and one can imagine that strain effects could also lead to modifications of the potential, in addition to the electrostatic definition of the QPC. While further improvements in device quality will lead to better reproducibility among different devices and allow for investigation of more subtle interaction effects, such as spontaneous spin polarization [115], at present the microscopic origin of the lifted degeneracy and the missing plateaus at low mode numbers in device E and I remains unknown.

7.5 Magnetotransport

7.5.1 Samples E and H

A magnetic field has the potential to provide further insights into degeneracy lifting in QPCs. Figure 7.4a(b) shows the conductance of sample E(H) as a function of V_{CH} for selected magnetic field strengths. For these measurements, the density in the bulk of the sample is considerably higher than the density in the channel. The conductance is therefore governed by the filling factor of the channel (see Appendix G.1). In a magnetic field of $B = 7$ T we observe that the four-fold degeneracy of the lowest Landau level is completely lifted in both samples, demonstrating the high quality of the samples [7]. Sample E shows a step size of $\Delta G = 4\ e^2/h$ at intermediate magnetic fields (see curve at $B = 2.5$ T). This is surprising, since the step size at $B = 0$ T (Fig. 7.3a) and $B = 1.6$ T (see arrows in Fig. 7.4a) is only $\Delta G = 2\ e^2/h$ for this sample. In sample H, no clear quantization of the levels is observed at intermediate magnetic fields.

The transconductance as a function of V_{CH} and B, shown in Fig. 7.4c,d, provides a more complete picture. Transitions between quantized modes are seen as dark lines. In sample E the transitions between the plateaus are more pronounced than in sample H. In both samples, these lines start out vertically at low magnetic fields, and bend over between $B = 1$ T and $B = 2$ T towards more positive gate voltages, ending up as straight lines with finite slope at high fields. This behavior is reminiscent of the magnetoconductance of high quality QPCs, for example in GaAs, where the low magnetic field conductance is confinement-dominated, whereas the high magnetic field conductance is determined by edge channels formed in crossed electric and magnetic fields. The effect is known as the magnetic depopulation of magnetoelectric subbands [116]. Also in our samples, filling factors can be assigned to the light regions between the lines as indicated in the figure. However, when the magnetic field is decreased towards the confinement dominated regime, the mode structure appears to be much more complicated than in GaAs.

Lacking a detailed theory we propose a heuristic model which describes the level transitions of sample E as a function of magnetic field. In analogy to magnetic depopulation in GaAs 2DEGs [117], we assume that the energy separation of the modes in the channel is given by

$$E_N = \mathrm{sgn}(N)\hbar\Omega\sqrt{N(N-1)}, \qquad \Omega = \sqrt{\omega_0^2 + \omega_c^2} \tag{7.1}$$

where ω_0 is the frequency of the electrostatic confinement potential in the absence of a magnetic field, and ω_c is the cyclotron frequency, given by $\omega_c = eB/m^*$. The gate voltage axis can be converted into an energy scale assuming a linear conversion from gate voltage V_{CH} to energy $E = \alpha_{CH} e(V_{\mathrm{CH}} - V)$. It is impossible to fit a mode spectrum as that described by Eq. 7.1 to all the levels observed in Fig. 7.4c using α_{CH}, V and ω_0 as free fitting parameters. Yet by extending the model with a second set of parameters α'_{CH}, V' and ω'_0 it is possible to capture the trends of the

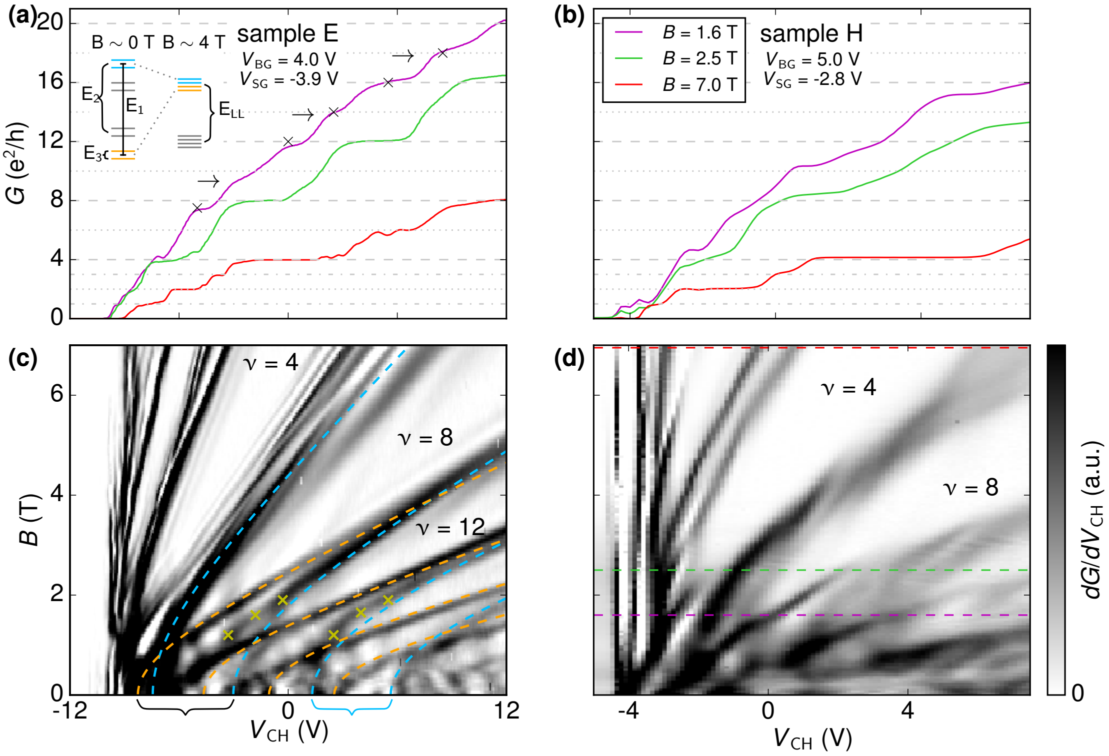

Figure 7.4: (a) Conductance of sample E for several magnetic field strengths. The plateaus at 10, 14 and 18 e^2/h are still present at $B = 1.6$ T (see arrows), but disappear in higher magnetic fields. At $B = 7$ T (red line) plateaus are present at 1, 2 ,3, 4 e^2/h. (b) Conductance of sample H for several magnetic field strengths. (c) Transconductance of sample E as a function of channel gate voltage V_{CH} and magnetic field B. The blue and orange dashed lines both follow the model described by Eq. 7.1. (d) Transconductance of sample H as a function of channel gate voltage V_{CH} and magnetic field B. The transitions between modes are less pronounced than in sample E. Horizontal dashed lines correspond to the line cuts in (a),(b).

level crossings in the low magnetic field regime. This is demonstrated by the dashed orange and blue lines in Fig. 7.4c. The employed parameters are $\hbar\omega_0 = 7.5$ meV, $\alpha_{CH} = 1.75 \times 10^{-3}$, $V = 13.5$ V, $\hbar\omega_0' = 5$ meV, $\alpha_{CH}' = 1.4 \times 10^{-3}$ and $V' = 17$ V. We want to stress that the model is purely heuristic. It was designed to capture the dominant features of the experiment. The two different frequencies could imply that the two valley/spin split modes may have different effective masses. The difference between V and V' indicates an energy offset between the two sets of levels. The model captures the main features of the data, except for the part where $V_{\mathrm{CH}} < -10$ V (where the conductance at $B = 0$ T already deviates from the expected pattern), and the features marked by yellow crosses in Fig. 7.4c. The parameters $\hbar\omega_0$ and $\hbar\omega_0'$ are similar to the curvature of the harmonic potential calculated in a COMSOL simulation of the electrostatic potential of the device (see appendix F).

The data suggest that around $B = 4$ T, the spin and valley splittings are too small to be resolved. The only relevant energy spacing is the Landau level spacing E_{LL} (see inset of Fig. 7.3a). Lowering the magnetic field, the relative influence of the electrostatic potential compared to the magnetic confinement grows, which lifts a degeneracy (the blue and orange dashed lines move apart). The black curly bracket in Fig. 7.3c indicates the energy range of the lifted degeneracy at $B = 0$ T (E_1 in Fig. 7.3a), which seems to have grown larger than the mode spacing indicated by the blue curly bracket (E_2 in Fig. 7.3a). The remaining twofold degeneracy implies that the energy scale $E_3 = 0$. Although the model suggests a degeneracy lifting larger than the mode spacing of the QPC, we currently do not know which mechanism could be responsible for such a drastic effect.

Another aspect which may contribute to the crossing mode pattern is the fact that the channel gate voltage changes the electric field inside the channel. Bilayer graphene exhibits a valley splitting of the Landau levels which depends on the electric field [82, 85, 118]. In the devices presented here, the charge carrier density and the electric field in the channel cannot be varied independently, complicating a systematic study of the effect of the electric field.

7.5.2 Sample I

The transconductance of the QPCs in sample I, shown in Fig. 7.5, exhibit an even more pronounced pattern of level crossings (marked with colored dots) as a function of channel gate voltage and magnetic field. For QPC M, the fourfold degeneracy at $B = 0$ T is lifted at $B > 0.2$ T. The levels cross around $B \approx 1$ T, which leads to a level sequence of $G = 6,\ 10,\ 14,\ \dots\ e^2/h$ in this magnetic field range (see pink numbers in Fig. 7.5a). The levels cross once more in a higher magnetic field, after which the conventional sequence of fourfold degenerate bilayer graphene Landau levels is observed (i.e. $G = 4,\ 8,\ 12,\ \dots\ e^2/h$). Because of the level crossings, the Nth Landau level consists of QPC modes $N-1$ and $N+1$. In the upper right corner of Fig. 7.5a, no quantum Hall states are observed. In this regime the filling factor in the channel is larger than the filling factor in the bulk. Therefore the conductance is no longer solely determined by the conductance of the channel.

Figure 7.5b shows the transconductance of QPC M measured with a more extreme setting of the back gate and split gate voltages. This leads to a higher electric field both under the split gates and inside the channel. On a qualitative level the pattern of level crossings is the same.

In Appendix G.3 the transconductance of QPC M is shown in the regime where the channel is p-doped. Although no clear quantization is observed at $B = 0$ T (Fig. G.3a), the higher modes show a similar pattern of mode crossings (Fig. G.3b) in presence of a magnetic field.

QPC S also shows a similar pattern of level crossings, see Fig. 7.5c. Because of the narrower QPC channel, the transition to the quantum Hall regime occurs in higher fields, as expected.

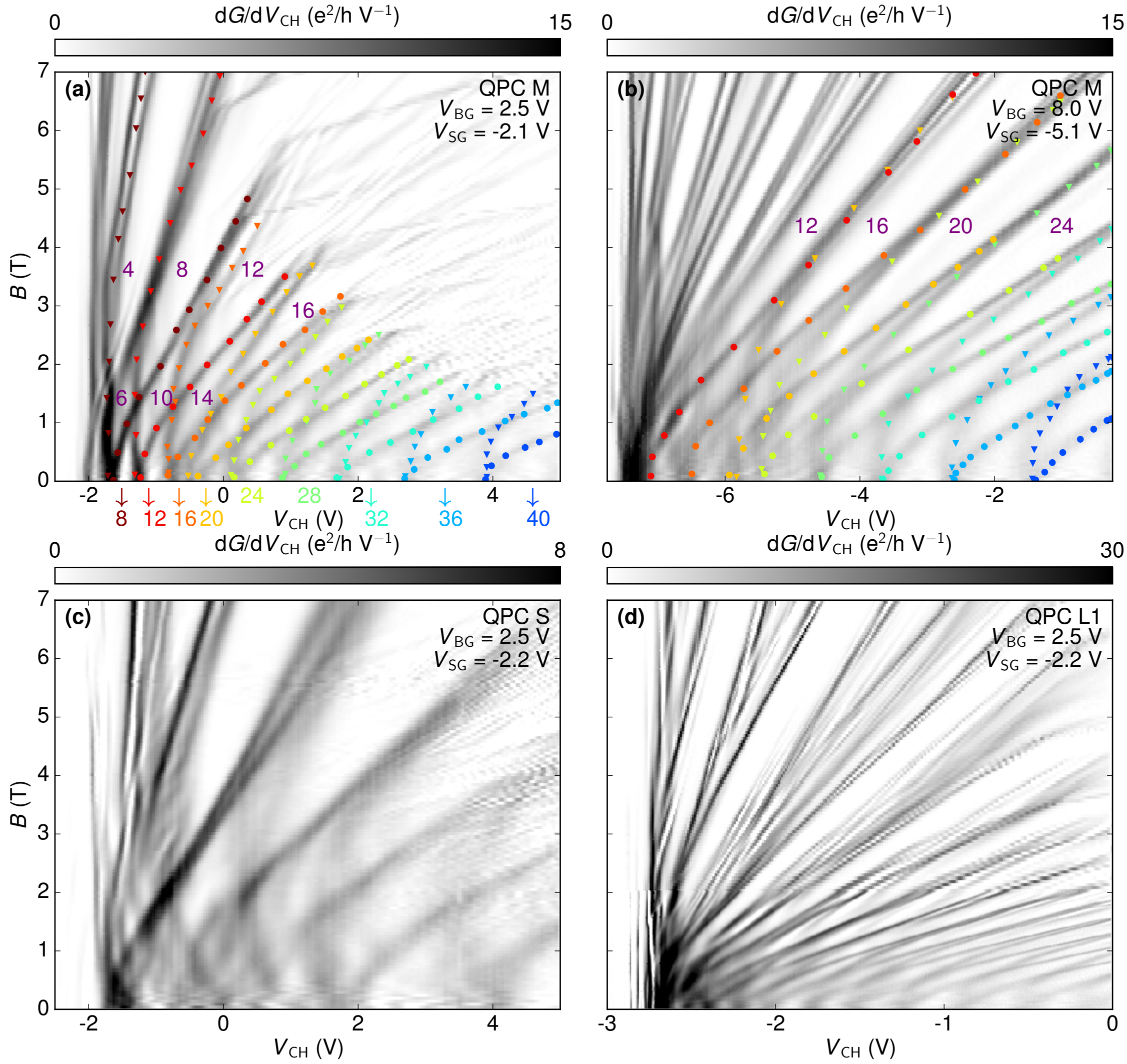

Figure 7.5: (a) Transconductance of QPC M in sample I as a function of channel gate voltage V_{CH} and magnetic field B measured at $V_{\mathrm{BG}} = 2.5$ V and $V_{\mathrm{SG}} = -2.1$ V. Colored numbers correspond to conductance values of the different modes. (b) Transconductance of QPC M for the gate voltage settings $V_{\mathrm{BG}} = 8.0$ V and $V_{\mathrm{SG}} = -5.1$ V. (c) Transconductance of QPC L1. (d) Transconductance of QPC S.

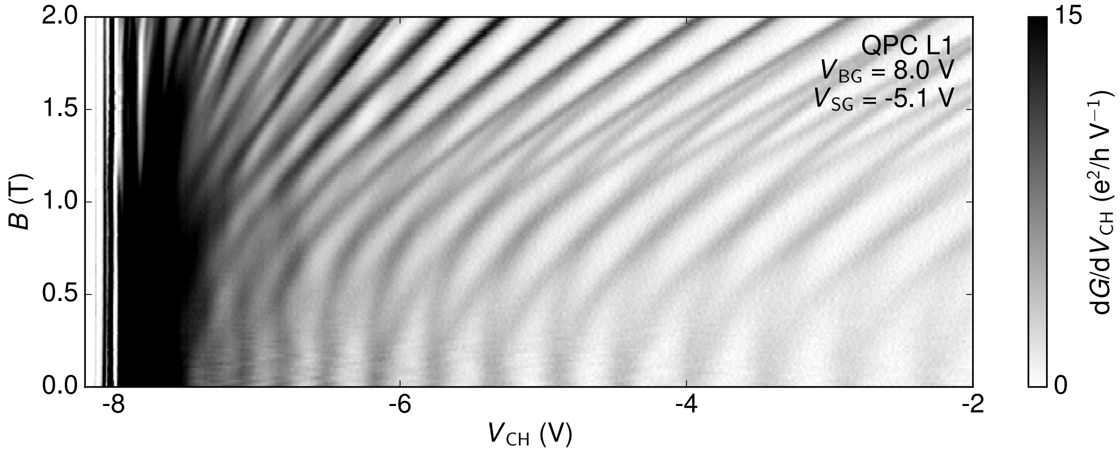

Figure 7.6: Transconductance of QPC L1 in sample I as a function of channel gate voltage V_{CH} and magnetic field B measured at $V_{\mathrm{BG}} = 8$ V and $V_{\mathrm{SG}} = -5.1$ V

QPC L1 (Fig. 7.5d) and L2 (not shown) show level crossings in a low magnetic field of $B \approx 1$ T. A zoom of the low magnetic field regime for a different gate voltage setting is shown in Fig. 7.6. A dozen of level crossings can be identified over the extensive channel gate voltage range. We again observe a merging of a QPC mode with its next nearest neighbor mode in the quantum Hall regime.

Using the finite bias measurements presented in section 7.6, the channel gate voltage axis can be converted into an energy scale. From Fig. 7.5 we can therefore extract the splitting of the QPC modes as a function of magnetic field. The result is plotted in Fig. 7.7. The different colors correspond to different modes. All modes show a linear dependence of the energy splitting on the magnetic field. The corresponding g-factors are $g^* = 100 - 300$, which makes it clear that the splitting cannot be explained by Zeeman splitting, for which a g-factor of 2 is expected and confirmed in Ref. [104]. For the middle QPC we observe a clear dependence of the splitting on the mode number. At a fixed magnetic field, higher modes exhibit a larger splitting. For the wide QPC this effect is four times weaker. Comparing Fig. 7.7a and Fig. 7.7b we conclude that the mode splitting is independent of the electric field within the range of the measurements. This excludes an explanation in terms of the valley Hall effect [48, 49, 119].

The mechanism responsible for the splitting and recombination of the modes in the QPCs is currently not known. The recombination of QPC mode $N - 2$ with QPC mode N might be related to the fact that the Dirac spinor describing the Nth Landau level wave function in bilayer graphene consists of the harmonic oscillator states $N - 2$ and N [77].

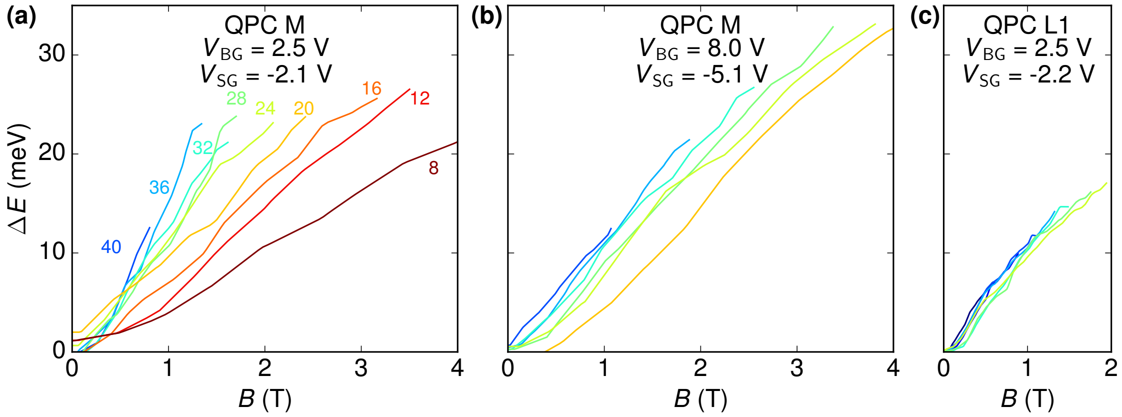

Figure 7.7: (a) Energy splitting of the modes of QPC M as function of magnetic field. Different colors correspond to different modes (see also Fig. 7.5a). (b) Same as (a) for the gate voltage setting of Fig. 7.5b. (c) Energy splitting of the modes of QPC L1 as a function of magnetic field for the gate voltage setting of Fig. 7.5d.

7.6 Finite bias spectroscopy

Finite bias measurements were performed to extract mode spacings. Figure 7.8a shows the conductance as a function of V_{CH} and the transconductance dG/dV_{CH} as a function of source drain bias measured at $B = 0$ T for QPC L1. Diamond-shaped minima in the transconductance are observed at the positions of the conductance plateaus. From the diamond pattern an energy spacing on the order of $\Delta E \approx 3$ meV can be extracted.

The pattern gets more pronounced at $B = 0.5$ T, as shown in Fig. 7.8b. At this magnetic field, the unconventional plateau sequence of $G = 4N + 2\ e^2/h$ with $N \in \mathbb{Z}^+$ is observed (see red dotted lines). From the increasing diamond size with increasing channel gate voltage we conclude that higher modes have a larger energy spacing. This is in agreement with the Comsol simulations shown in appendix F, which show that the confinement potential gets steeper for more positive channel gate voltage. At $B = 0.9$ T the higher modes show a twofold degeneracy (see red dotted lines in Fig. 7.8c). The corresponding bias diamonds are therefore smaller than those observed at lower fields. When increasing the magnetic field, the fourfold degeneracy is restored and the diamond size increases again (Fig. 7.8d). This is in agreement with the level crossings observed in section 7.5.2.

The extracted lever arm α_{CH} for conversion of channel gate voltage into energy ($E = \alpha_{CH} e V_{\mathrm{CH}}$) can be read from the slopes of the finite bias diamonds. For QPC L1 $\alpha_{CH} = 20 \times 10^{-3}$ and for QPC M $\alpha_{CH} = 14 \times 10^{-3}$ (diamonds shown in appendix G.4), in agreement with the fact that for the narrower QPC the channel gate is more screened by the split gates and therefore has a smaller influence.

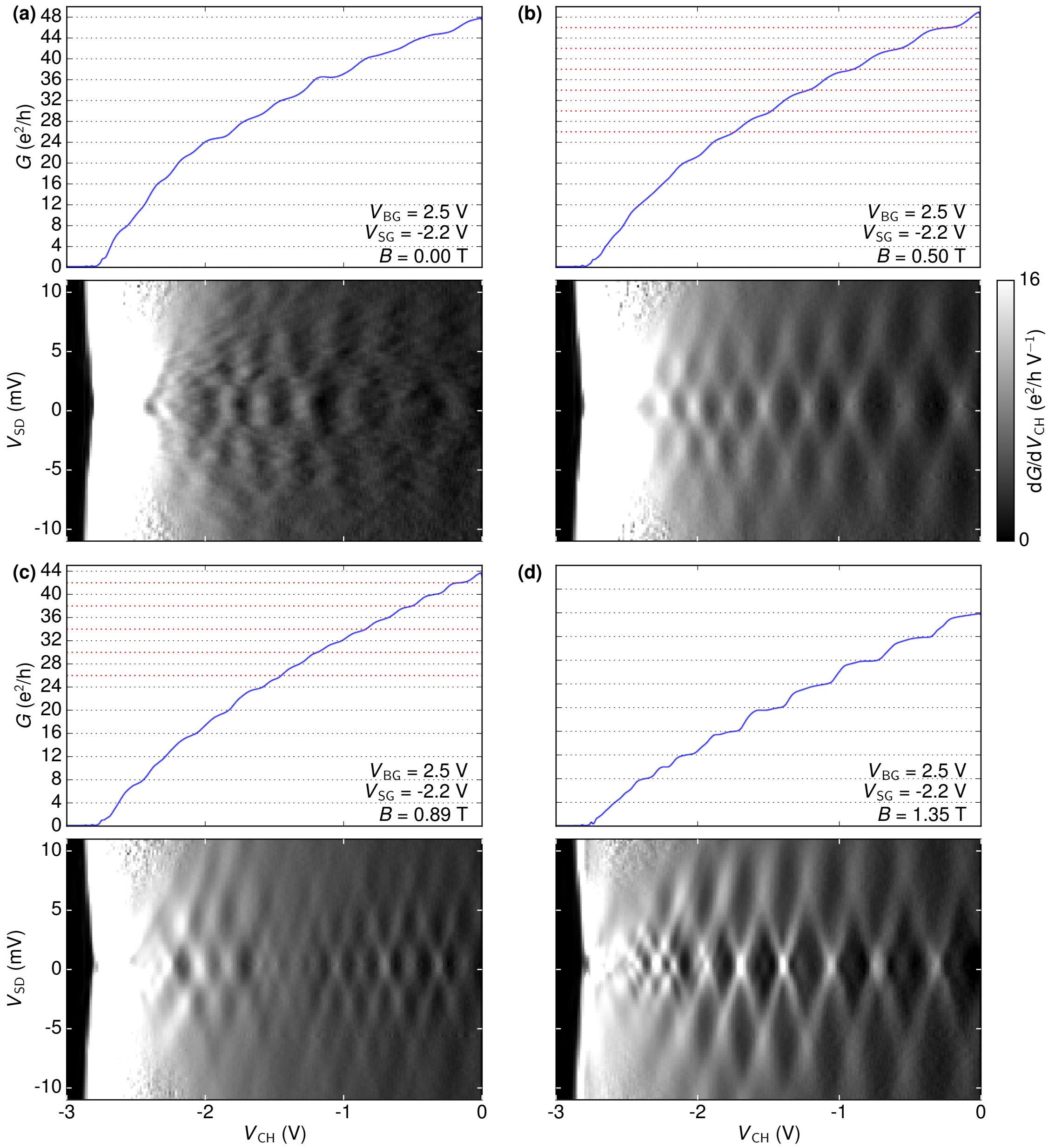

Figure 7.8: (a) Top: Conductance as a function of V_{CH} for QPC L1 at $B = 0$ T. Bottom: Transconductance as a function of V_{CH} and V_{SD}. Finite bias diamonds coincide with conductance plateaus. (b),(c),(d) Same as (a) for various magnetic field strengths.

7.7 Conclusion

We have defined QPCs in hBN-encapsulated bilayer graphene samples with a graphite back gate and we observe the following:

- In all samples, the channels can be fully depleted by gating, in contrast to previous works [105, 106].
- All samples show quantized conductance, though with different degeneracies.
- All samples show the expected quantum Hall plateaus with fourfold degeneracies at high fields and complete lifting of degeneracies for the lowest Landau levels.
- All samples show an intricate crossover regime between zero magnetic field and the quantum Hall regime, where level crossings and avoided crossings occur.

The different step sizes of $\Delta G = 2\ e^2/h$ and $\Delta G = 4\ e^2/h$ in the samples might be due to a different disorder potential or different strain patterns. Several factors, such as the reduced transmission of the modes of sample H and the absence of conductance quantization in the p-doped regime, indicate that mesoscopic details of the samples play an important role. Realizing one-dimensional nanostructures in bilayer graphene by electrostatic gating paves the way toward controllable quantum dots in bilayer graphene, which will be the topic of the next chapter.

Chapter 8

Edge channel confinement in a bilayer graphene *n*-*p*-*n* quantum dot

This chapter is based on the work:

Edge channel confinement in a bilayer graphene *n*-*p*-*n* quantum dot
Hiske Overweg, Peter Rickhaus, Marius Eich, Yongjin Lee,
Riccardo Pisoni, Thomas Ihn, Klaus Ensslin
New Journal of Physics **20**, 013013 (2018)

8.1 Introduction

In this chapter we study the QPC geometry of sample E, introduced in Chapter 7, in a different regime. We combine electrostatic and magnetic confinement to define a quantum dot in bilayer graphene. We again exploit the tunability of the band structure to define a nanostructure: by opening a band gap under the split gates and tuning the gate voltages such that the Fermi level lies in the band gap, flow of charge carriers under the split gates is obstructed. By applying a magnetic field and tuning the back gate to a positive voltage and the channel gate to a negative voltage we couple electron-like edge channels in the bulk of the device to a hole-like region in the channel, thus defining a *p*-doped quantum dot with *n*-doped reservoirs. This situation is drawn schematically in Fig. 8.1a. A side view of the sample is shown in Fig. 8.1b. We observe Coulomb blockade at $B \approx 2$ T. This demonstrates that the coupling of the copropagating modes at the *p*-*n* interface is weak enough to form a tunnel barrier.

The coupling of copropagating edge channels in graphene is a widely studied topic. The first graphene *p*-*n* junction experiments, in graphene on $\mathrm{SiO_2}$ covered by

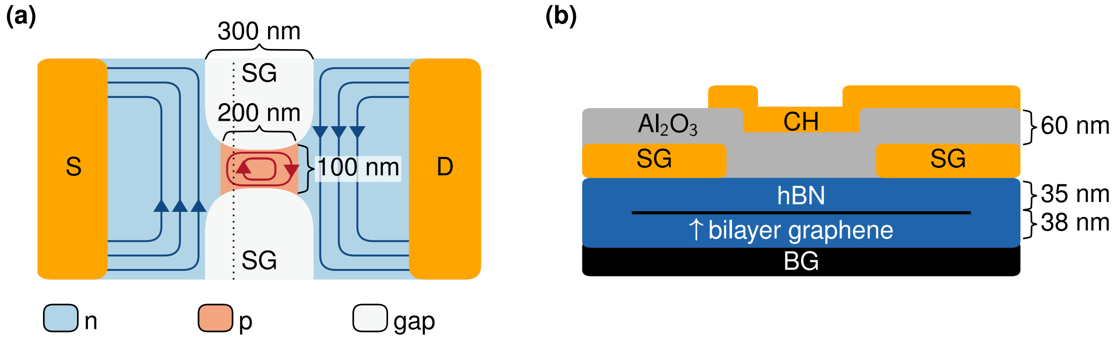

Figure 8.1: (a) Top view of the sample. The graphene is contacted by a source (S) and a drain (D). It can be tuned to the regime where the bulk of the sample is in the n-regime, the channel is in the p-regime and the region under the split gates (SG) is depleted. When applying a perpendicular magnetic field, this leads to confined edge channels in the constriction. (b) Side view of the sample along the dotted line in Fig. 8.1. A bilayer graphene flake is encapsulated in hexagonal boron nitride (hBN). It has a graphite back gate below (BG), two split gates (SG) and a channel gate (CH) on top. The channel gate is separated from the split gates by a dielectric layer of Al_2O_3.

Al_2O_3, showed complete mode mixing of the edge channels travelling along the p-n interface [90]. The situation is schematically drawn in Fig. 8.2a. Cleaner devices with hBN substrate showed a conductance below $G = e^2/h$ in the bipolar regime, suggesting a clear separation between copropagating edge channels [89]. The conductance decreases with increasing magnetic field because an insulating $\nu = 0$ region forms at the p-n interface. Detailed studies of the conductance in the bipolar regime have shown that coupling of the edge channels still occurs at the (rough) device edges [93, 120, 121]. This leads to the formation of an interferometer, as indicated by the two paths around the p-n interface in Fig. 8.2b. Aharonov-Bohm type oscillations have been observed in these devices. In the device we study, the p-n interface is delimited by electrostatically defined boundaries and does not reach the physical edge of the graphene (see Fig. 8.1a). We therefore expect even smaller coupling between the copropagating edge channels.

The behavior of edge channels in quantum dots has been studied in GaAs as well [122–128]. In these devices the polarity of the charge carriers in the dot and in the bulk is the same and the tunnel barriers are defined by electrostatic gating. A schematic of the configuration is shown in Fig. 8.3. In a small device with dot area $A \approx 2\ \mu\mathrm{m}^2$, the Coulomb energy of the dot governs the conductance of the system. Suppose that m Landau levels are completely filled in the confined region and they are tunnel coupled to the leads. When the magnetic field increases by $B = \phi_0/A$, the charge of each of the filled levels increases by one. This will expel m charges

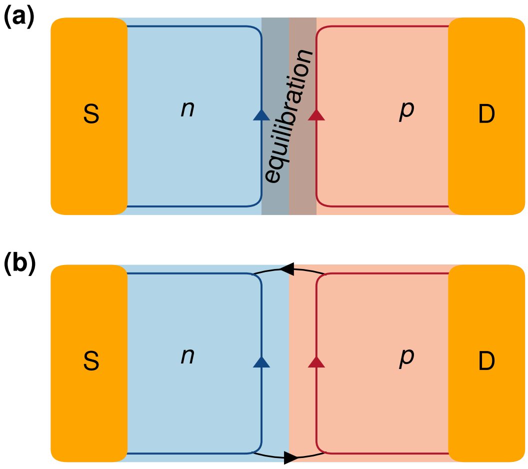

Figure 8.2: Sketches of graphene p-n junctions in the quantum Hall regime. (a) In more disordered devices, the copropagating edge channels mix over the full width of the p-n interface. (b) In cleaner devices, coupling of the edge channels occurs only at the rough device edges, which leads to the formation of an interferometer.

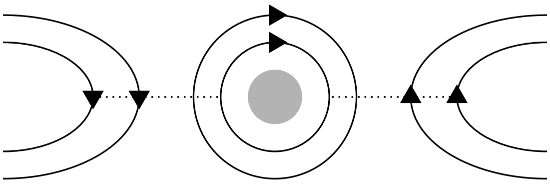

Figure 8.3: Sketch of the edge channel configuration in a quantum dot in GaAs. The edge channels in the leads (left and right) are tunnel coupled (dashed lines) to the edge channels in the central region. The dot is formed by the partially filled Landau level in the central region.

from the partially filled Landau level in the central region which forms the quantum dot [125], resulting in m conductance peaks. When the tunnel coupling between the leads and the central region is weak, the full Landau levels in the central region can act as capacitively coupled dots as well [128]. In the case of a larger device ($A \approx 18\ \mu\text{m}^2$), the charging energy is considerably reduced. The conductance shows oscillations which are caused by Aharahov-Bohm interference of the edge channels circling around the central region. The two phenomena can be distinguished by the slope of the conductance oscillations plotted as a function of gate voltage and magnetic field [125].

8.2 Results and discussions

8.2.1 Characterization measurements

All measurements described in this chapter were performed in a dilution refrigerator at a base temperature of 130 mK. A constant ac voltage bias was applied using conventional lock-in techniques.

To deplete the region under the split gates, we apply a positive voltage to the back gate and a negative voltage to the split gates (or vice versa). This leads to an asymmetry between the two graphene layers, which results in the opening of a band gap [5]. A detailed characterization of the band gap of this device at $B = 0$ T was given in chapter 7. To find the strongest depletion of the region under the split gates in a finite magnetic field, we measure the resistance as a function of split gate voltage V_{SG} and back gate voltage V_{BG} at $B = 2$ T (Fig. 8.4a) and identify the line of highest resistance (white dashed line). For this measurement the channel gate voltage was fixed at a large negative value ($V_{\mathrm{CH}} = -12$ V). With this channel gate voltage setting, the channel is depleted or p-doped for the entire range of the measurement and has a small coupling to the n-doped reservoirs (see also Fig. 8.4b). With a highly resistive channel and a highly n-doped bulk, the changes in resistance observed in this measurement stem primarily from the region under the split gates (see insets). If multiple regions of the device had a considerable influence on the resistance, features with different slopes would be expected, because of different gate capacitances in different regions. The diagonal line of high resistance corresponds to the charge neutrality point under the split gates. Along this line the displacement field increases in the direction of the arrow. We observe an increase of the resistance by two orders of magnitude along this line, ensuing from the increasing band gap under the split gates. The high resistance achieved is important for the formation of a well defined quantum dot. In all following measurements the split gate voltage is adjusted when the back gate voltage V_{BG} is varied (see white dashed line in Fig. 8.4a), so as to keep the region under the split gates depleted. We denote this by V'_{BG}.

We now focus on the effect of the channel gate. The conductance at $B = 2$ T as a function of V'_{BG} and V_{CH} is shown in Fig. 8.4b. In the upper right corner, both the bulk and the channel are n-doped and therefore quantized conductance is observed, similar to Refs. [90, 91]. The observed lines with negative slope are defined by a constant filling factor in the channel. The transitions between the Landau levels are marked by their respective filling factors. They are used to determine the dependence of the charge carrier density on the gate voltages. The conductance inside the channel reaches $G = 16\ e^2/h$, which shows that the edge channels of at least four Landau levels fit inside the channel. The extent of the wave function of the fourth Landau level is $l_B\sqrt{2N+1} = 55$ nm, where l_B is the magnetic length. This extent is indeed smaller than the lithographic width of the channel. In the hatched area at the bottom of the figure the conductance is much lower. In this regime, where the channel is p-doped while the bulk is n-doped, a quantum dot as sketched in Fig. 8.1a forms.

8.2.2 Coulomb blockade measurements

Figure 8.5 shows the main result of this chapter. In Fig. 8.5a the conductance as a function of channel gate voltage and magnetic field is shown. For this measurement a dc bias of $V_{\mathrm{SD,DC}} = 200\ \mu$V was applied to enhance the signal to noise ratio. Lines of higher conductance with a negative slope are observed. To enhance the visibility, we subtract a smoothened background (Fig. 8.5b). When moving in the direction of increasingly negative channel gate voltage, we can interpret each resonance as

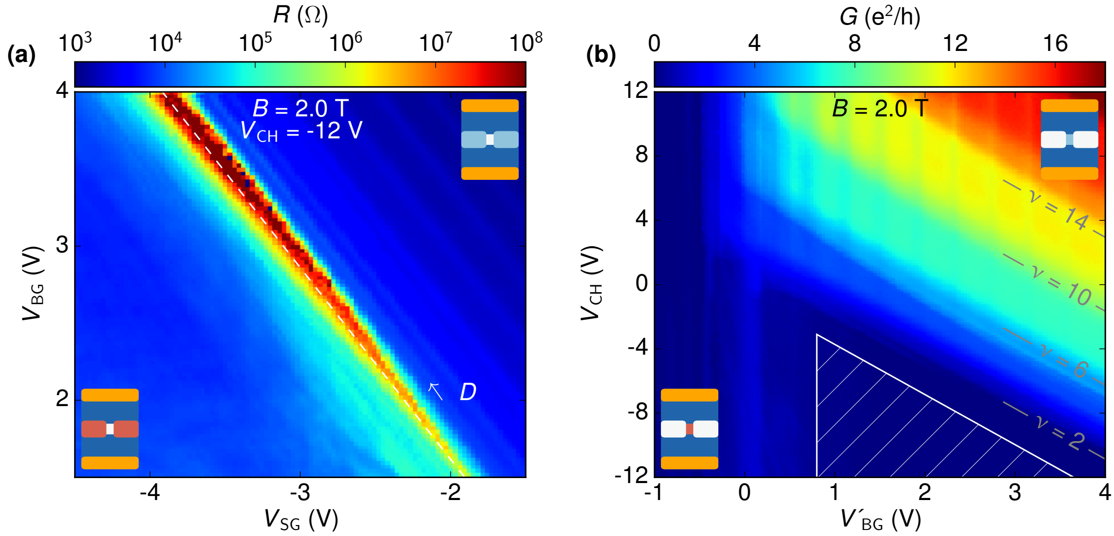

Figure 8.4: Sample characterization. (a) Resistance as a function of split gate and back gate voltage at $B = 2$ T. Along the diagonal line of high resistance, the Fermi level underneath the split gates and in the channel is in the band gap. The resistance in the gap is higher than 1000 h/e^2. (b) Conductance at $B = 2$ T as a function of channel gate voltage and back gate voltage. The split gate voltage is adjusted so as to keep the region under the split gates depleted (white dashed line in (a)). Conductance larger than e^2/h occurs when both the bulk and the channel are n-doped. Low conductance occurs when the bulk is n-doped and the channel is p-doped. Within the hatched area the edge channels inside the channel can form a quantum dot, as shown schematically in Fig. 8.1a.

the addition of an individual charge carrier to the confined area. The negative slope implies that an increase of the magnetic field leads to the removal of charge carriers from the dot. This trend can be understood as follows: when the magnetic field increases, the hole-like Landau levels shift down in energy. Since the Fermi level in the dot is pinned by the reservoirs, this leads to a decrease of the number of occupied states in the dot. In the case of Aharonov-Bohm interferometry, which typically requires larger dots [127], the opposite slope would be expected: an increase in magnetic field increases the flux through the interferometer, which has the same effect as increasing the area by applying a more negative gate voltage.

Charging lines of quantum dots in a magnetic field often show a slope related to a certain filling factor [129, 130]. The slope of the lines in Fig. 8.5b is close to a filling factor of four inside the channel, but the error bar on the density inside the channel does not allow for a quantitative comparison. To calculate the density, we extracted the capacitance between the conducting channel and the channel gate C_{CH} from a Landau fan measured in a previous cool down (see chapter 7) using a plate capacitor model. We also extract the same capacitance from several maps of the conductance at fixed magnetic field, such as Fig. 8.4b. The numbers we find are off by 30% and we therefore conclude that our estimates of charge carrier density and filling factor inside the channel have an error bar of 30%. Because of the vicinity of the split gates to the channel, it could be the case that C_{CH} depends on the split gate voltage. Moreover, C_{CH} might depend on the extent of the wave function inside the channel. These two factors are not accounted for in a simple capacitance model.

In Fig. 8.5c a line cut of Fig. 8.5a is shown. The spacing between the peaks is given by $\Delta V_{\mathrm{CH}} = 0.2$ V. For the addition of a single charge carrier, this corresponds to a capacitance between the dot and the channel gate of $C_{\mathrm{CH}} = e/\Delta V = 0.8$ aF, in rough agreement with the capacitance of $C_{\mathrm{CH}} = 1.3$ aF extracted using the gate voltage spacing of the Landau levels in Fig. 8.4b. For the latter estimate a dot area of $A = 0.02\ \mu\mathrm{m}^2$ (the lithographic size of the dot) was assumed. The significant background signal indicates that, apart from the channel exhibiting Coulomb blockade, there is another conductive channel through the dot. The conductive background decreases with increasing magnetic field (see Fig. 8.5a), but above $B = 3$ T the tunnel coupling to the reservoirs also gets weaker, because the distance between edge channels increases. Therefore we do not obtain a clearer signal at higher magnetic fields. The line cut shows a series of alternating low and high current peaks. This is reminiscent of the work on GaAs dots by Baer et al. [128], in which the pattern was explained by a different tunnel coupling to the reservoirs for the inner and outer edge channel present in the dot.

The conductance at $B = 2$ T as a function of density in the bulk n_{BG} and density in the channel n_{CH} (extracted from Fig. 8.4b) is shown in Fig. 8.5d. In Fig. 8.5e the same measurement is shown with a smoothened background subtracted. From the data it is apparent that the resonances (marked by dashed lines) are independent of the density in the bulk of the device and only depend on the density inside the dot for the entire range of the measurement. This is in agreement with our expectation, since the density in the bulk is much higher than the density in the dot. It also shows that the dot is clearly located inside the channel, making a disorder induced dot as in Ref. [94] highly unlikely.

Finite bias measurements were performed to determine the energy spacing of the levels in the quantum dot. The differential conductance as a function of dc bias and channel gate voltage (see Fig. 8.6) at $B = 2.33$ T shows pairs of Coulomb diamonds (see dotted red lines), with a charging energy on the order of 1 meV. By approximating the dot as a disk in an infinite medium with a self capacitance of $C = 8\epsilon\epsilon_0 r$, we can extract a radius of $r = 500$ nm. This is an upper bound for the dot radius, since the presence of closeby metal gates alters the capacitance of the dot significantly [9].

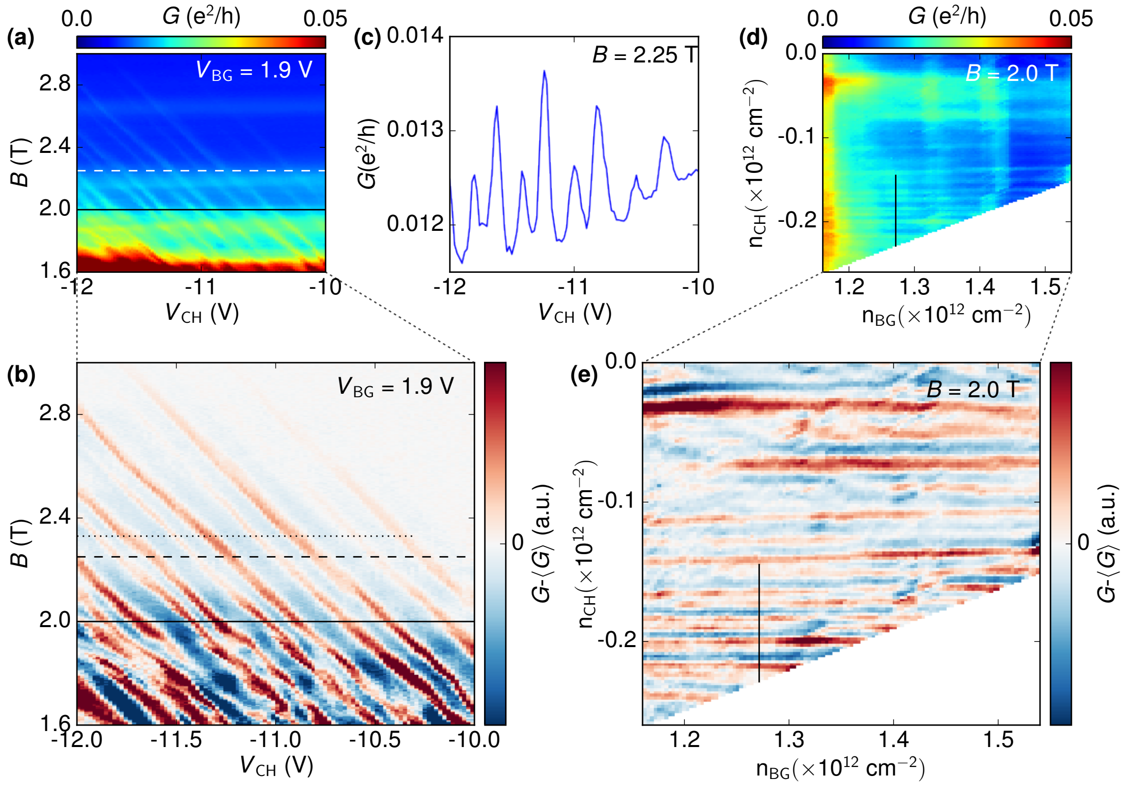

Figure 8.5: Magnetotransport through the device. (a) Conductance as a function of channel gate voltage and magnetic field. Peaks corresponding to charging of the quantum dot show up as diagonal lines. To enhance the visibility, we subtract a smoothened background (b). (c) Conductance at $B = 2.25$ T as a function of channel gate voltage (dashed line in (a),(b)), showing an alternating sequence of low and high peaks. (d) Conductance at $B = 2$ T as a function of the carrier density in the bulk and in the channel. (e) Same as (d) with a smoothened background subtracted. The solid line in (b) corresponds to the solid line in (d) and (e).

Figure 8.6: Bias spectroscopy. The differential conductance as a function of source drain bias and channel gate voltage measured at $B = 2.33$ T and $V_{BG} = 1.9$ V (dotted line in Fig. 8.5b). Pairs of Coulomb diamonds are visible, as indicated by the dotted red lines. They show an energy scale of roughly 1 meV.

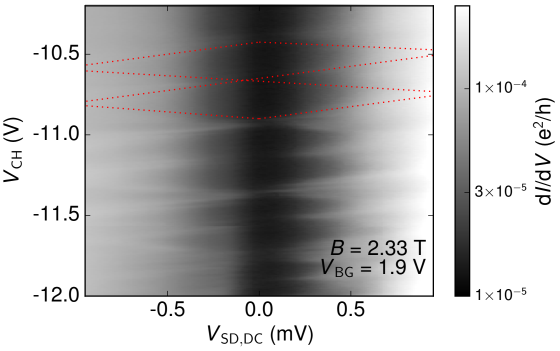

8.3 Conclusion

We realized an edge channel quantum dot in bilayer graphene making use of *p*-*n* interfaces. Around B = 2 T, the device shows Coulomb blockade. A scaled up version of the device discussed in this work could be used as an Aharanov-Bohm interferometer [127]. In the light of the recent observations of robust even denominator fractional quantum Hall states in bilayer graphene [131, 132], it could be an interesting geometry to study the statistics of the quasiparticles of these states [133].

Chapter 9

Conclusion and outlook

The goal of this thesis is the confinement of charge carriers in bilayer graphene. In this Chapter we summarize the experiments we performed to work towards this goal and provide an outlook on future experiments in this field.

9.1 Conclusion

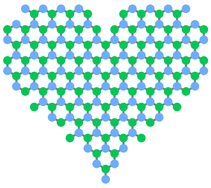

9.1: Graphene likes hBN

The first part of this project was devoted to the development of a fabrication process for high quality bilayer graphene devices. The encapsulation of bilayer graphene in hBN, pioneered by Dean et al. [26] and optimized by Wang et al. [27] has been essential for this project. Boron nitride provides a flat dielectric with few charged impurities and can withstand high gate voltages before the onset of leakage currents. On top of that, it protects graphene against contaminations during the lithography process. In Chapter 3 we developed a fabrication process for dual-gated bilayer graphene devices based on hBN encapsulation. The most important findings can be summarized as follows:

- We tried out different polymers for the stacking process. Best results have been obtained with freshly prepared PDMS and PC.
- Since bubbles of contaminants between the graphene and hBN tend to move (e.g. during spin-coating with resist), it turned out to be crucial to anneal the samples prior to

the lithography process. This reduces the mobility of the bubbles.

- Because of the extreme flatness of hBN, we found that roughening the surface before gate deposition is important. Otherwise the gates tend to shift or lift off.

- When adding additional dielectric layers after several lithography steps, Al_2O_3 deposited by atomic layer deposition is a suitable choice. The deposition process is reliable and high electric fields can be reached because of the large relative permittivity of Al_2O_3.

In Chapter 4 we assessed the quality of CVD grown bilayer graphene and found that, for the requirements of our project, the CVD graphene provided by the group of Prof. Ruoff could not yet compete with the exfoliated graphene. In the sample made with exfoliated graphene we could reproduce the results of Varlet et al., who reported on Fabry-Pérot oscillations [6] and a Lifshitz transition in bilayer graphene [7].

We then continued to study dual-gated encapsulated bilayer graphene devices. In Chapter 5 and Ref. [8] we found that these devices exhibit an oscillatory conductance in the *p*-*n* regime in intermediate magnetic fields. Ming-Hao Liu reproduced these oscillations in tight-binding simulations. The oscillatory conductance seems to be linked to the oscillatory density of states on both sides of the *p*-*n* interface, but the proposed model requires an eightfold degeneracy instead of a fourfold degeneracy to be in agreement with the periodicity observed in the experiment. Up to date it is not clear how to explain this eightfold degeneracy.

Although the dual-gated samples showed various interesting physical effects mentioned above, the maximal resistance usually stayed in the range of tens of kiloohms. This is not sufficient for the electrostatical definition of nanostructures. The incorporation of graphite back gates into the device geometry systematically led to induced resistances in the megaohm or even gigaohm regime, as discussed in Chapter 6 and Ref. [10]. Because of the vicinity to the graphene, these gates can screen charged impurities better than the previously employed Si back gates. The stray field pattern of these gates might also dif-

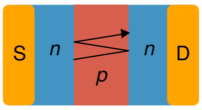

9.2: Fabry-Pérot cavity

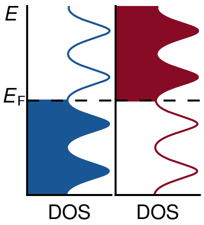

9.3: Modulated density of states

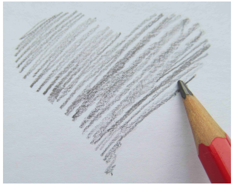

9.4: Graphene likes graphite too

fer, eliminating potential enhanced current flow along device edges [51].

The high resistance achieved in samples with a graphite back gate enabled us to define quantum point contacts in bilayer graphene. The observation of quantized conductance, with a complete pinch-off when depleting the structure, was discussed in Chapter 7. The step size of the quantized conductance plateaus is either 2 e^2/h or 4 e^2/h for six different QPCs. Several factors, such as the reduced transmission of the modes in one of the samples and the absence of conductance quantization in the p-doped regime, indicate that mesoscopic details play an important role. The samples showed an intricate pattern of level crossings in a magnetic field, which is yet to be understood.

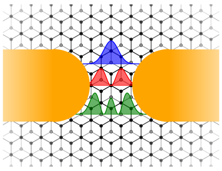

9.5: Quantum point contact

The same QPC device geometry was studied in a completely different regime in Chapter 8 and Ref. [11]. The sample was measured in the quantum Hall regime, where a p-doped central region was coupled to n-doped reservoirs. We observed Coulomb blockade at magnetic field values around B = 2 T, demonstrating that a quantum dot was formed. We thus realized our goal of confining charge carriers in bilayer graphene by electrostatic gating.

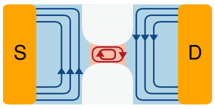

9.6: Edge channel quantum dot

9.2 Outlook

9.2.1 Further QPC studies

The level degeneracy of QPCs could be studied in a geometry proposed by Peter Rickhaus, see Fig. 9.7. In case of a (partially) valley polarized current exiting the QPC, the valley Hall effect [48, 49] would bend the trajectories of the charge carriers in an electric field (induced by the top gate in gray). The bending is opposite for the two valleys and therefore a valley polarization would result in a current imbalance between the top right and bottom right contact. Such a study could demonstrate that a QPC can be used as a source of valley polarized current.

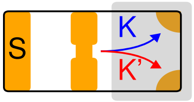

9.7: Valley Hall effect

The splitting and merging of QPC modes (see Section 7.5) in presence of a magnetic field is an open question at the moment. To answer this question one could make devices with QPCs under different angles with respect to the graphene lattice, to study the influence of this parameter. Another option would be to make a bilayer graphene QPC with a transition metal dicalchogenide as a dielectric layer. These materials induce enhanced spin-orbit interaction in graphene [134]. It would be informative to see if and how the pattern of level crosses changes with enhanced spin-orbit interaction. Finally, the effect of strain on QPCs could be investigated in samples with significantly differing thicknesses of the top hBN layer.

9.2.2 Scanning gate microscopy and other local imaging techniques

The QPC geometry proposed in this work will be investigated with scanning gate microscopy by Yongjin Lee and Carolin Gold. With this technique, the caustics of charge carriers eminating from the QPC can be studied. It will be interesting to see if patterns of branched electron (see Fig. 9.8[1]) flow occur and how they differ from those observed in GaAs [135, 136].

Luca Lorenzelli and Marius Palm from the Degen group aim to map out the local current density in graphene in the regime of viscous electron flow [137], using a scanning probe consisting of a diamond nanopillar with a single nitrogen-vacancy center [138]. The current density profile of etched QPCs [139] could be studied in the viscous flow regime, but electrostatically induced QPCs can provide tunability of the induced potential.

Another interesting topic would be the local current distribution of quantum Hall edge channels. In stacks of hBN and graphene the conductive layer is much closer to the surface than in most GaAs heterostructures, which is beneficial for the spatial resolution of local imaging techniques. Quantum Hall edge channels in graphene have already been studied with microwave impedance microscopy [140], albeit with limited resolution. A p-n junction with two back gates would be most interesting for such an experiment, since the spatial configuration of edge channels along abrupt edges of the graphene flakes might differ significantly from the configuration of edge channels along smooth p-n interfaces (see Fig. 9.9).

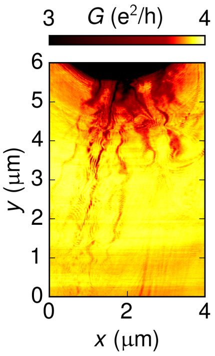

9.8: Branched electron flow in GaAs

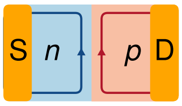

9.9: Edge channels in a p-n junction

---

[1] Image courtesy: Beat Bräm

9.2.3 Quantum dots at $B = 0$ T

Recent work in our group has demonstrated that the QPC geometry studied in Chapters 7 and 8 can also be used as a quantum dot at $B = 0$ T [104]. When decreasing the channel gate voltage beyond the depletion voltage, the region under the channel gate is tuned into the p-doped regime, while the bulk remains n-doped. The band structure at several positions along the transport direction is sketched in the inset of Fig. 9.10. The bulk of the sample and the region directly under the channel gate are separated by regions in which the Fermi level lies in the band gap, leading to the formation of tunnel barriers. The peaks of conductance shown in Fig. 9.10 correspond to individual charge carriers hopping onto the dot under the channel gate. Figure 9.11 shows the conductance of sample H as a function of channel gate voltage and source drain bias in a similar gate voltage regime. Coulomb diamonds are clearly visible. For $V_{\mathrm{CH}} > -10$ V no additional diamonds appear, indicating that the dot is depleted. We can therefore assign occupation numbers to the Coulomb diamonds.

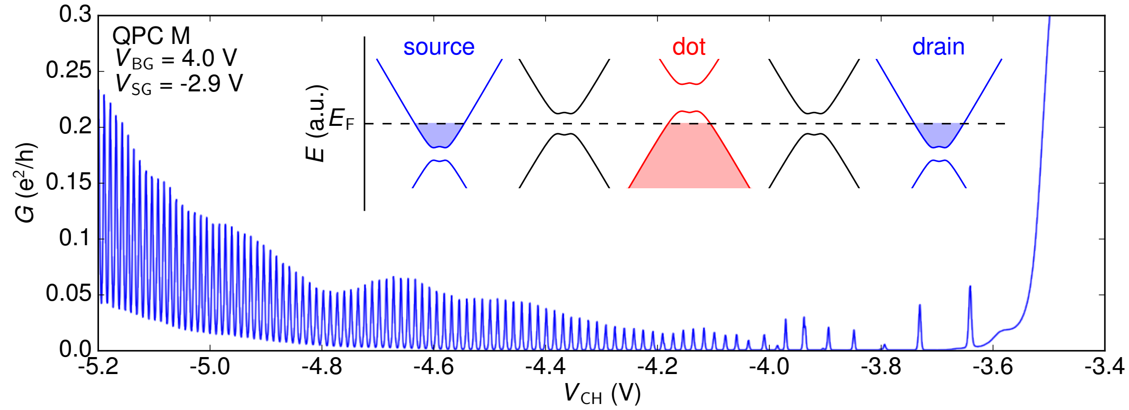

Figure 9.10: Conductance of QPC M as a function of channel gate voltage. The inset shows the band structure at various points along transport direction. Because of the positive back gate voltage and the negative channel gate voltage, the bulk of sample (labeled source and drain) is n-doped and the region under the channel gate is p-doped. Between these regions the Fermi level lies in the band gap, forming a tunnel barriers. The conductance peaks in the main figure correspond to individual charge carriers hopping onto the dot.

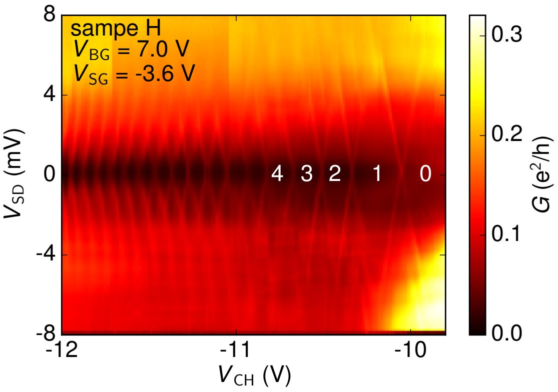

Figure 9.11: Coulomb diamonds observed in sample H. The numbers indicate the occupation of the quantum dot with charge carriers.

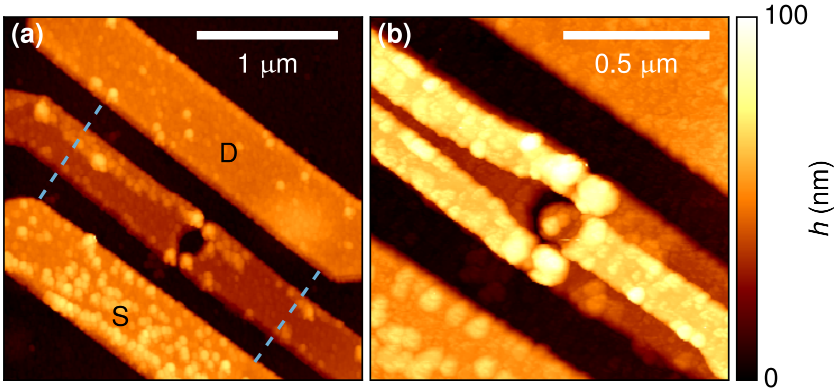

Figure 9.12: Atomic force microscopy images of a quantum dot structure prior to (a) and after (b) the deposition of the upper gate layer. The outer two gates on the upper layer tune the tunnel barriers, while the middle one is used to tune the levels in the quantum dot.

Future experiments on similar samples could involve coupling of multiple quantum dots and coupling of quantum dots of opposite polarity. Perhaps even laterally stacked quantum dots, bearing resemblance to the work of Bischoff et al. [141] could be revisited.

9.2.4 Dots with tunable tunnel barriers

In the quantum dots introduced in the previous paragraph the tunnel barriers between the dot and the reservoirs are formed by the regions of zero density which naturally occur at p-n interfaces in bilayer graphene. This simplifies the device geometry drastically, but has as a disadvantage that the tunneling rate cannot be tuned. We tried to make a dot with gates dedicated to the tuning of the tunnel barriers (see Fig. 9.12), but unfortunately one of the gates was not working. Similar device structures could be repeated in the future.

9.2.5 Counting electrons in graphene

In GaAs the combination of quantum dots and QPCs forms a versatile platform to study counting statistics [142], level degeneracies [143] and thermodynamics [144, 145] of charge carriers tunneling onto quantum dots. Annika Kurzmann will study these phenomena in bilayer graphene. The presence of both a spin and a valley degree of freedom might make the phenomenology even richer than in GaAs.

Fast pulsed measurements could be implemented to determine the spin coherence time of the charge carriers in the dots, similar to the work of Elzerman et al. [146] on GaAs quantum dots. Such measurements could quantify the hypothesis of long spin coherence times in graphene quantum dots [2].

9.2.6 Graphene quantum dots and microwave resonators

If spin states in graphene quantum dots indeed turn out to be long lived, these dots could be of use for quantum information processing applications. Coherent coupling of spin qubits to microwave photons has recently been demonstrated in Si [147, 148] and GaAs [149]. Graphene dots would offer the advantage of a larger lever arm between the dot and the gate, which leads to stronger coupling.

9.2.7 (F)QHE in nanostructures

As discussed in Chapter 8, the QPC geometry makes it possible to study copropagating edge channels which do not meet at a physical device edge. A similar device geometry was studied in Ref. [150]. A more detailed study of the quantum dot from Chapter 8 in different filling factor regimes could shed light on the potential presence of multiple dot-like Landau levels in the device, reminiscent of the work of Baer et al. [128]. A better control of the tunnel coupling, as proposed in Section 9.2.4, might be favorable for such studies.

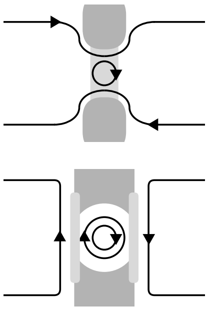

9.13: Top: edge channels in QPC. Bottom: edge channels in tunable dot

Another regime worth investigating would be the unipolar regime with higher density inside the dot region than in the bulk. Here a quantum dot might form as well, but the coupling to the bulk edge channels of the same polarity might be very different. In fact, the top right corner of Fig. 7.5a already exhibits an interesting pattern of oscillations in this regime. The differences between the QPC geometry and dots with tunable tunnel barriers could be studied in this regime as well (see Fig. 9.13).

Finally, it could be interesting to scale up the device geometry shown in Fig. 9.12. Similar structures in GaAs with a size on the order of 5 μm are dominated by Aharonov-Bohm interferences [127] and these might also occur in bilayer graphene. These interferometers are of particular interest to study the statistics of the quasi-particles of the fractional quantum Hall effect [133], which have recently been shown to exhibit large energy gaps in high quality bilayer graphene devices [131, 132].

9.2.8 Graphene nanostructures and 2D Lego bricks

In 2013 Geim and Grigorieva wrote a perspective article [151] on the combination of graphene with other 2D crystals into designer heterostructures, comparing the assembly process to building with Lego. With the electrostatic definition of nanostructures in bilayer graphene, we can now think of tailoring these structures with other 2D materials as well. As already mentioned in Section 9.2.1, enhanced spin orbit interaction in graphene QPCs could be studied by adding a transition metal dichalcogenide as a substrate for the graphene. A quantum dot with a nearby ferromagnet could be realized by incorporating CrI_3 [152] in a van der Waals heterostructure. Hybrid superconductor-quantum dot devices [153] could be studied in graphene by combining quantum dots with a superconducting 2D material such as $NbSe_2$ [154]. In conclusion, the atomic scale Lego, consisting of the vast spectrum of 2D materials combined with the powerful van der Waals stacking technique, provides countless exciting opportunities on the nanoscale.

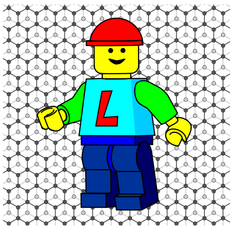

9.14: Everything is awesome when you work on graphene

Publications

Spin and Valley States in Gate-defined Bilayer Graphene Quantum Dots
Marius Eich, František Herman, Riccardo Pisoni, Hiske Overweg, Yongjin Lee, Peter Rickhaus, Kenji Watanabe, Takashi Taniguchi, Manfred Sigrist, Thomas Ihn, Klaus Ensslin
Physical Review X **8**, 031023 (2018)

Transport through a network of topological states in twisted bilayer graphene
Peter Rickhaus, John Wallbank, Sergey Slizovskiy, Riccardo Pisoni, Hiske Overweg, Yongjin Lee, Marius Eich, Ming-Hao Liu, K Watanabe, T Taniguchi, Vladimir Fal'ko, Thomas Ihn, Klaus Ensslin
ArXiv preprint 1802.07317 (2018)

Gate-tunable quantum dot in a high quality single layer MoS_2 van der Waals heterostructure
Riccardo Pisoni, Zijin Lei, Patrick Back, Marius Eich, Hiske Overweg, Yongjin Lee, Kenji Watanabe, Takashi Taniguchi, Thomas Ihn, Klaus Ensslin
Applied Physics Letters **112**, 123101 (2018)

Edge channel confinement in a bilayer graphene *n-p-n* quantum dot
Hiske Overweg, Peter Rickhaus, Marius Eich, Yongjin Lee, Riccardo Pisoni, Thomas Ihn, Klaus Ensslin
New Journal of Physics **20**, 013013 (2018)

Electrostatically induced quantum point contacts in bilayer graphene
Hiske Overweg, Hannah Eggimann, Xi Chen, Sergey Slizovskiy, Marius Eich, Pauline Simonet, Riccardo Pisoni, Yongjin Lee, Kenji Watanabe, Takashi Taniguchi, Vladimir Fal'ko, Klaus Ensslin, Thomas Ihn
Nano Letters **18**, 553-559 (2018)

Gate-Defined One-Dimensional Channel and Broken Symmetry States in MoS2 van der Waals Heterostructures
Riccardo Pisoni, Yongjin Lee, Hiske Overweg, Marius Eich, Pauline Simonet, Kenji Watanabe, Takashi Taniguchi, Roman Gorbachev, Thomas Ihn, Klaus Ensslin
Nano Letters **17**, 5008-5011 (2017)

Oscillating magnetoresistance in graphene p-n junctions at intermediate magnetic fields
Hiske Overweg, Hannah Eggimann, Ming-Hao Liu, Anastasia Varlet, Marius Eich, Pauline Simonet, Yongjin Lee, Kenji Watanabe, Takashi Taniguchi, Klaus Richter, Vladimir Fal'ko, Klaus Ensslin, Thomas Ihn
Nano Letters **17**, 2852–2857 (2017)

Anomalous Coulomb drag between bilayer graphene and a GaAs electron gas
Pauline Simonet, Szymon Hennel, Hiske Overweg, Marius Eich, Riccardo Pisoni, Yongjin Lee, Peter Märki, Mattias Beck, Jérôme Faist, Thomas Ihn, Klaus Ensslin
New Journal of Physics **19**, 103042 (2017)

Graphene nano-heterostructures for quantum devices
Dominik Bischoff, Marius Eich, Anastasia Varlet, Pauline Simonet, Hiske Overweg, Klaus Ensslin, Thomas Ihn
Materials Today **19**, 375 (2016)

Nonequilibrium transport in density-modulated phases of the second Landau level
Stephan Baer, Clemens Rössler, Szymon Hennel, Hiske Overweg, Thomas Ihn, Klaus Ensslin, Christian Reichl, Werner Wegscheider
Physical Review B **91**, 195414 (2015)

Localized charge carriers in graphene nanodevices
Dominik Bischoff, Anastasia Varlet, Pauline Simonet, Marius Eich, Hiske Overweg, Thomas Ihn, Klaus Ensslin
Applied Physics Reviews **2**, 031301 (2015)

The importance of edges in reactive ion etched graphene nanodevices
Dominik Bischoff, Pauline Simonet, Anastasia Varlet, Hiske Overweg, Marius Eich, Thomas Ihn, Klaus Ensslin
Physica Status Solidi RRL **10**, 68 (2015)

Appendices

A Sample names

The sample names used in this thesis are different from the ones used in the fabrication process and Refs. [8, 10, 11]. Table A.1 lists all the sample names.

thesis	**fabrication**	**Ref.** [8]	**Ref.** [10]	**Ref.** [11]
A	Anastasia Tr23	A	-	-
B	stack 17	B	-	-
C	stack 15	C	-	-
D	stack 22	D	-	-
E	stack 21	E	A	sample
F	stack 22	F	-	-
G	stack 16	-	-	-
H	stack 26	-	B	-
I	stack P1	-	-	-

Table A.1: Sample names

B Details of the tight-binding simulations on magnetoresistance oscillations in p-n junctions

This appendix discusses the simulations employed by Ming-Hao Liu to describe the magnetoresistance oscillations in Chapter 5.

Input parameters for the tight-binding model

The employed tight-binding model consists of a scaled version of the hexagonal graphene lattice [98] which takes into account the spatially varying on-site energy $V(x)$ induced by the gates.

$$H = -t \sum_{<i,j>} c_i^\dagger c_j + \sum_j V(x_j) c_j^\dagger c_j \tag{B.1}$$

The on-site energy $V(x)$ can be calculated from the charge carrier density profile $n(x)$. The charge carrier density induced by the gates is approximated as a simple hyperbolic tangent function with smoothness 50 nm. For single layer graphene in absence of a magnetic field the on-site energy is hence given by:

$$V(x) = -\hbar v_\mathrm{F} k_\mathrm{F}(x) \,\mathrm{sgn}(n(x)) = -\hbar v_\mathrm{F} \sqrt{\pi |n(x)|} \,\mathrm{sgn}(n(x)) \tag{B.2}$$

In the Shubnikov - de Haas regime, we approximate the density of states by:

$$D(E) = \frac{4eB}{h} \sum_{N=-\infty}^{\infty} \frac{\Gamma}{\pi} \frac{1}{(E - E_j)^2 + \Gamma^2} \tag{B.3}$$

where

$$E_N = \mathrm{sgn}(N) * \sqrt{2eB\hbar v_\mathrm{F}^2 |N|} \tag{B.4}$$

is the energy of the jth Landau level in monolayer graphene with $N = \nu/4$ the Landau level index. Using these equations we can calculate $n(E) = \int_E^0 D(E')dE'$. This relation can than be inverted (numerically) to determine the on-site energy as a function of the spatially varying charge carrier density.

Once the full Hamiltonian has been calculated, the transmission from source to drain can be determined using a Green's function formalism as described in Refs. [155, 156].

Overview

In chapter 5 we have shown a transmission map as a function of left and right carrier density, calculated as described in the previous section. The considered graphene ribbon of width $W = 1$ μm is subject to a model density function describing an ideal p-n junction with smoothness 50 nm. The full map is repeated here in Fig. B.1(a), with a white box marking the region plotted in Fig. B.1(b).

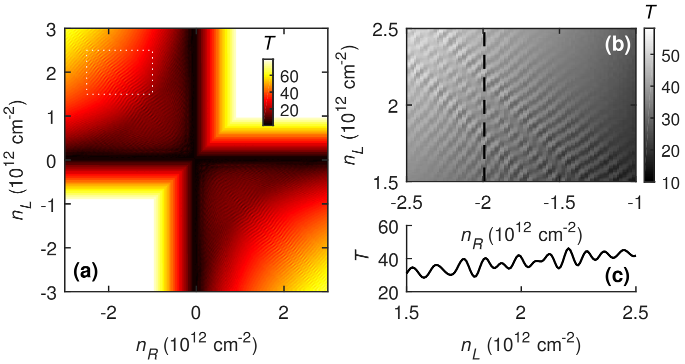

Figure B.1: (a) Transmission map $T(n_R, n_L)$, same as Fig. 5(a) in the main text (smoothness 50 nm and graphene width $W = 1$ μm); white dashed box marks the region shown in (b), where a black dashed line indicates the line cut of $T(n_L)$ at fixed $n_R \approx -2 \times 10^{12}$ cm^{-2} shown in (c).

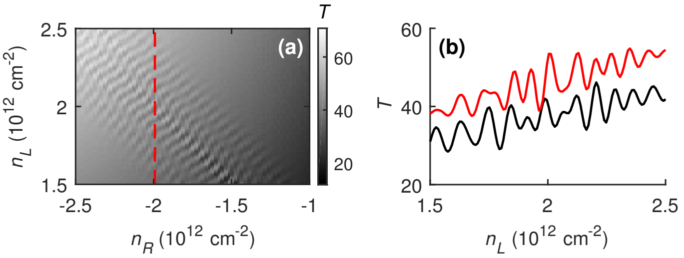

Figure B.2: (a) Transmission map $T(n_R, n_L)$, similar to Fig. B.1(b) but with smoothness 25 nm of the p-n junction. The red dashed line indicates the line cut shown as a red line in (b), where the black line is the reference line identical to Fig. B.1(c) for the case with smoothness 50 nm.

In the following, we show more numerical results in order to demonstrate that the observed oscillation is independent of the smoothness of the p-n junction and the width of the graphene ribbon, and is not related the current along the p-n junction. Instead, the oscillation is shown by the last numerical test to be closely related to the Landau levels away from the p-n junction.

For quantitative and systematic comparisons, we will focus on the density range shown in Fig. B.1(b) and the line cut on it along the dashed line shown in Fig. B.1(c). All calculations shown in the following consider the same density range and resolution as Figs. B.1(b) and (c), which can be regarded as the reference panels of this appendix. In particular, the line cut of Fig. B.1(c) will be repeatedly shown in the following results.

Smoothness dependence

Figure B.2(a) presents the transmission map with smoothness of 25 nm, showing a similar pattern seen in Fig. B.1(b) where the junction smoothness is 50 nm. A more quantitative comparison is shown in Fig. B.2(b) for the line cuts of the two cases. Despite a slightly higher T obtained for the sharper junction due to the Klein collimation [157], i.e., the sharper the p-n junction, the wider the finite transmission probability of the angle distribution and hence the conductance, the general trend

Figure B.3: Transmission maps $T(n_R, n_L)$ similar to Fig. B.1(b) with the same smoothness of 50 nm but with (a) $W = 0.9\ \mu$m and (b) $W = 0.8\ \mu$m. Line cuts along the red/blue dashed line marked in (a)/(b) are compared in (c) together with the reference line (black) of Fig. B.1(c) for the case of $W = 1\ \mu$m.

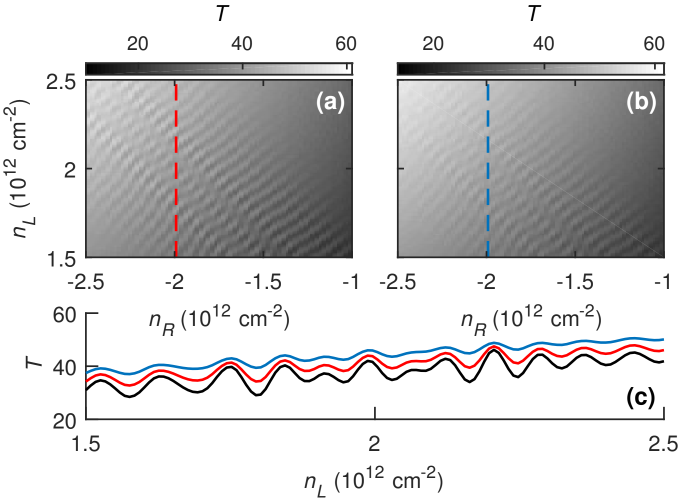

of the oscillation is shown to be independent of the smoothness.
In the rest of the numerical results, the smoothness will be fixed to 50 nm.

Width dependence

Figure B.3 presents the transmission map based on a graphene ribbon with $W = 0.9\ \mu$m shown in its panel (a) and $W = 0.8\ \mu$m shown in its panel (b). Comparing the line cuts in Fig. B.3(c), along with the reference line of Fig. B.1(c) for the case of $W = 1\ \mu$m, the feature of the oscillation is clearly shown to be width-independent. On the other hand, the oscillation amplitude decreasing with the reduced graphene width implies that the oscillation may be closely related to the Landau levels in the bulk away from the p-n junction, since the wider the graphene ribbon the better the Landau levels can develop.
In the rest of the numerical results, the graphene width will be fixed as $W = 1\ \mu$m.

Strong lattice defects

Next we show that the oscillation is not related to the current along the p-n junction. To this end, we consider large-area lattice defects located in the vicinity of the p-n junction. The basic idea is that if the oscillation came from any interference due to the current along the p-n junction, such as the snake state [102], a large-area lattice defect at the p-n interface or in the vicinity of it would act as a strong scatterer, destroying the interference and hence suppressing the oscillation. Contrarily, if the oscillation survives the introduced large defects, the current along the p-n junction will then be ruled out from possible origins of the oscillation.
We first consider a 50×400 nm^2 defect in Figs. B.4(a) and (b); the defect is placed in front of the p-n junction (at a distance 150 nm) in the former, and exactly on the p-n junction in the latter. Despite an additional modulating pattern observed in Fig. B.4(a), the fine oscillation patterns remain visible in both cases. By increasing

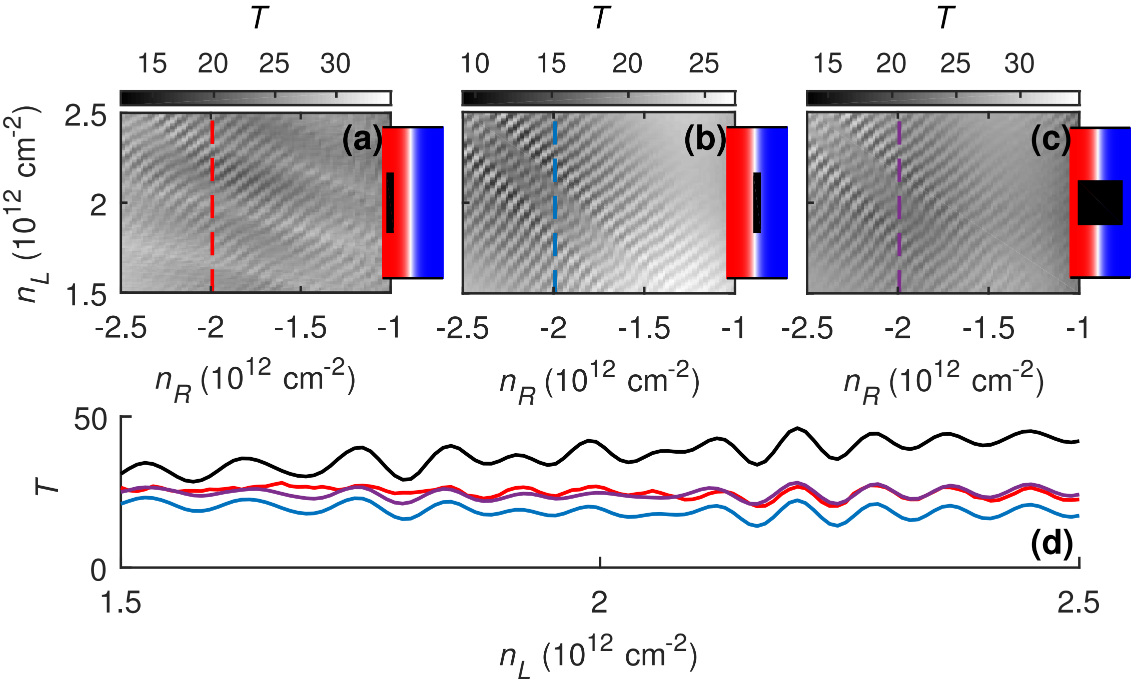

Figure B.4: (a)–(c) Transmission maps $T(n_R, n_L)$ similar to Fig. B.1(b) with the same smoothness of 50 nm and width $W = 1$ μm, but with a large-area defect represented by the black rectangle shown in the individual inset to the right of each panel, where the color background depicts the y-independent model function $n(x, y)$ describing the density variation of the p-n junction. The size of the defect is 50×400 nm^2 in (a,b) and 300×300 nm^2 in (c). Line cuts along the red/blue/purple dashed line marked in (a)/(b)/(c) are compared in (d) together with the reference line (black) of Fig. B.1(c) for the case without the defect.

the defect area to 300×300 nm^2, the transmission map shown in Fig. B.4(c) still exhibits the same oscillation pattern. A quantitative comparison of the line cuts summarized in Fig. B.4(d) together with the reference line from Fig. B.1(c) clearly shows that the oscillations observed in Figs. B.4(a)–(c) belong to the same type as all those shown previously.

The fact that the strong defect introduced in the vicinity of the p-n junction cannot suppress the oscillation clearly indicates that any possible interference effect due to the current along the p-n junction cannot be the origin causing the oscillation. Instead, the oscillation seems to depend only on the Landau levels that are well developed in the semi-infinite leads.

Fixed leads

So far, all the presented calculations are based on an infinite graphene ribbon with a p-n junction in the middle, as described in the main text. Technically, this is

Figure B.5: (a) Transmission map $T(n_R, n_L)$ with the same range and parameters considered in Fig. B.1(b) but with the two leads fixed at energy $E = 0.1$ eV. The red dashed line indicates the line cut shown as a red line in (b), where the black line is the reference line identical to Fig. B.1(c) for the case with floating leads.

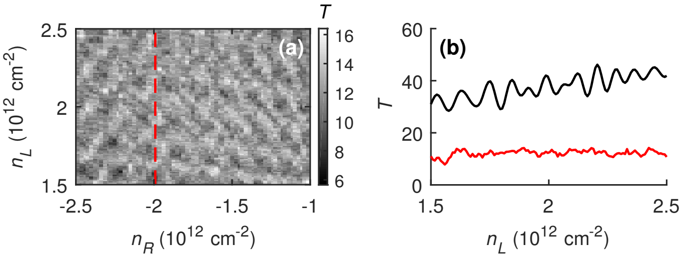

achieved in numerics by considering a scattering region of size $L \times W$ attached to two leads from the left and right, both floating with the density profiles at the attaching edge of the scattering region. As long as L is much longer than the smoothness of p-n junction ($L = 400$ nm has been adopted in all the presented calculations), the density values at the left and right edges of the scattering region will saturate to a constant, and the entire open quantum system of the finite-size scattering region attached to the two floating semi-infinite leads will resemble an ideal p-n junction in the middle of an infinitely long graphene ribbon, exhibiting an L-independent transmission behavior.

As a final and conclusive numerical test, we now fix the Fermi energies in the two semi-infinite leads at 0.1 eV, and consider the same range and parameters as the reference panel of Fig. B.1(b). The calculated transmission map is shown in Fig. B.5(a), which no longer exhibits the fine oscillation. The line cuts of fixed leads vs. floating leads compared in Fig. B.5(b) clearly show that the oscillation completely vanishes in the present case of fixed leads.

The vanishing oscillation is consistent with what we have speculated from the previously shown tests that the oscillation originates from the resonance between Landau levels well developed in the far left and far right in the semi-infinite leads. The present case shown in Fig. B.5 considers fixed Fermi energies in the leads that no longer float with the densities n_R and n_L. Together with the fact that the length $L = 400$ nm $\ll W$ of the scattering region is too short for the Landau levels to form, the vanishing oscillation is therefore reasonably expected. By increasing the length of the scattering region to at least $L \approx W$, revival of the oscillation is expected for the case of fixed leads.

Note that the situation of fixed leads is actually closer to the experiment, because the densities in graphene regions close to the contacts are rather pinned by the contact doping. However, the samples in our experiments (summarized in Table I in the main text) are long enough (several microns in all samples) for the Landau levels to develop well (with level spacing not far enough compared to disorder broadening in the magnetic field range we focus on) due to their cleanness and therefore exhibit the oscillation. Our numerical results based on floating leads correspond to the ideal case of infinitely long samples and therefore exhibit optimized oscillation.

C Details of the toy model for magnetoresistance oscillations in p-n junctions

Definition of the toy model

The density of states in the Shubnikov - de Haas regime can be approximated by Eq. B.3. Figure C.1 shows this density of states as a function of energy around the 50th Landau level ($E_\mathrm{F} = E_{50}$) for $B = 0.5$ T and $\Gamma = 0.3$ meV. The derivative of the Fermi-Dirac distribution at two different temperatures is also indicated.

We would like to find a measure for the overlap of the density of states on two sides of a pn junction. Assuming that only the density of states close to the Fermi energy matters, we define this overlap as:

$$O(\Gamma, B, T) = \int_{-\infty}^{\infty} -\frac{\partial f(\Gamma, B, T)}{\partial E} D(E - E_L) D(E - E_R) dE \tag{C.1}$$

where E_L and E_R are the energies of the highest occupied Landau level at the left and the right side of the pn interface. A similar expression is derived in a more rigorous way for weakly tunnel coupled 2DEGs in Ref. [14].

We numerically calculate this integral for different filling factors on the left and the right side of the interface. When we plug in a temperature of T = 10 K (window around E_F can be seen in Fig. C.1), we find the pattern shown in Fig. C.2. It resembles the experimentally observed pattern, except that the periodicity is off by a factor of two (gray lines indicate measured periodicity). When putting in a lower temperature (T = 2 K, probing only density of states very close to E_F), we obtain a checkerboard pattern, shown in Fig. C.3 (as can be expected with a small integration window around the Fermi energy).

The measured periodicity of the oscillations can be obtained by assuming that even (odd) Landau levels couple well to even (odd) Landau levels, and even and odd Landau levels do not couple. In the model this can be introduced by considering

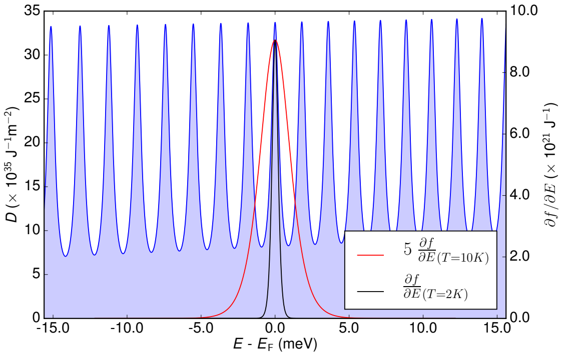

Figure C.1: Density of states as a function of energy when the Fermi level is positioned at the 50th Landau level. The derivative of the Fermi-Dirac distribution is also indicated.

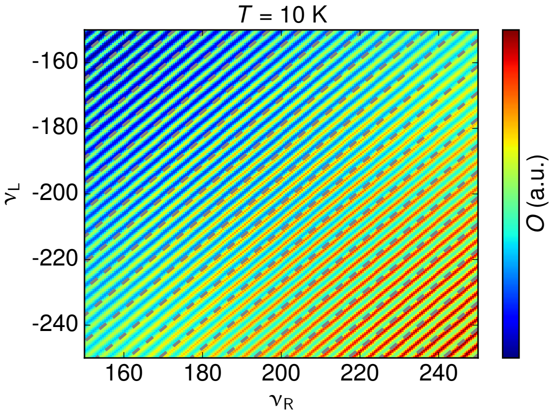

Figure C.2: Numerically calculated overlap (see Eq. C.1) as a function of ν_L and ν_R for T = 10 K, B = 0.5 T and $\Gamma = 0.3$ meV. The pattern shows the same slope as the experimentally observed magnetoresistance oscillations (gray dashed lines), but the periodicity is off by a factor two.

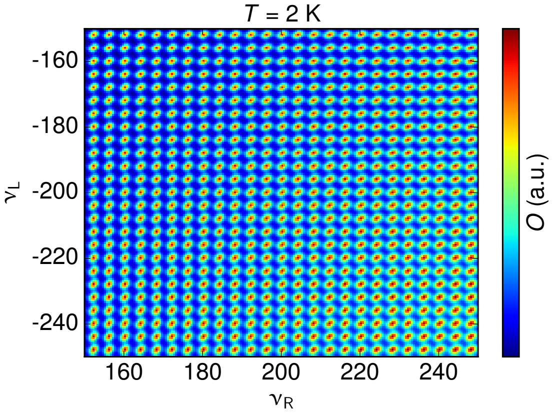

Figure C.3: Numerically calculated overlap (see Eq. C.1) as a function of ν_L and ν_R for T = 2 K, B = 0.5 T and Γ = 0.3 meV. The pattern is different from the experimentally observed oscillations.

the following density of states:

$$D(E) = \frac{4eB}{h} \sum_{N=-\infty}^{\infty} (-1)^N \frac{\Gamma}{\pi} \frac{1}{(E - E_N)^2 + \Gamma^2} \tag{C.2}$$

The resulting overlap is shown in Fig. C.4. Although this model describes the same pattern as the measured oscillations, the following questions remain:

- What mechanism would justify the artificially introduced parity?
- Is there a reason to use the derivative of the Fermi-Dirac distribution at higher temperature?
- Is it justified to use Eq. C.1, which describes tunneling in weakly coupled 2DEGs?

Oscillations with a different slope

A last interesting observation is that the toy model and the tight-binding simulations both show oscillations with a different slope in the regime where one of the filling

Figure C.4: Numerically calculated overlap (see Eq. C.2) as a function of ν_{L} and ν_{R} for $T = 2$ K, $B = 0.5$ T and $\Gamma = 0.3$ meV. The pattern shows the same slope as the experimentally observed magnetoresistance oscillations (gray dashed lines), and the periodicity is in agreement as well.

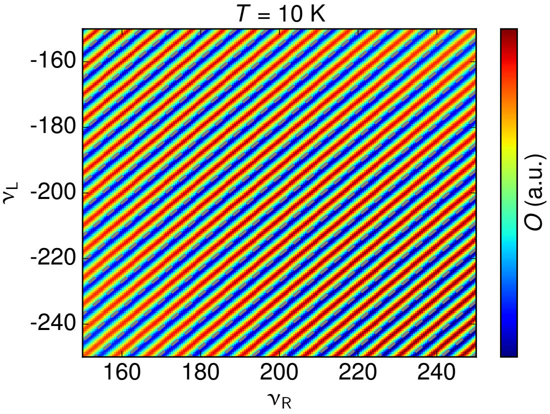

factors is significantly lower than the other ($\nu_{\mathrm{R}} \sim -20$,$\nu_{\mathrm{L}} \sim 160$). In this regime, the peaks in the density of states as a function of energy are roughly thrice as widely spaced for the right side of the interface, because the spacing goes with $\sqrt{N} - \sqrt{N-1}$. Therefore the overlap of the density of states stays unchanged when following a line along which $\Delta\nu_{\mathrm{L}} = 3\Delta nu_{\mathrm{R}}$. This is indeed the slope of the observed lines in the toy model (see Fig. C.5).

For bilayer graphene the energy of the Landau levels is given by

$$E_N = \mathrm{sgn}(N) * \hbar\omega_c\sqrt{|N||N-1|)} \tag{C.3}$$

with ω_c the cyclotron radius. The spacing in energy is therefore closer to a constant spacing than in monolayer graphene. When employing the toy model for bilayer graphene, we find that there are no oscillations with a different slope showing up, as expected.

The models therefore predict that in monolayer graphene samples oscillations with a different slope can occur, but not in bilayer graphene. An experimental verification of this prediction would be a strong indication that the density of states modulations indeed cause the observed oscillations. Unfortunately the observation of the oscillations with a different slope is challenging, since they occur when one side of the *p*-*n* junction is at very low density. These oscillations will only be visible in samples with a very low disorder density. So far they have not yet been observed.

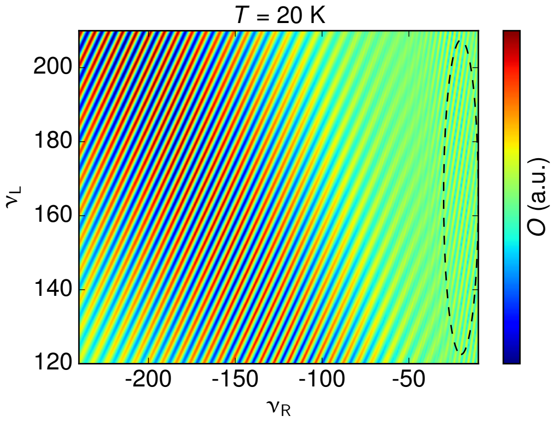

Figure C.5: Numerically calculated overlap. When one filling factor is significantly lower than the other, a set of lines with a different slope can be observed, which is encircled by the dashed ellipse.

D Magnetoresistance oscillations in samples B-F

Here we present measurements of the magnetoresistance oscillations discussed in Chapter 5 in additional samples. Figures D.1-D.5 show magnetoresistance oscillations of samples B-F, which look similar to the ones observed in sample A (see Fig. 5.3, Chapter 5). The periodicity of the oscillations is the same for all samples.

4-terminal measurements in sample D

The device layout of sample D is schematically shown in Fig. D.6. A DC voltage of $100mV$ was applied to the sample with a $R = 10$ MΩ resistor in series. This led to a constant current of $I = 10$ nA flowing from contact 1 to contact 4. The voltage drop between contact pairs (1,2), (2,3) and (3,4) where measured. To calculate the conductance a contact resistance was subtracted where appropriate. As is shown in Fig. D.6b-d, the oscillatory magnetoresistance is only observed when a p-n interface is present (i.e. in between contacts (2,3)).

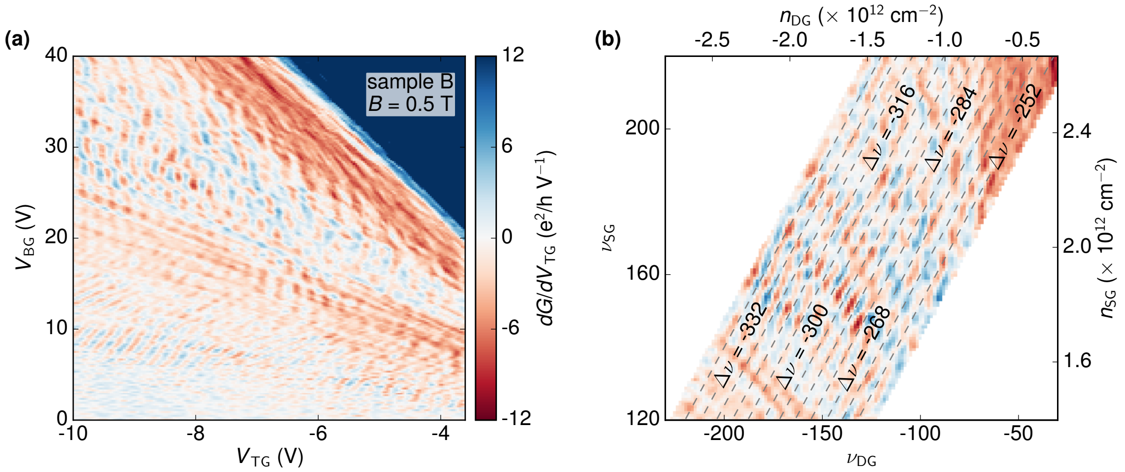

Figure D.1: (a) Transconductance dG/dV_{TG} of sample B at $B = 0.5$ T. (b) Transconductance as a function of filling factor in the single and double gated region.

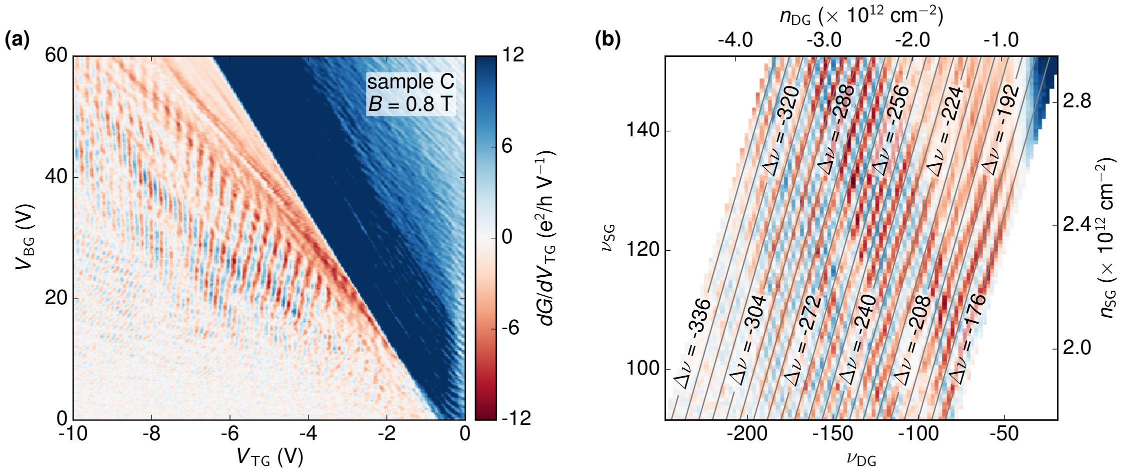

Figure D.2: a) Transconductance dG/dV_{TG} of sample C at $B = 0.8$ T. (b) Transconductance as a function of filling factor in the single and double gated region.

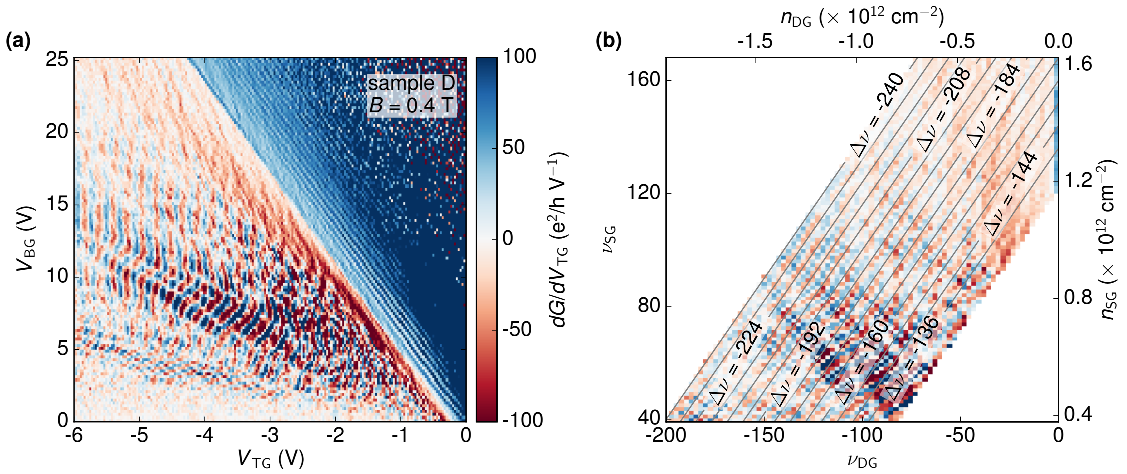

Figure D.3: (a) Transconductance dG/dV_{TG} of sample D at $B = 0.4$ T. (b) Transconductance as a function of filling factor in the single and double gated region.

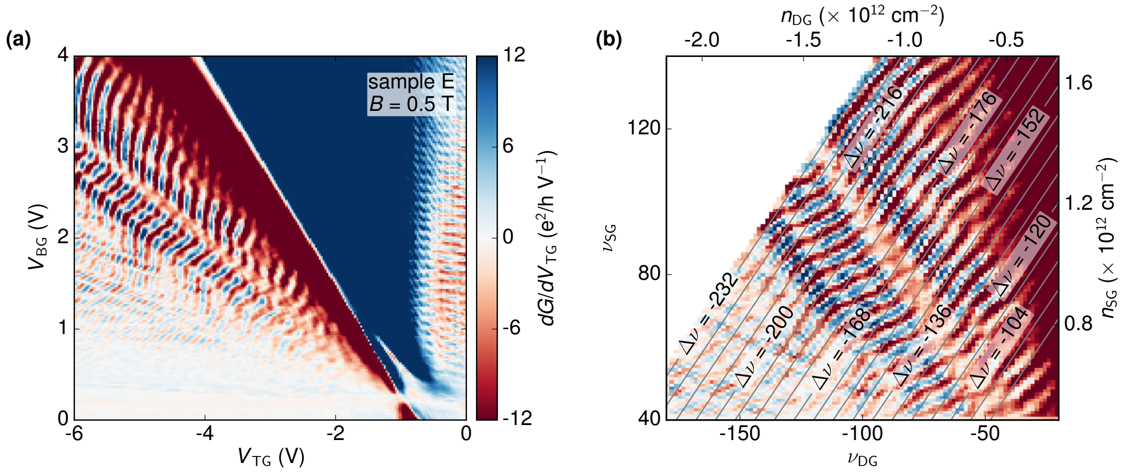

Figure D.4: (a) Transconductance dG/dV_{TG} of sample E at $B = 0.5$ T. (b) Transconductance as a function of filling factor in the single and double gated region.

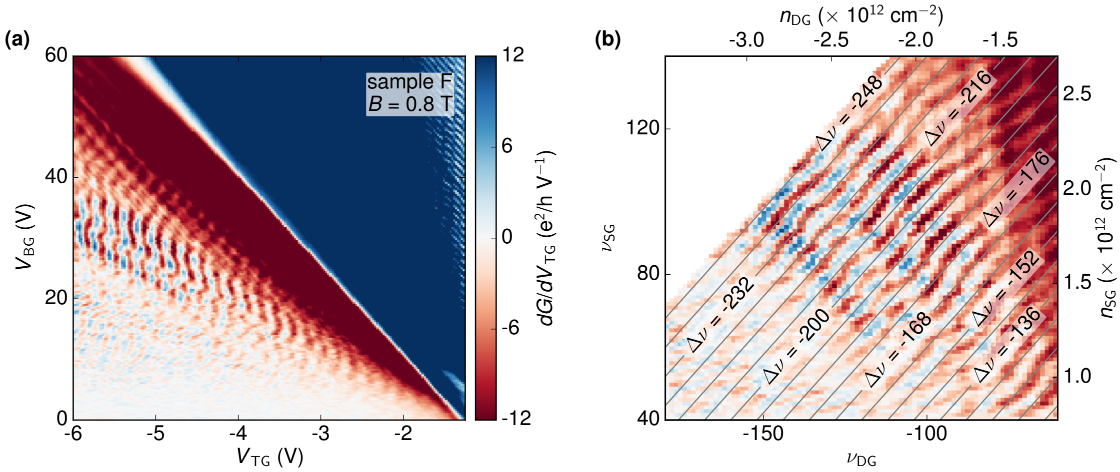

Figure D.5: (a) Transconductance dG/dV_{TG} of sample F at $B = 0.8$ T. (b) Transconductance as a function of filling factor in the single and double gated region.

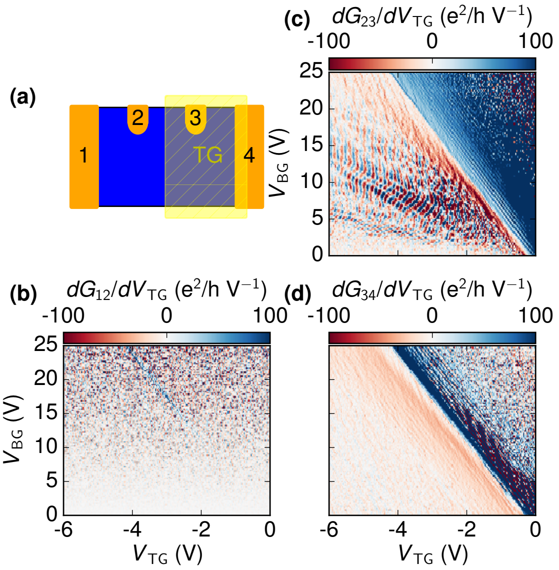

Figure D.6: (a) Schematic drawing of sample D. Contacts are labelled 1-4. (b) Transconductance between contacts (1,2) at $B = 0.4$ T. (c) Transconductance between contacts (2,3) showing an oscillatory pattern in the *p*-*n* regime. (d) Transconductance between contacts (3,4).

E Fabrication details of QPC samples

The geometry and mobility of the QPC samples can be found in Table E.1.

For the etching of the contacts, we use a recipe adapted from Ref. [27]. We use a reactive ion etcher (Oxford Instruments RIE 80 Plus), with a mixture of CHF_3 gas (40 sccm) and O_2 (4 sccm). With an RF power of 60 W, the obtained etch rate of hBN is 45 nm/min. We carefully choose an etching time for each individual sample to make sure that the hBN is etched sufficiently for the contacts to reach the graphene layer, but not too far, since this would lead to a short between the contacts and the graphite back gate.

The deposition of Al_2O_3 was done in an atomic layer deposition system (Picosun Sunale R-150B) at a temperature of 150 °C with trimethylaluminum (TMA) and water as precursor gases.

For sample E we performed temperature dependent measurements of the resistance maximum for (V_{TG},V_{BG}) = -3.9, 4 V, corresponding to a displacement field of 0.35 V/nm, and (V_{TG},V_{BG}) = -1.7, 2 V, corresponding to a displacement field of 0.2 V/nm. The respective gap sizes were 55 meV and 16 meV. An indirect measure of the gap size is the resistance at charge neutrality. Figure E.1a shows the resistance of sample A along several line cuts in Fig. 2a. The resistance at the charge neutrality point increases by orders of magnitude when a band gap is opened. The measurement was performed with a bias voltage of $V = 50\ \mu$V. The data for the highest displacement field (V_{BG} = 4 V) has been omitted, because the high resistance peak cannot be reliably measured with a small bias voltage. Similar data for sample H is shown in Fig. E.1b.

	sample E	sample H	sample I
graphite thickness (nm)	28	15	7
bottom BN thickness (nm)	38	53	24
top BN thickness (nm)	35	25	20
Al_2O_3 thickness (nm)	60	30	30
SG height (nm)	60	20	20
channel width (nm)	100	80	50/80/180
channel gate width (nm)	200	60	200
mobility (cm^2/Vs)	8×10^4	6×10^4	8×10^4

Table E.1: Characteristics of samples E, H and I

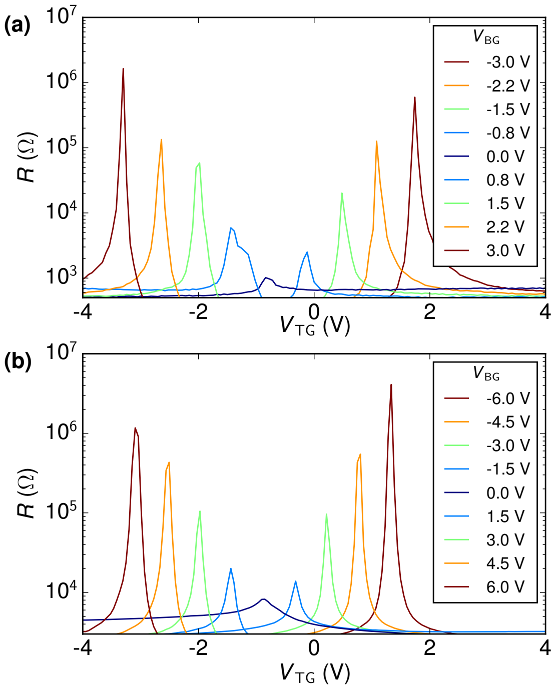

Figure E.1: (a) Resistance of sample E as a function of top gate voltage for several back gate voltages. The resistance at the charge neutrality point increases by orders of magnitude when a band gap is opened. (b) Same for sample H

F Simulation of the electrostatic potential in QPC samples

To get more insight in the electrostatic potential of the quantum point contact, we use a finite element simulator (COMSOL). The charge carrier sheet density $n(\vec{r})$ and the potential $V(\vec{r})$ are calculated self-consistently using Poisson's equation and the Thomas-Fermi approximation. The density of states is approximated by $D(E) = m^*/(\pi\hbar^2)\theta(E)$ with $m^* = 0.034m_e$ and θ the Heavyside step function, which limits the model to transport in the conduction band. We do not take the Mexican hat shape of the bilayer graphene band structure and the position dependent band gap into account. The quantization of states inside the one-dimensional channel, due to the lateral confinement, is also neglected.

Geometry

The geometry considered for the simulation is the same as for sample E (see main text and table 5.1). From AFM images of sample E it is apparent that the channel gate drops partially into the opening between the split gates. We therefore modelled the channel gate with an elliptical extension above the channel region (see Fig. F.1). The width of this extension was 150 nm and the depth 30 nm, in agreement with the AFM images. When omitting the extension from the simulation, the channel gets depleted around $V_{\mathrm{CH}} = -25$ V instead of the experimentally observed $V_{\mathrm{CH}} = -12$ V. With the extension the channel gets depleted close to the experimentally observed

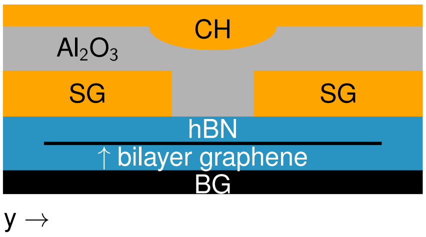

Figure F.1: Cross section of the sample used for Comsol simulation. The channel gate has an elliptic extension above the channel.

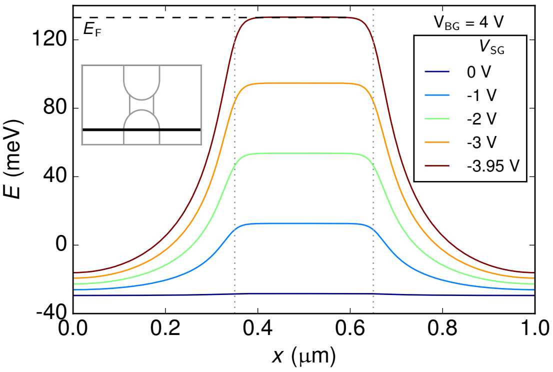

Figure F.2: Calculated electrostatic potential along a line cut (black line in inset) under the split gate for $V_{\mathrm{BG}} = 4$ V and various split gate voltages. The dotted lines indicate the extent of the split gates. At $V_{\mathrm{SG}} = 0$ V, the potential is constant throughout the structure. At $V_{\mathrm{SG}} = -3.95$ V, the region under the split gates is depleted.

value.

Depletion below split gates

Figure F.2 shows the calculated electrostatic potential along a line cut (black line in inset) under the split gate for $V_{\mathrm{BG}} = 4$ V and various split gate voltages. At $V_{\mathrm{SG}} = 0$ V, the potential is constant throughout the structure as expected. At $V_{\mathrm{SG}} = -3.95$ V, the region under the split gates is depleted. This voltage is in agreement with the experimentally determined depletion voltage.

Potential inside channel

In Fig. F.3a the potential inside the channel is shown, for the case in which transport under the split gates is suppressed ($V_{\mathrm{BG}} = 4$ V, $V_{\mathrm{SG}} = -3.95$ V). For $V_{\mathrm{CH}} = 0$ V, the potential can be approximated by a harmonic potential

$$V(y) = \frac{1}{2} m^* \omega_0^2 y^2$$

with an energy level separation of $\hbar\omega_0 = 8.4$ meV. For the gate voltage range of $V_{\mathrm{CH}} = -10$ V - 12 V the energy level separation changes according to

$$\hbar\omega_0(V_{\mathrm{CH}}) = 8.4 \text{ meV} + \alpha_{\mathrm{CH}} e V_{\mathrm{CH}}$$

with $\alpha_{\mathrm{CH}} = 0.33 \times 10^{-3}$. The increased mode spacing with higher channel gate voltage can also be observed in Fig. 7.3: the conductance rises less steeply for higher channel gate voltage.

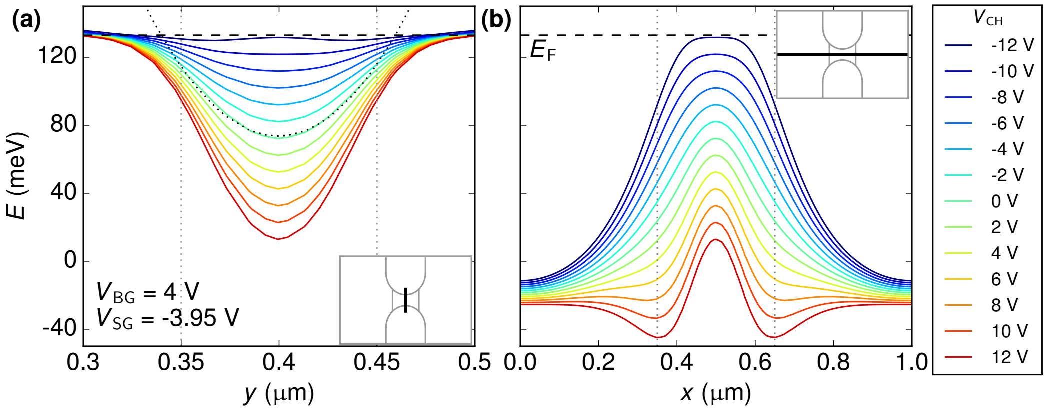

Figure F.3: Potential landscape for $V_{\text{BG}} = 4$ V, $V_{\text{SG}} = -3.95$ V and various channel gate voltages. (a) Electrostatic potential across the channel, which can be approximated by a harmonic potential (dotted black line). The channel gets depleted close to the experimental depletion voltage of $V_{\text{CH}} = -12$ V. (b) Electrostatic potential along the channel. For the range of $V_{\text{CH}} = -12$ V - 8 V a conventional saddle point potential is observed.

Figure F.3b shows the potential across the QPC. For the range of $V_{\text{CH}} = -12$ V - 8 V the positive curvature in y-direction and the negative curvature in x-direction lead to a conventional saddle point potential. Similar results were obtained for simulations of sample H.

G More QPC measurements

G.1 Role of the bulk in transport through QPC samples

The density in the bulk of the sample is higher than the density inside the constriction for the entire range of Fig. 7.4. Only the edge modes that exist in both the bulk and the channel contribute to transport and the conductance is given by $G = \nu_{\mathrm{CH}}\ e^2/h$. We can see a modest influence of the bulk of the device whenever the bulk is at a transition between integer filling factors. Figure G.1 shows the derivative of the conductance with respect to magnetic field as a function of V_{CH} and B for the same gate voltage settings as Fig. 7.4. The horizontal lines, which occur in a $1/B$ periodic fashion, correspond to Landau level transitions in the bulk of the sample. The filling factors of the bulk are indicated on the y-axis. Because of the high charge carrier density, no broken degeneracies are observed up to $B = 8$ T.

G.2 Disordered QPC

One of the 80 nm wide QPCs on sample I does not show any conductance quantization, see Fig. G.2. The rather irregular curve of conductance as a function of channel gate voltage points towards the presence of disorder inside the channel, leading to diffusive transport.

G.3 Transconductance on hole side

Figure G.3 shows the conductance as a function of channel gate voltage in QPC M for p-type charge carriers. Although the conductance at $B = 0$ T does not show any clear quantization (Fig. G.3a), the higher modes show a pattern of level crossings in presence of a magnetic field, similar to the pattern of level crossings discussed in Section 7.5.2.

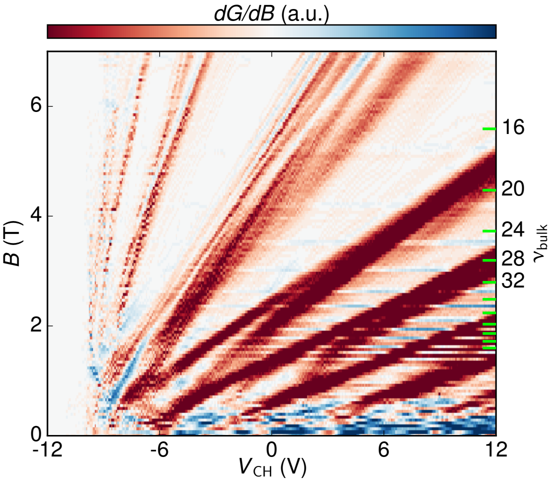

Figure G.1: Derivative of the conductance with respect to magnetic field for the same gate voltage settings as Fig. 4c. 1/B periodic horizontal lines are observed, which correspond to Landau level transitions in the bulk of the sample.

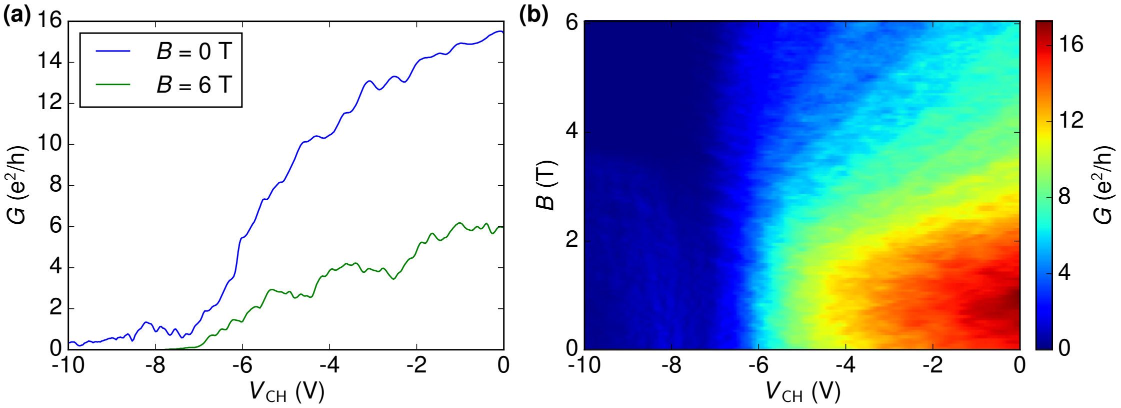

Figure G.2: (a) Conductance as a function of channel gate voltage for an 80 nm wide channel on sample I. No conductance quantization is observed. (b) Conductance as a function of channel gate voltage and magnetic field.

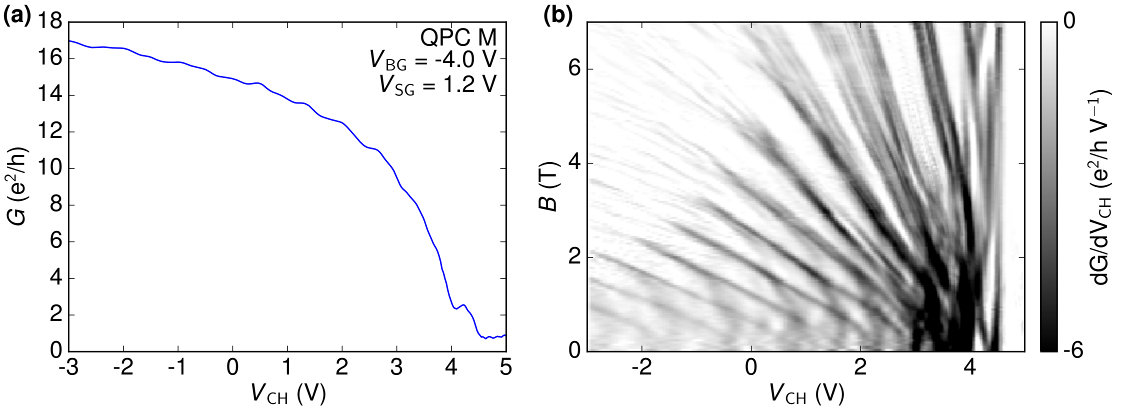

Figure G.3: (a) Conductance of QPC M as a function of channel gate voltage for *p*-type charge carriers (b) Transconductance as a function of channel gate voltage and magnetic field, showing a pattern of level crossings.

G.4 Finite bias diamonds of QPC M

Figure G.4 shows the finite bias diamonds of QPC M for various magnetic field strengths. The observed behavior is similar to that of QPC L1 (see Section 7.6).

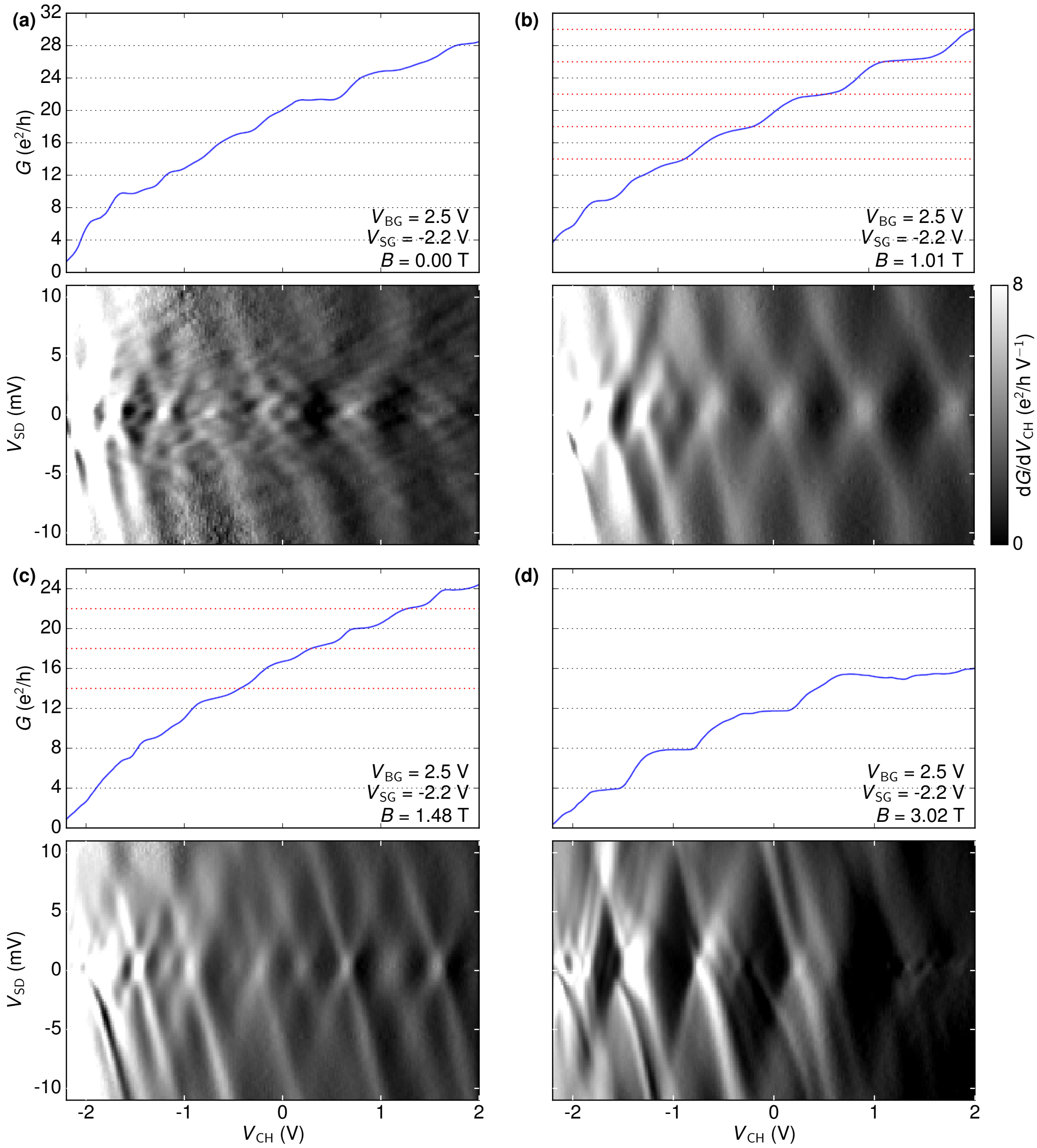

Figure G.4: (a) Top: Conductance as a function of V_{CH} for QPC M at $B = 0$ T. Bottom: Transconductance as a function of V_{CH} and V_{SD}. Finite bias diamonds coincide with conductance plateaus. (b),(c),(d) Same as (a) for various magnetic field strengths.

Bibliography

[1] K. S. Novoselov, A. K. Geim, S. V. Morozov, D. Jiang, Y. Zhang, S. V. Dubonos, I. V. Grigorieva, and A. A. Firsov, Science **306**, 666–669 (2004).

[2] B. Trauzettel, D. V. Bulaev, D. Loss, and G. Burkard, Nature Physics **3**, 192–196 (2007).

[3] D. P. DiVincenzo, Fortschr. Phys. **48**, 771–783 (2000).

[4] D. Bischoff, A. Varlet, P. Simonet, M. Eich, H. C. Overweg, T. Ihn, and K. Ensslin, Applied Physics Reviews **2**, 031301 (2015).

[5] E. McCann, Physical Review B **74**, 161403 (2006).

[6] A. Varlet, M.-H. Liu, V. Krueckl, D. Bischoff, P. Simonet, K. Watanabe, T. Taniguchi, K. Richter, K. Ensslin, and T. Ihn, Physical Review Letters **113**, 116601 (2014).

[7] A. Varlet, D. Bischoff, P. Simonet, K. Watanabe, T. Taniguchi, T. Ihn, K. Ensslin, M. Mucha-Kruczyński, and V. I. Fal'ko, Physical Review Letters **113**, 116602 (2014).

[8] H. Overweg, H. Eggimann, M. H. Liu, A. Varlet, M. Eich, P. Simonet, Y. Lee, K. Watanabe, T. Taniguchi, K. Richter, V. I. Fal'ko, K. Ensslin, and T. Ihn, Nano Letters **17**, 2852–2857 (2017).

[9] L. Kouwenhoven, C. Marcus, P. McEuen, S. Tarucha, R. Westervelt, and N. S. Wingreen, "Electron transport in quantum dots", in *Mesoscopic electron transport* (Kluwer, 1997), pp. 105–214.

[10] H. Overweg, H. Eggimann, X. Chen, S. Slizovskiy, M. Eich, P. Simonet, R. Pisoni, Y. Lee, K. Watanabe, T. Taniguchi, V. Fal'ko, K. Ensslin, and T. Ihn, Nano Letters **18**, 553–559 (2018).

[11] H. Overweg, P. Rickhaus, M. Eich, Y. Lee, R. Pisoni, K. Watanabe, T. Taniguchi, T. Ihn, and K. Ensslin, New Journal of Physics **20**, 013013 (2018).

[12] A. Varlet, M.-H. Liu, D. Bischoff, P. Simonet, T. Taniguchi, K. Watanabe, K. Richter, T. Ihn, and K. Ensslin, Physica Status Solidi - Rapid Research Letters **10**, 46–57 (2015).

[13] A. Varlet, *Tunable band structure in bilayer graphene: chirality and topology* (PhD Thesis, ETH Zürich, 2015).

[14]T. Ihn, *Semiconductor Nanostructures* (Oxford University Press, 2009).

[15]C. Luo, L. Zhou, K. Chiou, and J. Huang, Chem **4**, 784–794 (2018).

[16]P. Mesnier, *Graphene - an open source blockchain*, 2018.

[17]C. Lee, X. Wei, J. W. Kysar, and J. Hone, Science **321**, 385–388 (2008).

[18]A. K. Geim, Science **1530**, 1530–1535 (2014).

[19]A. A. Balandin, S. Ghosh, W. Bao, I. Calizo, D. Teweldebrhan, F. Miao, and C. N. Lau, Nano Letters **8**, 902–907 (2008).

[20]M. I. Katsnelson, K. S. Novoselov, and A. K. Geim, Nature Physics **2**, 620–625 (2006).

[21]V. P. Gusynin and S. G. Sharapov, Physical Review Letters **95**, 146801 (2005).

[22]Y. Cao, V. Fatemi, A. Demir, S. Fang, S. L. Tomarken, J. Y. Luo, J. D. Sanchez-Yamagishi, K. Watanabe, T. Taniguchi, E. Kaxiras, R. C. Ashoori, and P. Jarillo-Herrero, Nature **556**, 80–84 (2018).

[23]B. Padhi, C. Setty, and P. W. Phillips, Arxiv Preprint, 1804.01101 (2018).

[24]S. Huang, K. Kim, D. K. Efimkin, T. Lovorn, T. Taniguchi, K. Watanabe, A. H. MacDonald, E. Tutuc, and B. J. LeRoy, Phyisical Review Letters **121**, 037702 (2018).

[25]P. Rickhaus, J. Wallbank, S. Slizovskiy, M.-h. Liu, R. Pisoni, H. Overweg, Y. Lee, M. Eich, K. Watanabe, T. Taniguchi, V. Fal, T. Ihn, and K. Ensslin, Arxiv preprint, 1802.07317 (2018).

[26]C. R. Dean, A. F. Young, I. Meric, C. Lee, L. Wang, S. Sorgenfrei, K. Watanabe, T. Taniguchi, P. Kim, K. L. Shepard, and J. Hone, Nature Nanotechnology **5**, 722–726 (2010).

[27]L. Wang, I. Meric, P. Y. Huang, Q. Gao, Y. Gao, H. Tran, T. Taniguchi, K. Watanabe, L. M. Campos, D. a. Muller, J. Guo, P. Kim, J. Hone, K. L. Shepard, and C. R. Dean, Science **342**, 614–7 (2013).

[28]L. Grover, STOC '96 Proceedings of the twenty-eighth annual ACM symposium on Theory of computing, 212–219 (1996).

[29]P. Shor, SIAM J. Comput. **26**, 1484–1509 (1997).

[30]F. H. L. Koppens, C. Buizert, K. J. Tielrooij, I. T. Vink, K. C. Nowack, T. Meunier, L. P. Kouwenhoven, and L. M. K. Vandersypen, Nature **442**, 766–771 (2006).

[31]K. Nowack, F. Koppens, Y. Nazarov, and L. Vandersypen, Science **318**, 1430–1433 (2007).

[32]A. H. Castro Neto, N. M. R. Peres, K. S. Novoselov, and A. K. Geim, Reviews of Modern Physics **81**, 109–162 (2009).

[33] E. McCann, “Electronic Properties of Monolayer and Bilayer Graphene”, in *Graphene nanoelectronics: metrology, synthesis, properties and applications* (Springer, 2014), pp. 237–275.

[34] J. W. McClure, Physical Review **108**, 612–618 (1957).

[35] J. C. Slonczewski and P. R. Weiss, Physical Review **109**, 272–279 (1958).

[36] A. B. Kuzmenko, I. Crassee, D. Van Der Marel, P. Blake, and K. S. Novoselov, Physical Review B **80**, 165406 (2009).

[37] A. Varlet, M. Mucha-Kruczyński, D. Bischoff, P. Simonet, T. Taniguchi, K. Watanabe, V. Fal’Ko, T. Ihn, and K. Ensslin, Synthetic Metals **210**, 19–31 (2015).

[38] E. McCann and V. I. Fal’ko, Physical Review Letters **96**, 086805 (2006).

[39] E. McCann, D. S. L. Abergel, and V. I. Fal’ko, Solid State Communications **143**, 110–115 (2007).

[40] T. Ohta, A. Bostwick, T. Seyller, K. Horn, and E. Rotenberg, Science **313**, 951–954 (2006).

[41] Y. Zhang, T. T. Tang, C. Girit, Z. Hao, M. C. Martin, A. Zettl, M. F. Crommie, Y. R. Shen, and F. Wang, Nature **459**, 820–823 (2009).

[42] L. M. Zhang, Z. Q. Li, D. N. Basov, M. M. Fogler, Z. Hao, and M. C. Martin, Physical Review B **78**, 235408 (2008).

[43] J. B. Oostinga, H. B. Heersche, X. Liu, A. F. Morpurgo, and L. M. K. Vandersypen, Nature Materials **7**, 151–157 (2008).

[44] K. Zou and J. Zhu, Physical Review B **82**, 081407 (2010).

[45] T. Taychatanapat and P. Jarillo-Herrero, Physical Review Letters **105**, 166601 (2010).

[46] R. T. Weitz, M. T. Allen, B. E. Feldman, J. Martin, and A. Yacoby, Science **330**, 812–816 (2010).

[47] S. Dröscher, *Electronic properties of confined systems in single and bilayer graphene* (PhD Thesis, ETH Zürich, 2012).

[48] M. Sui, G. Chen, L. Ma, W. Y. Shan, D. Tian, K. Watanabe, T. Taniguchi, X. Jin, W. Yao, D. Xiao, and Y. Zhang, Nature Physics **11**, 1027–1031 (2015).

[49] Y. Shimazaki, M. Yamamoto, I. V. Borzenets, K. Watanabe, T. Taniguchi, and S. Tarucha, Nature Physics **11**, 1032–1036 (2015).

[50] J. Li, K. Wang, K. J. McFaul, Z. Zern, Y. Ren, K. Watanabe, T. Taniguchi, Z. Qiao, and J. Zhu, Nature Nanotechnology **11**, 1060–1065 (2016).

[51] M. J. Zhu, A. V. Kretinin, M. D. Thompson, D. A. Bandurin, S. Hu, G. L. Yu, J. Birkbeck, A. Mishchenko, I. J. Vera-Marun, K. Watanabe, T. Taniguchi, M. Polini, J. R. Prance, K. S. Novoselov, A. K. Geim, and M. Ben Shalom, Nature Communications **8**, 14552 (2017).

[52]E. V. Castro, N. M. R. Peres, and J. M. B. Lopes Dos Santos, Journal of Optoelectronics and Advanced Materials **10**, 1716–1721 (2008).

[53]J. Li, I. Martin, M. Buttiker, A. F. Morpurgo, M. Büttiker, and A. F. Morpurgo, Nature Physics **7**, 38–42 (2011).

[54]M. T. Allen, O. Shtanko, I. C. Fulga, A. R. Akhmerov, K. Watanabe, T. Taniguchi, P. Jarillo-Herrero, L. S. Levitov, and A. Yacoby, Nature Physics **12**, 128–133 (2016).

[55]B. Hunt, T. Taniguchi, P. Moon, M. Koshino, and R. C. Ashoori, Science **340**, 1427–1431 (2013).

[56]Z. Dou, S. Morikawa, A. Cresti, S.-W. Wang, C. G. Smith, C. Melios, O. Kazakova, K. Watanabe, T. Taniguchi, S. Masubuchi, T. Machida, and M. R. Connolly, Nano Letters **18**, 2530–2537 (2018).

[57]I. Martin, Y. M. Blanter, and a. F. Morpurgo, Physical Review Letters **100**, 036804 (2008).

[58]F. Zhang, A. H. MacDonald, and E. J. Mele, Proceedings of the National Academy of Sciences **110**, 10546–10551 (2013).

[59]A. Vaezi, Y. Liang, D. H. Ngai, L. Yang, and E. A. Kim, Physical Review X **3**, 021018 (2013).

[60]L. Ju, Z. Shi, N. Nair, Y. Lv, C. Jin, J. Velasco, C. Ojeda-Aristizabal, H. a. Bechtel, M. C. Martin, A. Zettl, J. Analytis, and F. Wang, Nature **520**, 650–655 (2015).

[61]L. J. Yin, H. Jiang, J. B. Qiao, and L. He, Nature Communications **7**, 11760 (2016).

[62]X. Du, I. Skachko, A. Barker, and E. Y. Andrei, Nature Nanotechnology **3**, 491–495 (2008).

[63]D. Bischoff, *Localized electrons in graphene nanostructures* (PhD Thesis, ETH Zürich, 2014).

[64]A. C. Ferrari, J. C. Meyer, V. Scardaci, C. Casiraghi, M. Lazzeri, F. Mauri, S. Piscanec, D. Jiang, K. S. Novoselov, S. Roth, and a. K. Geim, Physical Review Letters **97**, 187401 (2006).

[65]A. Castellanos-Gomez, M. Buscema, R. Molenaar, V. Singh, L. Janssen, H. S. J. van der Zant, and G. A. Steele, 2D Materials, 011002 (2014).

[66]P. J. Zomer, M. H. D. Guimarães, J. C. Brant, N. Tombros, B. J. V. Wees, J. C. Brant, N. Tombros, and B. J. V. Wees, Applied Physics Letters **105**, 013101 (2014).

[67]R. Frisenda, E. Navarro-Moratalla, P. Gant, D. Pérez De Lara, P. Jarillo-Herrero, R. V. Gorbachev, and A. Castellanos-Gomez, Chemical Society Reviews **47**, 53–68 (2018).

[68] M. A. Mohammad, M. Muhammad, S. K. Dew, and M. Stepanova, "Fundamentals of Electron Beam Exposure and Development", in *Nanofabrication* (Springer, 2012).

[69] L. Banszerus, M. Schmitz, S. Engels, J. Dauber, M. Oellers, F. Haupt, K. Watanabe, T. Taniguchi, B. Beschoten, and C. Stampfer, Science Advances **1**, e1500222 (2015).

[70] T. Kobayashi, M. Bando, N. Kimura, K. Shimizu, K. Kadono, and N. Umezu, Applied Physics Letters **102**, 023112 (2013).

[71] V. E. Calado, S.-E. Zhu, S. Goswami, Q. Xu, K. Watanabe, T. Taniguchi, G. C. A. M. Janssen, and L. M. K. Vandersypen, Applied Physics Letters **104**, 023103 (2014).

[72] L. Banszerus, M. Schmitz, S. Engels, M. Goldsche, K. Watanabe, T. Taniguchi, B. Beschoten, and C. Stampfer, Nano Letters **16**, 1387–1391 (2016).

[73] G. Giovannetti, P. A. Khomyakov, G. Brocks, V. M. Karpan, J. Van Den Brink, and P. J. Kelly, Physical Review Letters **101**, 026803 (2008).

[74] J. Martin, N. Akerman, G. Ulbricht, T. Lohmann, J. H. Smet, K. von Klitzing, and A. Yacoby, Nature Physics **4**, 144–148 (2007).

[75] A. L. Grushina, D.-K. Ki, and A. F. Morpurgo, Applied Physics Letters **102**, 223102 (2013).

[76] P. Rickhaus, R. Maurand, M.-H. Liu, M. Weiss, K. Richter, and C. Schönenberger, Nature Communications **4**, 2342 (2013).

[77] E. McCann and M. Koshino, Reports on Progress in Physics **76**, 056503 (2013).

[78] E. McCann, K. Kechedzhi, V. I. Fal'ko, H. Suzuura, T. Ando, and B. L. Altshuler, Physical Review Letters **97**, 146805 (2006).

[79] K. Nomura and A. H. MacDonald, Physical Review Letters **96**, 256602 (2006).

[80] D. A. Abanin and L. S. Levitov, Physical Review B **78**, 035416 (2008).

[81] A. K. Geim and K. S. Novoselov, Nature Materials **6**, 183–191 (2007).

[82] L. M. Zhang, M. M. Fogler, and D. P. Arovas, Physical Review B **84**, 075451 (2011).

[83] B. E. Feldman, J. Martin, and A. Yacoby, Nature Physics **5**, 889–893 (2009).

[84] J. V. s. J. Suff, L. Jing, W. Bao, Y. Lee, P. Kratz, V. Aji, M. Bockrath, C. N. Lau, C. Varma, R. Stillwell, D. Smirnov, F. Zhang, J. Jung, and A. H. MacDonald, Nature Nanotechnology **7**, 156–160 (2012).

[85] K. Lee, B. Fallahazad, J. Xue, D. C. Dillen, K. Kim, T. Taniguchi, K. Watanabe, and E. Tutuc, Science **345**, 58–61 (2014).

[86] M. Schmitz, S. Engels, L. Banszerus, K. Watanabe, T. Taniguchi, C. Stampfer, and B. Beschoten, Applied Physics Letters **110**, 263110 (2017).

[87] T. Taychatanapat, J. Y. Tan, Y. Yeo, K. Watanabe, T. Taniguchi, and B. Özyilmaz, Nature Communications **6**, 6093 (2015).

[88] P. Rickhaus, P. Makk, M.-h. Liu, E. Tóvári, M. Weiss, R. Maurand, K. Richter, and C. Schönenberger, Nature Communications **6**, 6470 (2015).

[89] F. Amet, J. R. Williams, K. Watanabe, T. Taniguchi, and D. Goldhaber-Gordon, Physical Review Letters **112**, 196601 (2014).

[90] J. R. Williams, L. DiCarlo, and C. M. Marcus, Science **317**, 638–641 (2007).

[91] B. Özyilmaz, P. Jarillo-Herrero, D. Efetov, D. a. Abanin, L. S. Levitov, and P. Kim, Physical Review Letters **99**, 166804 (2007).

[92] D. K. Ki, S. G. Nam, H. J. Lee, and B. Özyilmaz, Physical Review B **81**, 033301 (2010).

[93] S. Morikawa, S. Masubuchi, R. Moriya, K. Watanabe, T. Taniguchi, and T. Machida, Applied Physics Letters **106**, 183101 (2015).

[94] E. Tóvári, P. Makk, P. Rickhaus, C. Schönenberger, and S. Csonka, Nanoscale **8**, 11480–11486 (2016).

[95] N. Kumada, F. D. Parmentier, H. Hibino, D. C. Glattli, and P. Roulleau, Nature Communications **6**, 8068 (2015).

[96] S. Matsuo, S. Takeshita, T. Tanaka, S. Nakaharai, K. Tsukagoshi, T. Moriyama, T. Ono, and K. Kobayashi, Nature Communications **6**, 8066 (2015).

[97] S. Engels, B. Terrés, A. Epping, T. Khodkov, K. Watanabe, T. Taniguchi, B. Beschoten, and C. Stampfer, Physical Review Letters **113**, 126801 (2014).

[98] M. H. Liu, P. Rickhaus, P. Makk, E. Tóvári, R. Maurand, F. Tkatschenko, M. Weiss, C. Schönenberger, and K. Richter, Physical Review Letters **114**, 036601 (2015).

[99] A. A. Patel, N. Davies, V. Cheianov, and V. I. Fal'Ko, Physical Review B **86**, 081413 (2012).

[100] M. Raikh and T. Shahbazyan, Physical Review B **49**, 5531–5540 (1994).

[101] I. A. Dmitriev, A. D. Mirlin, D. G. Polyakov, and M. A. Zudov, Reviews of Modern Physics **84**, 1709–1763 (2012).

[102] P. Rickhaus, M.-H. Liu, P. Makk, R. Maurand, S. Hess, S. Zihlmann, M. Weiss, K. Richter, and C. Schönenberger, Nano Letters **15**, 5819–5825 (2015).

[103] S. Chen, Z. Han, M. M. Elahi, K. M. M. Habib, L. Wang, B. Wen, Y. Gao, T. Taniguchi, K. Watanabe, J. Hone, A. W. Ghosh, and C. R. Dean, Science **353**, 1522–1525 (2016).

[104] M. Eich, F. Herman, R. Pisoni, H. Overweg, Y. Lee, P. Rickhaus, K. Watanabe, T. Taniguchi, M. Sigrist, T. Ihn, and K. Ensslin, Physical Review X **8**, 031023 (2018).

[105] M. T. Allen, J. Martin, and A. Yacoby, Nature Communications **3**, 934 (2012).

[106] A. S. M. Goossens, S. C. M. Driessen, T. A. Baart, K. Watanabe, T. Taniguchi, and L. M. K. Vandersypen, Nano Letters **12**, 4656–4660 (2012).

[107] S. Dröscher, C. Barraud, K. Watanabe, T. Taniguchi, T. Ihn, and K. Ensslin, New Journal of Physics **14**, 103007 (2012).

[108] Y. J. Um, Y. H. Oh, M. Seo, S. Lee, Y. Chung, N. Kim, V. Umansky, and D. Mahalu, Applied Physics Letters **100**, 183502 (2012).

[109] N. Tombros, A. Veligura, J. Junesch, M. H. D. Guimarães, I. J. V. Marun, H. T. Jonkman, and B. J. van Wees, Nature Physics **7**, 697–700 (2011).

[110] S. Somanchi, B. Terrés, J. Peiro, M. Staggenborg, K. Watanabe, T. Taniguchi, B. Beschoten, and C. Stampfer, Annalen der Physik, 1700082 (2017).

[111] B. Terrés, L. A. Chizhova, F. Libisch, J. Peiro, D. Jörger, S. Engels, A. Girschik, K. Watanabe, T. Taniguchi, S. V. Rotkin, J. Burgdörfer, and C. Stampfer, Nature Communications **7**, 11528 (2016).

[112] M. Kim, J.-H. Choi, S.-H. Lee, K. Watanabe, T. Taniguchi, S.-H. Jhi, and H.-J. Lee, Nature Physics **12**, 1022–1026 (2016).

[113] K. Zimmermann, A. Jordan, F. Gay, K. Watanabe, T. Taniguchi, Z. Han, V. Bouchiat, H. Sellier, and B. Sacépé, Nature Communications **8**, 14983 (2017).

[114] P. D. Ye, D. Weiss, R. R. Gerhardts, K. von Klitzing, K. Eberl, H. Nickel, and C. T. Foxon, Semiconductor Science and Technology **10**, 715–719 (1995).

[115] E. V. Castro, N. M. R. Peres, T. Stauber, and N. A. P. Silva, Physical Review Letters **100**, 186803 (2008).

[116] C. Beenakker and H. V. Houten, Solid State Physics **44**, 1–228 (1991).

[117] M. Büttiker, Physical Review B **41**, 7906–7909 (1990).

[118] B. M. Hunt, J. I. A. Li, A. A. Zibrov, L. Wang, T. Taniguchi, K. Watanabe, J. Hone, C. R. Dean, M. Zaletel, R. C. Ashoori, and A. F. Young, Nature Communications **8**, 1–7 (2017).

[119] D. Xiao, W. Yao, and Q. Niu, Physical Review Letters **99**, 1–4 (2007).

[120] D. S. Wei, T. van der Sar, J. D. Sanchez-Yamagishi, K. Watanabe, T. Taniguchi, P. Jarillo-Herrero, B. I. Halperin, and A. Yacoby, Science Advances **3**, e1700600 (2017).

[121] C. Handschin, *Quantum Transport in Encapsulated Graphene P-N junctions* (PhD Thesis, Universität Basel, 2017).

[122] B. J. van Wees, L. P. Kouwenhoven, C. J. P. M. Harmans, J. G. Williamson, C. E. Timmering, M. E. I. Broekaart, C. T. Foxon, and J. J. Harris, Physical Review Letters **62**, 2523–2526 (1989).

[123] R. P. Taylor, A. S. Sachrajda, P. Zawadzki, P. T. Coleridge, and J. A. Adams, Physical Review Letters **69**, 1989–1992 (1992).

[124] A. A. M. Staring, B. W. Alphenaar, H. van Houten, L. W. Molenkamp, O. J. A. Buyk, M. A. A. Mabesoone, and C. T. Foxon, Physical Review B **46**, 12869–12872 (1992).

[125] T. Heinzel, D. A. Wharam, J. P. Kotthaus, G. Böhm, W. Klein, G. Tränkle, and G. Weimann, Physical Review B **50**, 15113–15119 (1994).

[126] N. C. van der Vaart, L. P. Kouwenhoven, M. P. de Ruyter van Steveninck, Y. V. Nazarov, C. J. P. M. Harmans, and C. T. Foxon, Physical Review B **55**, 9746–9756 (1997).

[127] Y. Zhang, D. T. McClure, E. M. Levenson-Falk, C. M. Marcus, L. N. Pfeiffer, and K. W. West, Physical Review B **79**, 241304 (2009).

[128] S. Baer, C. Rössler, T. Ihn, K. Ensslin, C. Reichl, and W. Wegscheider, New Journal of Physics **15**, 023035 (2013).

[129] S. Ilani, J. Martin, E. Teitelbaum, J. H. Smet, D. Mahalu, V. Umansky, and A. Yacoby, Nature **427**, 328–332 (2004).

[130] B. Rosenow and B. I. Halperin, Physical Review Letters **98**, 106801 (2007).

[131] A. A. Zibrov, C. Kometter, H. Zhou, E. M. Spanton, T. Taniguchi, K. Watanabe, M. P. Zaletel, and A. F. Young, Nature **549**, 360–364 (2017).

[132] J. I. A. Li, C. Tan, S. Chen, Y. Zeng, T. Taniguchi, K. Watanabe, J. Hone, and C. R. Dean, Science **358**, 1–9 (2017).

[133] A. Stern and B. Halperin, Physical Review Letters **96**, 016802 (2006).

[134] Z. Wang, D. K. Ki, H. Chen, H. Berger, A. H. MacDonald, and A. F. Morpurgo, Nature Communications **6**, 8339 (2015).

[135] M. A. Topinka, B. J. LeRoy, R. M. Westervelt, S. E. Shaw, R. Fleischmann, E. J. Heller, K. D. Maranowski, and a. C. Gossard, Nature **410**, 183–6 (2001).

[136] R. Steinacher, A. A. Kozikov, C. Rössler, C. Reichl, W. Wegscheider, K. Ensslin, and T. Ihn, Physical Review B **93**, 085303 (2016).

[137] D. A. Bandurin, I. Torre, R. Krishna Kumar, M. Ben Shalom, A. Tomadin, A. Principi, G. H. Auton, E. Khestanova, K. S. Novoselov, I. V. Grigorieva, L. A. Ponomarenko, A. K. Geim, and M. Polini, Science **351**, 1055–1058 (2016).

[138] P. Maletinsky, S. Hong, M. S. Grinolds, B. Hausmann, M. D. Lukin, R. L. Walsworth, M. Loncar, and A. Yacoby, Nature Nanotechnology **7**, 320–324 (2012).

[139] R. Krishna Kumar, D. A. Bandurin, F. M. Pellegrino, Y. Cao, A. Principi, H. Guo, G. H. Auton, M. Ben Shalom, L. A. Ponomarenko, G. Falkovich, K. Watanabe, T. Taniguchi, I. V. Grigorieva, L. S. Levitov, M. Polini, and A. K. Geim, Nature Physics **13**, 1182–1185 (2017).

[140] Y. T. Cui, B. Wen, E. Y. Ma, G. Diankov, Z. Han, F. Amet, T. Taniguchi, K. Watanabe, D. Goldhaber-Gordon, C. R. Dean, and Z. X. Shen, Physical Review Letters **117**, 186601 (2016).

[141] D. Bischoff, M. Eich, O. Zilberberg, C. Rössler, T. Ihn, and K. Ensslin, Nano Letters **15**, 6003–6008 (2015).

[142] R. Schleser, E. Ruh, T. Ihn, K. Ensslin, D. C. Driscoll, and A. C. Gossard, Applied Physics Letters **85**, 2005–2007 (2004).

[143] A. Hofmann, V. F. Maisi, C. Gold, T. Krähenmann, C. Rössler, J. Basset, P. Märki, C. Reichl, W. Wegscheider, K. Ensslin, and T. Ihn, Physical Review Letters **117**, 206803 (2016).

[144] B. Küng, C. Rössler, M. Beck, M. Marthaler, D. Golubev, Y. Utsumi, T. Ihn, and K. Ensslin, Physical Review X **2**, 011001 (2012).

[145] A. Hofmann, V. F. Maisi, J. Basset, C. Reichl, W. Wegscheider, T. Ihn, K. Ensslin, and C. Jarzynski, Physica Status Solidi (B) **254**, 1600546 (2017).

[146] J. Elzerman, R. Hanson, L. Willems van Beveren, B. Witkamp, L. Vandersypen, and L. Kouwenhoven, Nature **430**, 431–435 (2004).

[147] N. Samkharadze, G. Zheng, N. Kalhor, D. Brousse, A. Sammak, U. C. Mendes, A. Blais, G. Scappucci, and L. M. K. Vandersypen, Science **359**, 1123–1127 (2018).

[148] X. Mi, M. Benito, S. Putz, D. M. Zajac, J. M. Taylor, G. Burkard, and J. R. Petta, Nature **555**, 599–603 (2018).

[149] A. J. Landig, J. V. Koski, P. Scarlino, U. C. Mendes, A. Blais, C. Reichl, W. Wegscheider, A. Wallraff, K. Ensslin, and T. Ihn, Arxiv Preprint, 1711.01932 (2017).

[150] K. Wang, A. Harzheim, J. U. Lee, T. Taniguchi, K. Watanabe, and P. Kim, Arxiv Preprint, 1711.03184 (2018).

[151] A. K. Geim and I. V. Grigorieva, Nature **499**, 419–425 (2013).

[152] D. R. Klein, D. MacNeill, J. L. Lado, D. Soriano, E. Navarro-Moratalla, K. Watanabe, T. Taniguchi, S. Manni, P. Canfield, J. Fernández-Rossier, and P. Jarillo-Herrero, Science **360**, 1218–1222 (2018).

[153] S. De Franceschi, L. Kouwenhoven, C. Schönenberger, and W. Wernsdorfer, Nature Nanotechnology **5**, 703–711 (2010).

[154] Y. Cao, A. Mishchenko, G. L. Yu, E. Khestanova, A. P. Rooney, E. Prestat, A. V. Kretinin, P. Blake, M. B. Shalom, C. Woods, J. Chapman, G. Balakrishnan, I. V. Grigorieva, K. S. Novoselov, B. A. Piot, M. Potemski, K. Watanabe, T. Taniguchi, S. J. Haigh, A. K. Geim, and R. V. Gorbachev, Nano Letters **15**, 4914–4921 (2015).

[155] M. H. Liu and K. Richter, Physical Review B **86**, 115455 (2012).

[156] M. H. Liu, J. Bundesmann, and K. Richter, Physical Review B **85**, 085406 (2012).

[157] V. V. Cheianov and V. I. Fal'ko, Physical Review B **74**, 041403 (2006).

Acknowledgements

It is in fact quite misleading that my name is the only one featuring on the cover of this thesis. This work has been a team effort, and I would like to thank the following people:

Klaus, the past four years have been a great experience in many respects. Thank you for providing this fantastic opportunity to explore exciting physics, to learn plenty of new skills and to get to know so many wonderful people. Your engagement as a supervisor is as large as any PhD student could wish for.
Thomas, thank you for the in-depth physics discussions. Your eye for detail is what got us there in the end. And thank you for the music of course. It has been great fun to play together.
Srijit and Christian, thank you for co-examining my thesis. I am looking forward to seeing your future results on graphene!
Thanks to Peter, Erwin, Cecil and the FIRST operational team for their invaluable technical support.
Thank you Claudia, for making our group run so smoothly!
Anastasia, Dominik and Pauline, thank you for introducing me to the field of graphene. Your protocols and recipes have been of great help. Et merci pour toutes nos conversations en Français. Anastasia, thank you for staying involved throughout my PhD. It was always a pleasure to discuss new results with you.
Marius, it was great to have you as a colleague on this project. We have had a lot of fun while playing the clarinet, running, cycling home and defeating aliens in outer space. You are an awesome hypernavigator! Thank you for all your enthusiasm.
Yongjin and Aroosa, thank you for all the open minded conversations we had while running or strolling through the forest.
Riccardo, the fabrication knowledge you brought to the 2D team has been of significant impact on the results of everyone in our office. And now for the last time: doei doei!
Peter, I am amazed by the countless exciting projects you came up with during our brainstorm sessions. And thank you for all the quick feedback for my thesis and our papers.
Annika, thank you for the feedback on my thesis and thank you for continuing the work on bilayer graphene nanostructures. It is a good feeling to leave the project in your competent hands!

Carolin, thank you for temporarily sharing the frustrations of a complicated diet. A shared problem is a problem halved, right? Thank you for the yummy cakes and thank you for the music as well.

I would like to thank all other Ensslin group members for their advise, feedback and participation in running sessions, pub quizzes, board game evenings and the balloon blowing ensemble. Thanks to you it was always a delight to go to work, even at times where the project seemed to be at a dead end.

During my PhD I have had the pleasure to supervise Pol, Aideen, Hannah, Thomas and Lucien. You were absolutely great students, and I learned a lot by teaching you!

I would like to thank Ming-Hao Liu, Klaus Richter, Xi Chen, Sergey Slizovskiy and Vladimir Fal'ko for fruitful discussion and the theoretical insights they provided for this thesis.

I higly appreciated the scientific discussions with Péter Makk, Mansour Shayegan and David Sanchez as well.

Thanks to all my friends for providing just the right amount of distraction from work. Taking a break at the right moment is the best way to keep going, I believe.

Jasper, thank you for your optimism, which has helped me get unstuck on numerous occasions. It has been great to share all the fun and frustrations of my PhD studies with you. Thank you for being there for me.

Papa, mama and Sietske, thank you for all the support you provided no matter what path I took. Studying music at the conservatory, combining it with physics, moving to France, moving to Switzerland, moving back to the Netherlands, moving back to Switzerland, nothing was too crazy for you! Perhaps I should consider moving to Jupiter in the future. Will you come and pay me a visit? ;)